



저작자표시-비영리-변경금지 2.0 대한민국

이용자는 아래의 조건을 따르는 경우에 한하여 자유롭게

- 이 저작물을 복제, 배포, 전송, 전시, 공연 및 방송할 수 있습니다.

다음과 같은 조건을 따라야 합니다:



저작자표시. 귀하는 원저작자를 표시하여야 합니다.



비영리. 귀하는 이 저작물을 영리 목적으로 이용할 수 없습니다.



변경금지. 귀하는 이 저작물을 개작, 변형 또는 가공할 수 없습니다.

- 귀하는, 이 저작물의 재이용이나 배포의 경우, 이 저작물에 적용된 이용허락조건을 명확하게 나타내어야 합니다.
- 저작권자로부터 별도의 허가를 받으면 이러한 조건들은 적용되지 않습니다.

저작권법에 따른 이용자의 권리는 위의 내용에 의하여 영향을 받지 않습니다.

이것은 [이용허락규약\(Legal Code\)](#)을 이해하기 쉽게 요약한 것입니다.

[Disclaimer](#)

공학박사학위논문

**질량-강성 분절설계 탄성 메타물질을
활용한 완벽투과율 초음파 제어**

**Mass-Stiffness Substructured Elastic Metamaterials
for Total Transmission Ultrasonic Wave Engineering**

2018년 8월

서울대학교 대학원
기계항공공학부
이 혁

ABSTRACT

Mass-Stiffness Substructured Elastic Metamaterials for Total Transmission Ultrasonic Wave Engineering

Hyuk Lee

School of Mechanical and Aerospace Engineering

The Graduate School

Seoul National University

This dissertation aims to investigate and provide a new design methodology for fully transmissive mass-stiffness substructured elastic metamaterials for various extraordinary wave phenomena. Recently, there have been numerous developments of engineered elastic metamaterials to innovatively control ultrasonic waves for broad range of applications including non-destructive evaluation and biomedical screening. However, conventional devices still suffer from low transmission that stems from the intrinsic impedance mismatch between the artificially fabricated (perforated or composite) metamaterials and the background medium, which in result severely disturbs the quality of inspection.

To resolve such chronic dilemma, we propose an explicit way to independently

facilitate mass and stiffness properties of an elastic metamaterial unit cell so that its own impedance can be conveniently tuned with respect to the outer elastic medium. Specifically, we first design the basic substructures containing properly designed local resonators so that each of them can exclusively tune either mass or stiffness only. By combining the substructures in proper manners, impedance matching condition (for total transmission) together with anomalous effective parameters (not only negative mass/stiffness values but also their extreme positive values) can be available for extraordinary wave phenomena.

By utilizing the developed substructuring method, two major novel elastic metamaterial structures are proposed and researched. To design an elastic metasurface for anomalous beam steering within subwavelength scale, we utilize amplified mass and lowered stiffness to achieve both the impedance matching condition and low phase velocity for wide range of phase gradients. On the other hand, for super-resolution diffraction limit breaking lens, we adopt both extreme stiffness and negative effective mass simultaneously for hyperbolic dispersion and impedance matching condition. Such exceptional substructuring mechanism and its applications are expected to significantly enhance the design flexibility of elastic metamaterials for fine quality fully transmissive ultrasonic wave inspection.

Keywords: Elastic metamaterial, Lumped elements, Ultrasonic wave, Periodic system, Effective properties.

Student Number: 2012-22564

TABLE OF CONTENTS

ABSTRACT	i
TABLE OF CONTENTS	iii
LIST OF TABLES	vii
LIST OF FIGURES.....	viii
<CHAPTER 1> INTRODUCTION.....	1
1.1 Research Motivation	1
1.2 Research Objectives	3
1.3 Outline of Thesis	6
<CHAPTER 2> WAVE PROPAGATION IN PERIODIC LUMPED ELEMENT STRUCTURES.....	9
2.1 Chapter Overview	9
2.2 1-D Lumped-Element Lattice.....	10
2.2.1 Dispersion relation analysis	11
2.2.2 2-Dimensional dispersion relation: Equi-frequency contour (EFC)	13
2.3 1-D Lumped-Element Lattice with Local Resonators: Metamaterials.....	15
2.3.1 Effective mass tuning by dipolar resonance.....	16
2.3.2 Effective stiffness tuning by monopolar resonance.....	17

2.4 Wave Propagation Analysis for Metamaterials	19
---	----

**<CHAPTER 3> PROPOSITION OF TRANSFER MATRIX METHOD FOR
SUBSTRUCTURE DESIGN AND ANALYSIS.....33**

3.1 Chapter Overview	33
3.2 Transfer Matrix Method	35
3.2.1 Spring-Mass-Spring model (M_{eff} -substructure)	38
3.2.2 Mass-Spring-Mass model (K_{eff} -substructure)	40
3.3 Transfer Matrix Method Employed in Theoretical Domain.....	42
3.3.1 Dispersion curve evaluation	42
3.3.2 Characteristic impedance evaluation.....	44
3.3.3 Transmission spectra of multiple lumped-element structures embedded within continuum media	47
3.4 Transfer Matrix Method Employed in Numerical Simulation Domain with Actual Continuum Structures	52
3.4.1 Dispersion curve, characteristic impedance, and transmission coefficient retrieval	56
3.4.2 Effective parameter retrieval	59
3.5 Summary	64

**<CHAPTER 4> ELASTIC METASURFACE FOR HIGH TRANSMISSION
ANOMALOUS BEAM REFRACTION78**

4.1 Chapter Overview	78
4.2 Generalized Snell's Law.....	81
4.3 Mechanics of Substructured Unit Cell	82
4.3.1 Analysis on each substructure	85
4.3.2 Analysis on the geometry of slits to control stiffness	87
4.3.3 Dispersion relation	90
4.4 Transmission and Phase Spectra for Multiple Unit Cells.....	90
4.4.1 Full transmission condition due to impedance matching and tunneling.....	93
4.4.2 Unit cell geometry variation for both full transmission and 2π phase coverage	95
4.5 Numerical Simulation of the Refracted Beam Pattern Manipulation.....	99
4.6 Experimental Validation.....	102
4.7 Summary	106

<CHAPTER 5> HYPERBOLIC ELASTIC METAMATERIAL LENS FOR

TOTAL TRANSMISSION SUPER-RESOLUTION IMAGING131

5.1 Chapter Overview	131
5.2 Mechanics of Highly Anisotropic Unit Cell.....	134
5.2.1 2-D mass-spring model	135
5.2.2 Basic equation for simple mass-spring system with respect to effective parameters	136

5.2.3 x -directional parameters: resonant mass density	137
5.2.4 y -directional parameters: resonant stiffness	139
5.2.5 Explanation for simultaneous monopolar/dipolar resonances.....	142
5.3 Unit Cell Analysis Based on Transfer Matrix Method	143
5.3.1 Negative mass in the transverse direction: for hyperbolic dispersion	144
5.3.2 Extreme stiffness in the propagating direction: for total transmission.....	145
5.4 Physical Explanation on Super-Resolution Imaging by Hyperbolic Dispersion	146
5.5 1-D Total Transmission Condition due to Impedance Matching Condition	148
5.6 Numerical Simulations of Super-Resolution Imaging	151
5.7 Experimental Verification.....	153
5.8 Summary	160
<CHAPTER 6> CONCLUSIONS	175
APPENDIX A. Derivation of the N^{th} power of the unimodular matrix	179
REFERENCES.....	182
ABSTRACT (KOREAN).....	191
ACKNOWLEDGEMENTS.....	193

LIST OF TABLES

Table 4.1 Values of M_{al} , K_{al} , etc.....	108
Table 4.2 Structural parameters of chosen unit cells and their transmission/phase shift values.....	109
Table 5.1 The calculated values for mass and stiffness parts of the analytical mass-spring model from the continuum unit cell.	162
Table 5.2 Wave properties in the wave propagation direction (y direction) of the two media	162

LIST OF FIGURES

Fig. 2.1 1-D periodic mass-spring lattice.	23
Fig. 2.2 (a) Dispersion relation of the mass-spring lattice. (b) Dispersion relation of the irreducible Brillouin zone with real (black solid line) and imaginary (purple dotted line) components.	24
Fig. 2.3 2-dimensional simple mass-spring model with different periodicity and spring constants in the x and y directions.	25
Fig. 2.4 (a) Dispersion surface for the 2-dimensional lattice. The irreducible Brillouin zone is denoted with Greek letters Γ , X , and M . (b) Dispersion surface of the first Brillouin zone. The black contours are EFCs that show the wavenumber components at the target frequencies denoted in the figure. The arrows denote the group velocity vectors.	26
Fig. 2.5 Schematic drawing for a dipolar resonator and its equivalent rigid mass with effective mass property.	27
Fig. 2.6 Schematic drawing for a monopolar mechanical resonator and its equivalent spring model having effective stiffness.	28
Fig. 2.7 Combined lumped element model with local resonators and its equivalent simple mass-spring model with effective parameters.	29
Fig. 2.8 (a) Dispersion curve for a simple mass-spring lattice with frequency dependent effective mass and constant stiffness. (b) Dispersion curve for a simple mass-spring lattice with constant mass and frequency dependent	

effective stiffness.....	30
Fig. 2.9 Dispersion curve for a simple mass-spring lattice with frequency dependent effective mass and stiffness specially tuned to have overlapped negative region to yield negative curve.	31
Fig. 2.10 Displacement plots of the particles for (a) double-positivity, (b) single-negativity where q is complex, (c) single-negativity where q is purely imaginary, and (d) double-negativity cases with respect to time variance where $t_1 < t_2 < t_3$. The group and phase velocities are denoted by V_g and V_p , respectively. All plots are calculated by a finite lattice composed of 30 mass elements.	32
Fig. 3.1 Schematic drawing for the transfer matrix calculation.	66
Fig. 3.2 (a) Dipolar resonator with springs attached on both sides to represent the continuum unit cell which contains both density and stiffness components. (b) Simplified model for the transfer matrix definition.	67
Fig. 3.3 (a) Monopolar resonator with rigid masses attached on both sides to represent the continuum unit cell which contains both density and stiffness components. (b) Simplified model for the transfer matrix definition.	68
Fig. 3.4 (a) Infinite series of mass-spring containing effective properties. (b) Schematic drawing to calculate the mechanical impedance of the M_{eff} substructure. (c) Schematic drawing to calculate the mechanical impedance of the K_{eff} substructure. (d) Schematic drawing to retrieve effective impedance term from an arbitrary material.	69

Fig. 3.5 Lumped element model composed of unit cells embedded within continuum outer elastic medium for wave transmission analysis.....70

Fig. 3.6 Numerical simulation model (also experimentally feasible) to calculate the transfer matrix components.71

Fig. 3.7 (a) Dipolar cell design for single-phase continuum material. (b) Dipolar resonance mode shape near the resonance frequency.72

Fig. 3.8 (a) Monopolar cell design for single-phase continuum material. (b) Monopolar resonance mode shape near the resonance frequency.73

Fig. 3.9 Numerical analysis for the dipolar cell. (a) (From top to bottom) Dispersion curve, relative impedance, and transmission spectrum retrieved by the transfer matrix method. (b) Effective parameters retrieved by the transfer matrix method.74

Fig. 3.10 Numerical analysis for the monopolar cell. (a) (From top to bottom) Dispersion curve, relative impedance, and transmission spectrum retrieved by the transfer matrix method. (b) Effective parameters retrieved by the transfer matrix method.75

Fig. 3.11 (a) Dipolar and (b) monopolar cells retrieved with homogenized material assumption.....76

Fig. 3.12 (a) Dipolar and (b) monopolar cells retrieved by other models (monopolar and dipolar, respectively).....77

Fig. 4.1 (a) Schematic drawing of the Generalized Snell’s law (b) Beam steering by the elastic metasurface composed of unit cells stacked together within a

subwavelength layer.	110
Fig. 4.2 Unit cell consisting of two independent substructures, the M_{eff} - and K_{eff} - substructures ($d=6$ mm, $h=10$ mm, thickness=0.5 mm, and l,w : design parameters). (c) Analytic mass-spring model of the unit cell composed of M_{eff} - and K_{eff} -substructures.....	111
Fig. 4.3 Substructures for independent tuning of mass and stiffness. (a) M_{eff} - substructure and its eigenmode (dipolar mode) at 100 kHz. (b) K_{eff} - substructure and its eigen mode (softening mode) at 100 kHz. The black arrows within the eigenmode plots represent the vector magnitude of displacements. (c, d) Graphs of how effective parameters (M_{eff} and K_{eff}) change at the target frequency of 100 kHz depending on the two geometrical parameters w and l , respectively. (e,f) Contour plots of M_{eff} and K_{eff} , respectively, determined by the geometrical parameters w and l	112
Fig. 4.4 Superposition of retrieved parameters from discrete substructures. (a) Numerically retrieved effective parameters for discrete substructures. (b) Superposition of the retrieved parameters.	113
Fig. 4.5 Transmission and phase shift of metasurfaces consisting of each substructure only. (a) Simulation set-up with a metasurface composed of only the M_{eff} -substructures and its corresponding analytic mass-spring model. (b) Another metasurface unit is composed of only the K_{eff} - substructures while maintaining the periodicity by replacing the M_{eff} -	

substructure with an aluminum block.....	114
Fig. 4.6 Concept of rule of mixture applied to the substructure. (a) The layered composite consisting of metal and air. (b) The K_{eff} -substructure and its analogous model to be calculated as mixture of layered stacks. (c) The calculated stiffness and mass density properties with respect to l	115
Fig. 4.7 Comparison of off-centered triple slits with single-slit unit cells. (a) The original unit cell having off-centered multiple slits and its effective properties plotted as functions of the slit length l . (b) A single-slit unit cell to be compared with the original unit cell in (a).....	116
Fig. 4.8 (a) Dispersion curves of a substructured unit cell with $w=0.5$ mm and $l=2.5$ mm for its 1 st Brillouin zone. (b) Numerically retrieved effective stiffness and mass for the unit cell. The magenta line denotes the target frequency of 100 kHz.	117
Fig. 4.9 (a) Discrete mass-spring model of unit cells within continuum outer elastic medium. (b) Corresponding numerical simulation with actual elastic metasurface structure embedded within continuum elastic medium.	118
Fig. 4.10 The wave transmission plots for various geometric parameters with the specific simulation set-up. (a) The whole simulation set-up. (b) Various plots for the cases of transmissions less than unity.....	119
Fig. 4.11 Frequency-dependent transmission spectra estimation for (a) a single cell and (b) multiple cells.	120
Fig. 4.12 (a) The contour plots of impedance ($Z_r= Z_s/Z$) and phase velocity (V_p)	

plotted on the $M_{eff}-K_{eff}$ plane. (b) The contour plots of transmission and phase plotted on the $M_{eff}-K_{eff}$ plane. In (b), the $Z_r=1$ line indicates the curve of matched impedance and the $m=1, 2,$ and 3 lines indicate the satisfied tunneling condition. For (a,b), the analytic model was used for calculation.

..... 121

Fig. 4.13 Transmission/Phase spectra and the phase shift range along the impedance matching line for (a) $N=1$, (b) $N=2$, (c) $N=3$, and (d) $N=4$ case.

..... 122

Fig. 4.14 Characteristics on functions of geometrical parameters from the simulation. (a) Semi-analytical values of relative impedance and phase velocity from effective parameters retrieved in Fig. 4.3(e-f). (b) Numerically calculated contour plots of transmission and phase on the $l-w$ plane. The transmission and phase shift of the selected 12 unit cells exhibiting $\pi/6$ phase steps. The insets sketch the unit cells #1 and #11, which have extreme l values. (c) The phase simulation plots for odd-numbered unit cells corresponding to the phase shift of multiples of $\pi/3$.

..... 123

Fig. 4.15 The phase simulation plots for odd-numbered unit cells corresponding to the phase shift of multiples of (a) $\pi/3$ and (b) $\pi/4$ 124

Fig. 4.16 Engineering longitudinal ultrasonic beam by elastic metasurface. (upper) The two-dimensional simulation of refraction with (a) $d\varphi/dy=\pi/6h$, (b) $d\varphi/dy=\pi/8h$, and (c) $f_l=0.15m$ cases. The corresponding phase profiles are

also shown below.....	125
Fig. 4.17 Simulations for various incident angles of longitudinal sources where (a) $\theta_i=0^\circ$, (b) $\theta_i=10^\circ$, and (c) $\theta_i=-10^\circ$	126
Fig. 4.18 Analysis on the ratio of mode conversion. (a) Analytic model to calculate power (left). Normalized power and amplitudes on functions of refracted angle (right). (b) Simulations on various transmitted angles.....	127
Fig. 4.19 Experimental set-up. (a) The fabricated elastic metasurface structure and the magnified image showing the details of a unit cell. (b) The experimental set-up with a giant magnetostrictive patch transducer (MPT) for generating ultrasonic 100 kHz S_0 wave. The measurement is carried out by the laser scanning vibrometer.	128
Fig. 4.20 Comparison of numerical and experimental results obtained for the rectangular regions marked in Figs. 4.17(a,c). Transient simulation results and experimentally retrieved sequential images for (a) the beam steering case considered in Fig. 4.17(a), and (b) the beam focusing case considered in Fig. 4.17(c).	129
Fig. 4.21 Post-processing with the experimental results. (a) For the refraction case, the original signal is extracted at the point denoted with the black dot. Although the raw data contain minor peaks of noises, the dominant frequency (target frequency) component of the whole wavelet is 100 kHz. This is confirmed by Fast-Fourier-Transform (FFT) as shown in the figure. (b) The same procedure has been demonstrated for the focusing case.	130

Fig. 5.1 Concept Schematic of total transmission subwavelength imaging with hyperbolic elastic metamaterial. The constitutive properties of its unit cell are presented in the box with red dashed lines. 163

Fig. 5.2 (a) Mass-spring model of unit cell configuration. (b) Displacement notations and a set of masses to be considered as a new unit cell for deriving the parameters. Its effective mass and stiffness terms are equivalently represented in a simple mass-spring system in the right..... 164

Fig. 5.3 (a) Analytical mass-spring model and its realization in continuum body. (b) The two translational resonance eigenmodes: in-phase (left) and out-of-phase (right). Lumped element transfer matrix model for the (c) x -direction and (d) y -direction 165

Fig. 5.4 Numerical analysis for the cell in the x -direction. (a) (From top to bottom) Dispersion curve, relative impedance, and transmission spectrum retrieved by the transfer matrix method. (b) Effective parameters retrieved by the transfer matrix method. 166

Fig. 5.5 Numerical analysis for the cell in the y -direction. (a) (From top to bottom) Dispersion curve, relative impedance, and transmission spectrum retrieved by the transfer matrix method. (b) Effective parameters retrieved by the transfer matrix method. 167

Fig. 5.6 (a) Dispersion curves for the Γ -X and Γ -Y directions. The mismatched resonant bandgap (shaded region) causes highly anisotropic properties. (b) Equi-frequency contours in a range of frequency. The white contour

represents equi-frequency contour of the isotropic aluminum plate at 35.48 kHz.	168
Fig. 5.7 Numerical set-up for transmission computation and transmission curve for different number of unit cells.	169
Fig. 5.8 (a) One-source simulation with a 20 mm-wide line source generating the S_0 wave. The zoomed plots inside the metamaterial propagation is also presented in the right side. (b) Two-source simulation with the same sources separated (center-to-center) by 56 mm is shown. The color plot is in unit of the absolute y -directional stress ($ \sigma_{yy} $) where the input power is 100 Pa in the y direction.	170
Fig. 5.9 (a) Numerical simulation for two sources as close as 1 lattice constant (14 mm or 0.09λ). The specific parameters are presented in the right side. All the simulation set-up and condition were the same as those stated in the manuscript. (b) Obtained intensity profiles conforming the subwavelength imaging capability.	171
Fig. 5.10 Additional simulations for different thicknesses (not belonging to the Fabry-Perot resonance or finite resonance) of elastic metamaterial lenses. Thicknesses of 7 cells ($\approx 1\lambda$) and 17 cells ($\approx 2.43\lambda$) are considered. The resolved images are clearly observed in all figures.	172
Fig. 5.11 (a) Fabricated hyperbolic elastic metamaterial lens. It consists of 21×10 unit cells. (b) Experimental set-up with magnetostrictive transducers and	

nickel patches that generate the S_0 wave. The middle of the figure-of-eight coil of the transducer is aligned with the nickel patch. The measurement is carried out by a laser scanning vibrometer.173

Fig. 5.12 (a) Obtained intensity profiles confirming the subwavelength resolution capability. As for the experimental data, the Gaussian regression method is applied. (b) Snapshots from animated images by laser scanning vibrometer software.174

<CHAPTER 1>

INTRODUCTION

1.1 Research Motivation

“Metamaterial” is a recently researched subject which breaks the limit of conventional materials by anomalous wave phenomena due to its artificially designed structures. Generally by the local resonance mechanisms, they exhibit extraordinary properties that cannot be realized by materials that exist in nature. The main principle is defined within subwavelength scale where the local oscillation reacts as though the metamaterial itself possesses extraordinary effective material properties. Ever since the first proposition of Pendry’s super lens [1] with doubly negative permeability and permittivity properties in electromagnetic regime, numerous works on the metamaterials have been carried out for decades and even extended to the acoustic and elastic regimes. Such striking properties initially enabled negative refractive index/refraction [2-6], super-resolution imaging [7-10], filtering [11, 12], tunneling [13, 14], and phase shifters [15, 16] in which all of them boosted the wave engineering technology in unprecedented ways. Then, this research field has been explosively expanded to yield hyperlenses [17-22], cloaking devices [23-26], zero-index materials [27-30], and even recently

developed metasurfaces [31-34] for higher compatibility in practical applications.

On the other hand, as for the elastic counterpart, it is also no exception that such innovative wave controlling techniques are significantly demanded, especially regarding the vast range of potential applications including bio-medical imaging and non-destructive evaluation. However, the extension of the metamaterials developed in acoustics and electromagnetics to the elastic regime so far has been seriously hindered due to lack of a methodology to exclusively manipulate the elastic constitutive properties: mass and stiffness. In fact, the local resonance mechanism and periodic configuration of elastic metamaterials can be suitably represented by linkage-based lumped element models where the elastic mass and stiffness properties are described as discrete rigid mass and deformable spring, respectively. Nevertheless, such form cannot be directly applied on continuum background for practical application due to low compatibility.

To resolve such limits, several researches have been performed by two main methods to realize such geometry from the lumped-element model to a continuum media: by perforating air holes in a single-phase medium [35-39], or by utilizing composites to demonstrate the local resonance effect [40-43]. In fact, the former is much more suitable in practical usage because of the fabrication feasibility. However, there still lies the fundamental complication to adopt the linkage principle into continuum media because of the intrinsic proportional coupling

between mass density and stiffness within continuum itself. In other words, conventional elastic metamaterials all suffer from the correlation between effective mass and stiffness that makes it difficult to implement only the desired properties.

In other words, the main problem stemming from the incapability of independent tuning is that there exists an inevitable correlation between mass and stiffness that hinders the delicate impedance matching condition. In particular, as in a situation that requires extreme parameters for the desired phenomena, this inevitably causes huge impedance mismatch between the background medium and the working metamaterial structure. Owing to such limits, adaptation of the elastic metamaterials into practical environments have been seriously hindered.

1.2 Research Objectives

Motivated by the aforementioned limits in elastic metamaterials, this thesis is dedicated to designing novel substructures that enable exclusive tuning of only the desired property (mass or stiffness). In other words, the substructures conceptually contribute to the breaking of the intrinsic proportional density-stiffness relation in continuum media. The main principle is to spatially decompose the functioning regions into independent substructures. In this way, various combinations of the substructures as the basic building blocks will form innovative metamaterial unit cells for exact property tuning at the target frequency. With proper knowledge of the substructures and their physical mechanism as a combined cell, one will be able

to build various elastic metamaterial structures for innovative applications.

The research objectives can be summarized in more details as follows.

<Theoretical Objectives>

1. How to design a mass/stiffness tuning continuum substructure

The local resonance mechanism for manipulating the effective properties can be represented with the lumped element model containing rigid mass and spring. For practical realization, this model should be correspondingly realized to a continuum version. To maximize the practicability, the continuum structure must be a single-phase medium, which in turn hampers discrete materialization of the continuum materials into the linkage structures. Thus, a robust design supported by a concrete physical basis is crucial. Most of all, each substructure must be capable of efficiently tuning only one property while the other remains constant.

2. Method to define the discrete lumped element structure for their in-depth analysis

The continuum materials possess the characteristics of both the mass and spring simultaneously. Therefore, not only the original lumped model should be considered but also its actual response in the continuum form must be explicitly verified. Specifically, the complex structural geometries within elastic metamaterials react differently in all frequencies. Accordingly, newly modified models that match each different substructure must be devised. Moreover, the wave

characteristics (such as characteristic impedance, dispersion relation, transmission coefficient, etc.) of each model must also be established by in-depth analysis.

3. A concrete method to retrieve their effective properties

To predict the wave characteristic of a material, defining its effective dynamic properties is a critical procedure. Although conventional models employ long-wavelength assumption to omit some parameters to conveniently define the metamaterials, this method cannot always predict the exact information of the metamaterial. Especially near the resonance frequencies where the extreme properties significantly develops, conventional methods fail to define and predict the wave phenomena. Thus, not only a justifiable assumption but also a concrete model to represent the metamaterial and retrieve its effective properties is necessary.

<Application Objectives>

1. Proposition of high transmission elastic metasurface

To adapt to the leading trend of miniaturizing the conventional bulk metamaterial to practical applications, the metasurface concept has received paramount attention recently. Although it remains at its infancy stage for the elastic regime, such concept is highly desirable given a lot of potential for numerous ultrasonic wave-based applications. In that context, the challenging issue is to guarantee both high transmission and adequate phase changes, which are the essential conditions for a

metasurface to function properly. In other words, realizing inverse proportionality of (amplified) mass and (lowered) stiffness is critical for a properly working elastic metasurface.

2. Proposition of high transmission hyperbolic elastic metamaterial lens for super-resolution imaging

Fine quality super-resolution (deep subwavelength scale) imaging of high transmission and low loss is crucially demanded for the broad range of ultrasonic imaging applications including non-destructive evaluation and biomedical screening. However, such performance is yet unable to be achieved with conventional method, which can have resolution up to only half the wavelength (0.5λ) and suffers from significant loss. Although few existing elastic metamaterial lenses proved their capability of subwavelength imaging, they still suffer from low resolution/transmission. Above all, their huge sizes and curved geometries hinder direct installation upon inspecting specimens, severely losing their practicality.

1.3 Outline of Thesis

The thesis is organized as follows.

In <Chapter 2>, the theoretical background of periodic system will be reviewed. Because the basic elastic metamaterial structures can be modeled by a simple periodic lumped element (composed of mass and spring) model, its harmonic wave

analysis will be presented. In addition to the simple mass and spring system, we explain how local resonators can be installed within existing mass and spring to induce metamaterial properties. Furthermore, the fundamental underlying mechanisms for each mass and stiffness tuning technique will be discussed.

In **<Chapter 3>**, in-depth study on the continuum substructures based on its corresponding lumped element model will be given. We introduce an explicit transfer matrix method for the lumped element model to investigate the harmonic dynamics. Furthermore, how to define the characteristic impedance, dispersion relation, and the transmission coefficient by the transfer matrix is given. In this way, each continuum substructure can be conveniently defined by the transfer matrix, which in turn provides its intrinsic information. Most of all, a concrete method to retrieve the effective properties using the transfer matrix is given. Because this method is based on the actual boundary responses of the unit cell, the effective properties for any metamaterials can be calculated with respect to the working frequency as long as its transfer matrix can be defined.

In **<Chapter 4>**, we present a subwavelength scale elastic metasurface for both the full transmission and abrupt phase shift to anomalously control refracted ultrasonic beams. To simultaneously achieve low phase velocity and impedance-matched condition, which are intrinsically in opposite relation within normal elastic materials, the substructuring mechanism is utilized. When assembled into a

subwavelength elastic metasurface, these substructures provide inverse proportionality of (amplified) mass and (lowered) stiffness to obtain both the whole 2π phase shift as well as full transmission. To validate our approach, the anomalous steering and focusing of in-plane longitudinal ultrasonic beams are confirmed both numerically and experimentally. The substructured-metasurface concept will offer a new design framework for much wider range of elastic metasurface applications.

In <**Chapter 5**>, we present total transmission subwavelength imaging with a hyperbolic elastic metamaterial lens. The elastic parameters (mass density and stiffness) are delicately tuned and realized with our explicit analytical method by a mass-spring model including two-dimensional stiffness definition. The essential conditions for super-resolution (by hyperbolic dispersion relation with negative effective mass density) and total transmission (by extremely large effective stiffness) are successfully realized. The fabricated metamaterial lens is capable of resolving subwavelength symmetric Lamb waves (up to 0.09λ) and the subwavelength imaging with total transmission is confirmed by both finite element simulation and experiment. As for the experiment, wave propagation in its inside structures are visualized via a laser scanning vibrometer to prove its ability of directly transmitting subwavelength details. The proposed elastic metamaterial lens will bring forth significant guidelines for ultrasonic imaging techniques.

In <**Chapter 6**>, the overall conclusion of this dissertation is presented.

<CHAPTER 2>

WAVE PROPAGATION IN PERIODIC LUMPED ELEMENT STRUCTURES

2.1 Chapter Overview

This chapter will review the wave propagation physics in periodic lumped element structures. In fact, the researches on periodic medium dates back to decades for its capability of inducing extraordinary wave phenomena. As much as the wave physics in continuum medium, theoretical foundations on periodic systems have received more and more attention for their relevance on analyzing composite materials (for aircraft structures), impact resistant cellular materials, periodic foundations for buildings, and multispan bridges, etc.

While applied researches in various kinds of periodic media have been abundant in recent years, this chapter will cover the exclusive model to generally define the recently emerging elastic metamaterials. Especially, the added feature of exhibiting distinguished local resonances for mass (dipolar resonance) and stiffness (monopolar resonance) manipulation will be thoroughly discussed.

2.2 1-D Lumped-Element Lattice

Analogous to the transmission line model in the electromagnetic regime, the lumped element (mass and spring) model can generally represent the wave physics of periodic system in the elastic regime. Such model is suitable because the metamaterials are not only governed by the local resonance mechanism but also by the periodic nature. In this section, for basic analysis, we will discuss the periodic system only composed of mass and spring without local resonances. In fact, this model is capable of describing the physics of phononic crystals (PCs) [44, 45] (artificial structures having periodically arranged inclusions in matrix, having extraordinary refraction phenomena owing to their unusually structured dispersion curves), which is still a substantially large research topic as non-resonant type periodic structures for phonon manipulation.

Specifically, the periodicity can cause Bragg scattering [46], leading to extraordinary wave phenomena that had not been observed in general materials. For example, the periodic nature of PCs can create a complete band gap in which wave propagation is forbidden. Also, negative refraction phenomena have been observed in PC structures [47-51] owing to their unusually structured dispersion curves. As a result, PCs have been widely used in many elastic wave based applications, including efficient filters [52], wave guiding [53], and tunneling devices [54]. Moreover, by using PCs, numerous works have been dedicated to invention of devices that would have been impractical with conventional wave technology, such as flat superlenses for subwavelength imaging [3, 55, 56] and

wave collimators [57].

To understand the basic principles of such periodic systems, Fig. 2.1 will be considered. In addition, only the 1-dimensional (in the x -direction) physics of the lumped element system will be dealt with. The system is composed of masses M and springs K and the periodicity is d . The overall dynamic behavior can be investigated by considering the equation of motion for the n th mass as

$$M \frac{\partial^2 u_n}{\partial t^2} = K(u_{n+1} + u_{n-1}) - 2Ku_n. \quad (2.1)$$

Here, the particle displacement u_n in harmonic motion will be defined as

$$u_n = Ae^{i(\omega t - qnd)} \quad (2.2)$$

where q is Bloch wavenumber [46]. Owing to the periodic nature, the particles are governed by the Bloch-Floquet [46] theory, thus resulting in

$$u_{n-1} = u_n e^{iqd}, \quad (2.3a)$$

$$u_{n+1} = u_n e^{-iqd}. \quad (2.3b)$$

Also, from Eq. (2.2), it can be observed that u_n has also periodicity of 2π with respect to the wavevector q . Therefore, the spatial periodicity induces periodic wavevectors for a given temporal frequency in the harmonic motion.

2.2.1 Dispersion relation analysis

To thoroughly analyze the characteristics of a PC structure, the dispersion relation must be calculated. Substituting Eqs. (2.3a-b) and (2.2) into Eq. (2.1) gives

$$-\omega^2 M u_n = K \left(e^{-iqd} + e^{iqd} \right) u_n - 2K u_n, \quad (2.4)$$

which can be modified to

$$\omega^2 M = 4K \sin^2 \left(\frac{qd}{2} \right). \quad (2.5)$$

By adopting a non-dimensional normalized frequency term $\Omega = \omega/\omega_0$ where $\omega_0 = \sqrt{K/M}$ finally yields the dispersion relation

$$\Omega^2 = 4 \sin^2 \left(\frac{qd}{2} \right). \quad (2.6)$$

Solving for the frequency by imposing certain range of wavenumbers provides the dispersion curve plotted in Fig. 2.2(a). As observed in the figure, the curves are periodic with periodicity of 2π and symmetric with respect to $qd=0$. In other words, at a given frequency, the system can have infinite values of periodic wavenumbers. In fact, due to the periodicity, the “first Brillouin zone” [46] ($q \in [-\pi/d, +\pi/d]$) can fully describe all the other regions. Similarly, facilitating the symmetry can also reduce the zone into the “irreducible Brillouin zone” ($q \in [0, +\pi/d]$).

The detailed plot of the irreducible Brillouin zone is shown in Fig. 2.2(b). Both the real and imaginary values of wavenumbers are plotted. Above the cutoff frequency ($\Omega=2$), the imaginary part starts to appear and the real part becomes constant. This “stopband” or “bandgap” above the cutoff frequency has complex values of wavenumber and thus the incoming waves become evanescent and decay in this region. As the frequency increases, so does the imaginary part, meaning that the

wave attenuation increases with frequency. In summary, such 1-D monoatomic periodic system behaves as a low-pass filter.

2.2.2 2-Dimensional dispersion relation: Equi-frequency contour (EFC)

The 1-D periodic structure can also be expanded to 2-D system [44] as described in Fig. 2.3. In this system, the governing equation can be written as

$$M \frac{\partial^2 u_{n,m}}{\partial t^2} = K_x (u_{n+1,m} + u_{n-1,m}) + K_y (u_{n,m+1} + u_{n,m-1}) - 2(K_x + K_y) u_{n,m}. \quad (2.7)$$

The particle displacement, similar to the 1-d case, can be expressed as

$$u_{n,m} = A e^{i(\omega t - \mathbf{k} \cdot \mathbf{d})} = A e^{i(\omega t - nq_x d_x - mq_y d_y)} \quad (2.8)$$

where $\mathbf{k} = nq_x \mathbf{i} + mq_y \mathbf{j}$ is the wavevector. Substituting Eq. (2.8) into Eq. (2.7)

gives

$$-\omega^2 M u_{n,m} = K_x (e^{-iq_x d_x} + e^{iq_x d_x}) u_{n,m} + K_y (e^{-iq_y d_y} + e^{iq_y d_y}) u_{n,m} - 2(K_x + K_y) u_{n,m}, \quad (2.9)$$

which can be further simplified to

$$\omega^2 M = 4K_x \sin^2 \left(\frac{q_x d_x}{2} \right) + 4K_y \sin^2 \left(\frac{q_y d_y}{2} \right). \quad (2.10)$$

For simplicity, we will consider $K_x = K_y$ and $d_x = d_y = d$ so that the 2-D system is quasi-isotropic. Assuming such condition modifies Eq. (2.10) into

$$\Omega^2 = 4 \left(\sin^2 \left(\frac{q_x d_x}{2} \right) + \sin^2 \left(\frac{q_y d_y}{2} \right) \right). \quad (2.11)$$

The results are depicted as dispersion surface in Fig. 2.4(a) with the frequency Ω denoted by the color map. This scheme provides conceptual visualization for one to conveniently see the dispersion relation in all directions. The surface indicates that waves propagating inside the periodic system can have infinite wave modes. Such representation provides good information for all wavenumbers in broad range of frequencies. The plot also illustrates both the first and irreducible Brillouin zone in 2-D perspective. Here, Γ , X, and M stands for the coordinates $(0,0)$, $(\pi,0)$, and (π,π) , respectively, in the $q_x - q_y$ plane.

In order to achieve better understanding of the wave propagation behavior, we examine the equi-frequency contours (EFCs) as plotted by black contours in Fig. 2.4(b). EFC is a configuration that displays the wavevectors at a specific frequency. From EFC, information for the energy propagation can be obtained by analyzing the group velocities. Regarding the definition of group velocity which is expressed as

$$\mathbf{v}_g = \frac{\partial \omega}{\partial q_x} \mathbf{i} + \frac{\partial \omega}{\partial q_y} \mathbf{j}, \quad (2.12)$$

it can be inferred that the group velocity vector is always perpendicular to the EFC in the direction of increasing frequency. In Fig. 2.3(b), the EFC becomes more circular as the target frequency decreases. This means that in the low frequency region, or long wavelength regime, the wavelength becomes much larger relative to

the periodicity so that the wave is less affected by the details of the system. Therefore, in this regime, the system behaves considerably isotropic in harmonic response, making the EFC to be circular.

2.3 1-D Lumped-Element Lattice with Local Resonators: Metamaterials

In this section, the key principle to compose metamaterials; the local resonators, will be covered. As proposed in previous works by Huang *et al.* [58, 59], Oh *et al.* [38, 60, 61], and Liu *et al.* [42], simple mass-in-mass system or geometrically designed internal resonators can induce unbounded range of effective mass or stiffness properties, respectively. Such extraordinary characteristics can allow negative refraction [39], super-resolution imaging [36, 62], focusing [40, 61], wave blocking [41, 43, 60, 63], and many other potential anomalous wave phenomena. In addition to the Bragg scattering (determined by the periodicity) which dominantly governs aforementioned simple mass-spring lattice, metamaterials are especially capable of manipulating the wave at any frequencies governed by the resonant frequencies of the internal resonators. The target frequencies are usually much lower so that the wavelengths are much larger than the unit cell (generally larger than 4 times the unit cell), so that long-wavelength assumption [64] can be applied. In this condition, the whole system can be regarded as to embody its effective properties.

The specific principles will be discussed in the next subsections.

2.3.1 Effective mass tuning by dipolar resonance

In this subsection, the fundamental principle for effective mass tuning will be discussed. Specifically, mass tuning is related to inertia (cf., Newton's second law $F = ma$). Therefore, the whole unit cell should exhibit dipolar resonance [41] where the internal resonator and the outer cell drastically move by out-of-phase motion above the resonant frequency. To demonstrate such motional dynamics, a mass-in-mass [65] structure as shown in Fig. 2.5 has been generally implemented. The primary goal is to express the response of the unit cell containing the local resonator as though it functions as a single "effective" mass M_{eff} with its displacement u , such that

$$F = M_{eff} \frac{\partial^2 u}{\partial t^2} \quad (2.13)$$

can be satisfied.

To investigate the physics of this system, the governing equation will be derived using the notations in the figure as follows.

$$m_m \frac{\partial^2 v}{\partial t^2} = k_m (u - v), \quad (2.14a)$$

$$M_m \frac{\partial^2 u}{\partial t^2} = F + k_m (v - u). \quad (2.14b)$$

Under harmonic wave condition, the Eqs. (2.14a-b) become

$$-\omega^2 m_m v = k_m (u - v), \quad (2.15a)$$

$$-\omega^2 M_m u = F + k_m (v - u). \quad (2.15b)$$

Substituting Eq. (2.15a) into (2.15b) and re-writing the result with respect to displacement term u yields,

$$F = -\omega^2 \left(M_m + \frac{m_m}{1 - \omega^2 / \omega_r^2} \right) u, \quad (2.16)$$

where $\omega_r = \sqrt{k_m / m_m}$ is the resonant frequency of the local resonator. Comparing this equation to Eq. (2.13), the effective mass is defined as

$$M_{eff} = M_m + \frac{m_m}{1 - \omega^2 / \omega_r^2}. \quad (2.17)$$

This infers that the rigid mass containing a local resonator can be regarded to possess frequency-dependent inertia, which is consequently expressed as “effective” mass.

2.3.2 Effective stiffness tuning by monopolar resonance

In this subsection, the mechanism to tune the stiffness part will be discussed. For the stiffness parameter, the underlying physics is related to the volume change (cf., Hooke’s law $F = kx$). Therefore, the key requirement is to demonstrate the monopolar resonance [58], which exhibits the overall volume change. In contrast to the dipolar resonance, it requires more complicated geometrical structures as depicted in Fig. 2.6 to induce the monopolar resonance. The local resonators are

geometrically connected to the main spring K_s by massless truss bars with pivots.

Similar to the mass tuning case, the final goal is to achieve

$$F = K_{eff} u, \quad (2.18)$$

so that the whole system can be regarded as a single spring with all the dynamic response expressed in the “effective” stiffness (K_{eff}) term.

To investigate the mechanism specifically, we first assume symmetric forces (like Hooke’s law) as in the figure so that the governing equations can be obtained as

$$F = 2 \left(K_s u + \frac{W}{H} k_s (v_r - v) \right), \quad (2.19a)$$

$$m_s \frac{\partial^2 v_r}{\partial t^2} = k_s (v - v_r). \quad (2.19b)$$

Here, we also assumed that the small resonators m_s move only in the y -direction so that their inertia terms have only y -directional components. Also assuming small displacements, the relation between displacement terms can be modified to

$$v = -\frac{W}{H} u. \quad (2.20)$$

Under time harmonic wave condition, Eq. (2.19b) becomes

$$-\omega^2 m_s v_r = k_s (v - v_r). \quad (2.21)$$

By substituting Eqs. (2.20) and (2.21) into Eq. (2.19a) and re-writing the result with respect to the displacement term u yields

$$F = 2 \left(K_s + \left(\frac{W}{H} \right)^2 \left(\frac{k_s \omega^2}{\omega^2 - \omega_r^2} \right) \right) u. \quad (2.22)$$

where $\omega_r = \sqrt{k_s/m_s}$ is the resonant frequency of the local resonators. Finally, comparing this equation with Eq. (2.18), the effective stiffness is defined as

$$K_{eff} = 2 \left(K_s + \left(\frac{W}{H} \right)^2 \left(\frac{k_s \omega^2}{\omega^2 - \omega_r^2} \right) \right). \quad (2.23)$$

Similar to M_{eff} case, K_{eff} is also confirmed to be frequency-dependent where significant variation occurs near the resonant frequency.

2.4 Wave Propagation Analysis for Metamaterials

Former subsections discussed how different kinds of special local resonators can modify a rigid mass and a deformable spring to achieve frequency-dependent M_{eff} and K_{eff} , respectively. In this section, detailed analysis on their behaviors and utilization to metamaterials will be discussed. As shown in Fig. 2.7, a series of lumped elements containing the aforementioned local resonators can be interpreted as a simple mass-spring lattice having effective properties. Although similar to the periodic mass-spring system discussed in Section 2.2, the unbounded effective parameters from the local resonators are the key fundamentals for anomalous wave phenomena in metamaterials. In fact, for such lattice with effective parameters, the governing Bloch relation in Eq. (2.5) can be modified to

$$\omega^2 M_{eff} = 4K_{eff} \sin^2\left(\frac{qd}{2}\right). \quad (2.24)$$

To examine how the parameters affect the wave propagation, further studies with dispersion relations formed by each effective parameter are provided.

First, a dispersion curve and its corresponding M_{eff} are shown in Fig. 2.8(a). Here, K_{eff} is remained constant to investigate the effect of only M_{eff} . As observed from Eq. (2.17), M_{eff} starts from $M_m + m_m$, which is the static total mass value at $\Omega = 0$. Then, M_{eff} experiences unbounded range of values near the resonance frequency (ω_r). Also, it should be noted that M_{eff} rapidly increases below ω_r and then starts from negative infinity just above ω_r . After recovering to positive values from the rapid increase, M_{eff} converges to M_m , which is the outer mass value. Owing to the trait of the M_{eff} curve, the dispersion curve experiences “resonance gap” near ω_r . Specifically, q first becomes complex just below ω_r due to the increased M_{eff} term. Above ω_r , q becomes purely imaginary due to M_{eff} 's negative value. The former gap can otherwise be named “Bragg-like bandgap” owing to the complex value of q . All these observation can be confirmed from Eq. (2.24) and Fig. 2.8(a).

Similarly, another dispersion curve and its corresponding K_{eff} is shown in Fig. 2.8(b). In contrast to M_{eff} , K_{eff} first experiences negative value just below ω_r ,

and then starts from positive infinite value just above ω_r . Because of this fact, the induced dispersion curve exhibits similar shape but different location of the resonance gap. Although the Bloch wavenumber q has both the complex and purely imaginary value near ω_r , passband starts from ω_r on contrary to the M_{eff} case. This is because in Eq. (2.24), q can have real values as long as K_{eff} term is positive. On the other hand, for the M_{eff} case, q became complex when M_{eff} exceeded a certain value.

Now, by combining only the negative regions of these two, double negativity phenomenon is investigated in Fig. 2.9. Double negativity is considered to be the most fascinating trait of the metamaterials for their unusual features that do not exist in nature. As can be observed in the figure, the negative branch has opposite signs between the phase velocity

$$V_p = d \sqrt{\frac{K_{eff}}{M_{eff}}} \left| \frac{\sin(qd/2)}{qd/2} \right|, \quad (2.25)$$

and the group velocity as in Eq. (2.12). This means that the phase momentum direction is opposite to the direction of energy propagation. To visualize such propagation effects of metamaterials, configurations of dynamic shapes of elements are provided in Fig. 2.10.

Fig. 2.10(a) shows the wave propagating shapes for double-positivity case, which is similar to that of normal materials. The wave phase moves (defined by phase velocity) in the same direction as the wave propagating direction (defined by group

velocity). In Fig. 2.10(b), not only decaying but also fluctuation of the lattice occur simultaneously due to the complex q , composed of both real and imaginary value. This Bragg-like bandgap has attenuation factor which is determined by the imaginary component. On the other hand, the resonance gap phenomenon is shown in Fig. 2.10(c). Here, in contrast to the former bandgap, the wave field has only the decaying motion without fluctuation because q has only the imaginary value. Thus, this gap may be more efficient in some applications. Finally, the double-negativity inducing negative phase velocity is described in Fig. 2.10(d). The peculiarity of double negativity comes from manipulating the wave to propagate in the desired direction while guiding the phase to propagate in the opposite direction. This characteristic can otherwise be described to have negative refractive index. Overall, with delicately designed local resonators to exclusively tune each elastic parameter, the design domain for wave manipulation can be extensively broadened.

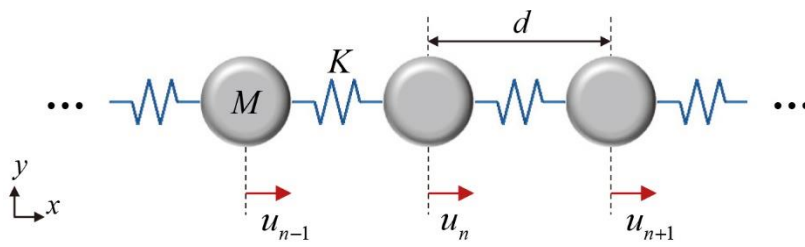


Fig. 2.1 1-D periodic mass-spring lattice.

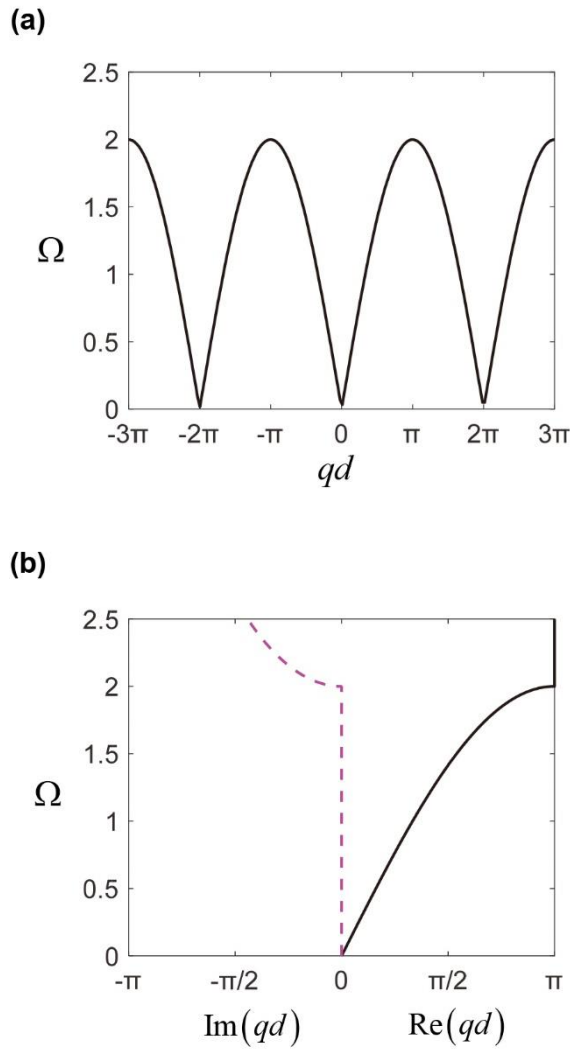


Fig. 2.2 (a) Dispersion relation of the mass-spring lattice. (b) Dispersion relation of the irreducible Brillouin zone with real (black solid line) and imaginary (purple dotted line) components.

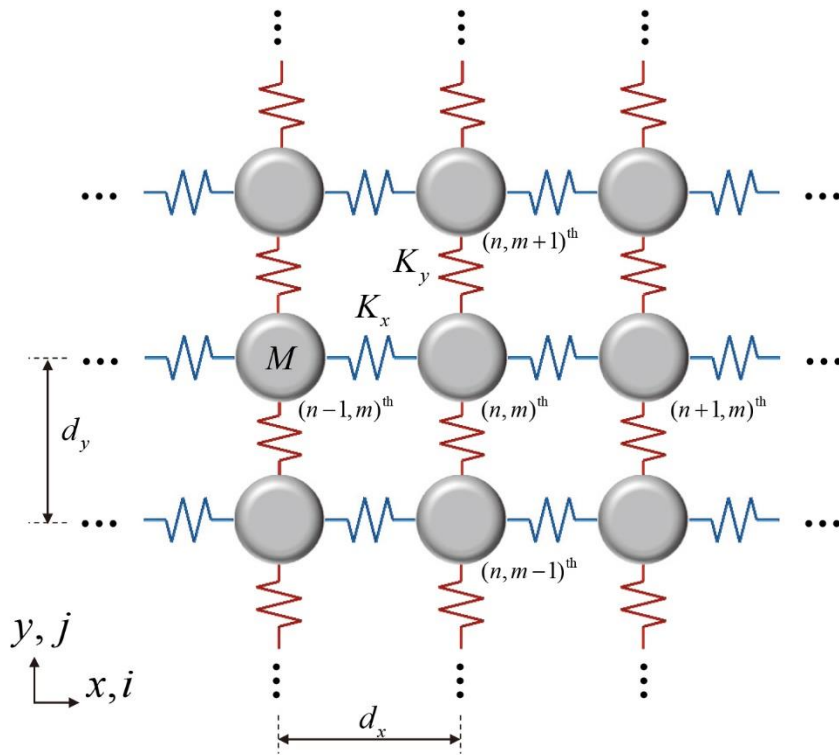


Fig. 2.3 2-dimensional simple mass-spring model with different periodicity and spring constants in the x and y directions.

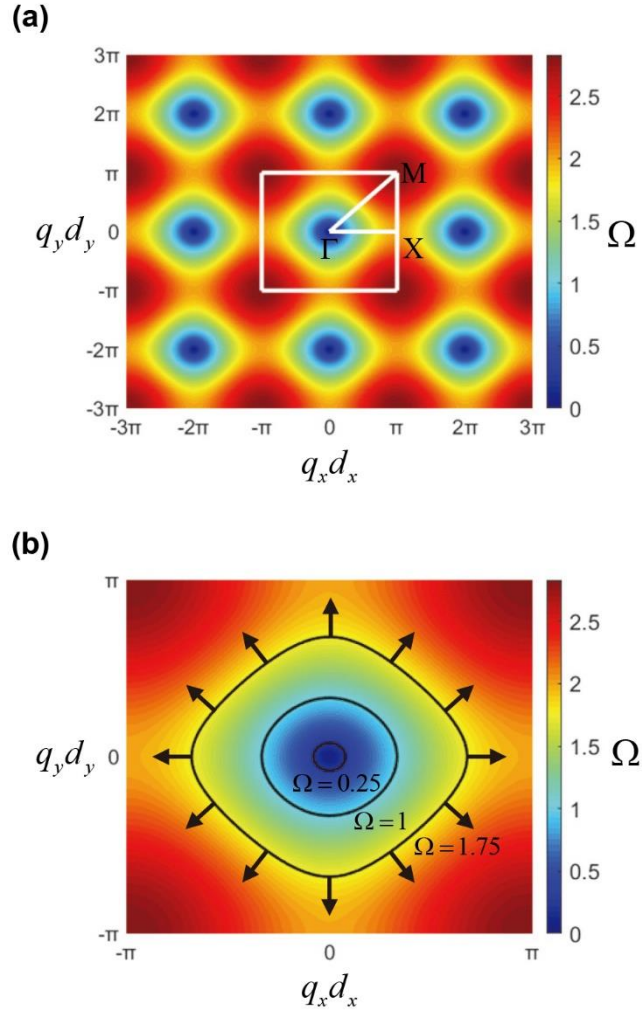


Fig. 2.4 (a) Dispersion surface for the 2-dimensional lattice. The irreducible Brillouin zone is denoted with Greek letters Γ , X , and M . (b) Dispersion surface of the first Brillouin zone. The black contours are EFCs that show the wavenumber components at the target frequencies denoted in the figure. The arrows denote the group velocity vectors.

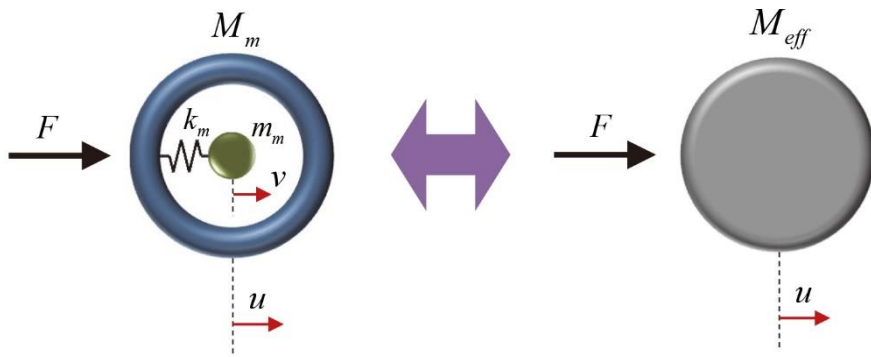


Fig. 2.5 Schematic drawing for a dipolar resonator and its equivalent rigid mass with effective mass property.

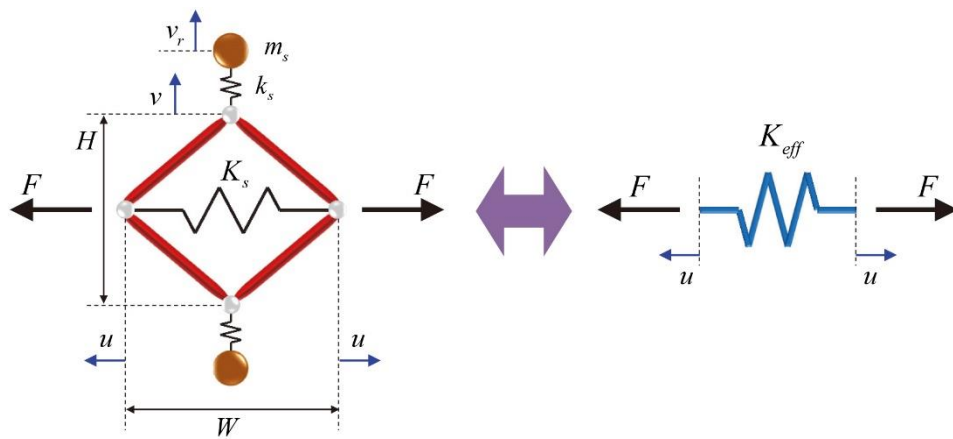


Fig. 2.6 Schematic drawing for a monopolar mechanical resonator and its equivalent spring model having effective stiffness.

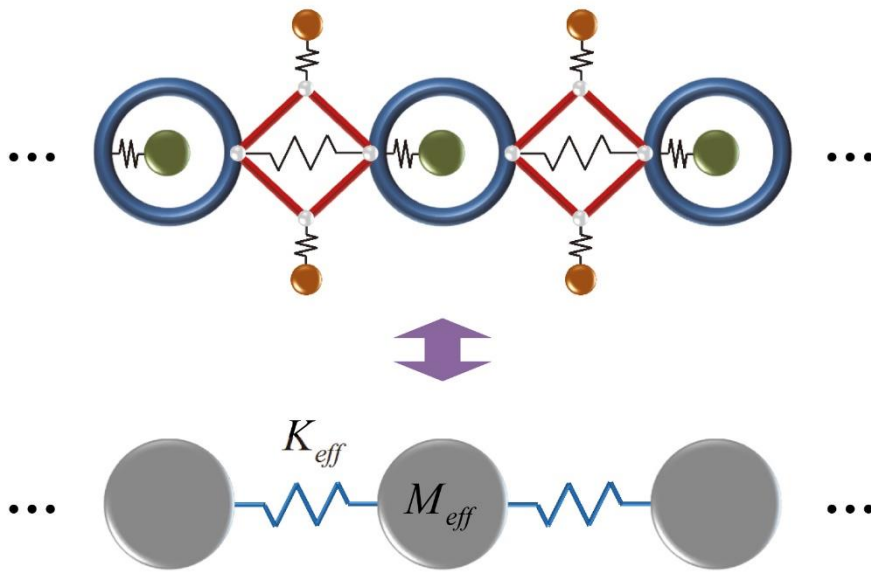


Fig. 2.7 Combined lumped element model with local resonators and its equivalent simple mass-spring model with effective parameters.

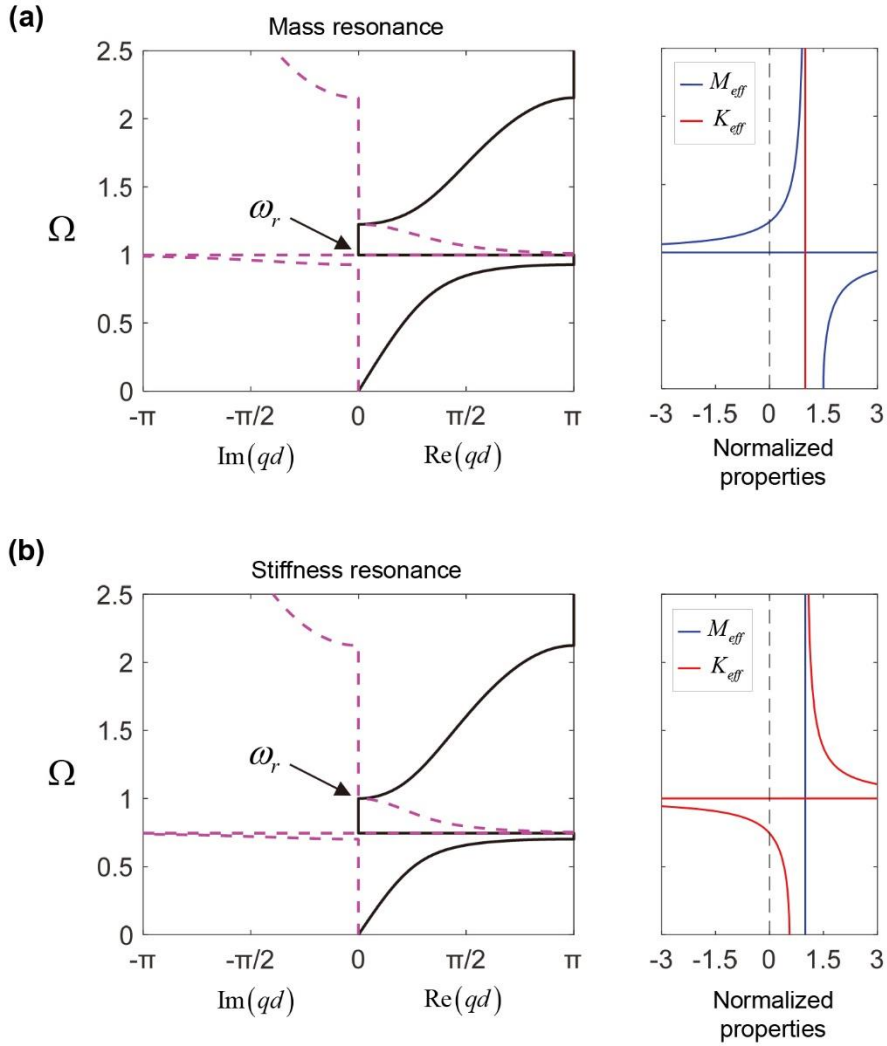


Fig. 2.8 (a) Dispersion curve for a simple mass-spring lattice with frequency dependent effective mass and constant stiffness. (b) Dispersion curve for a simple mass-spring lattice with constant mass and frequency dependent effective stiffness.

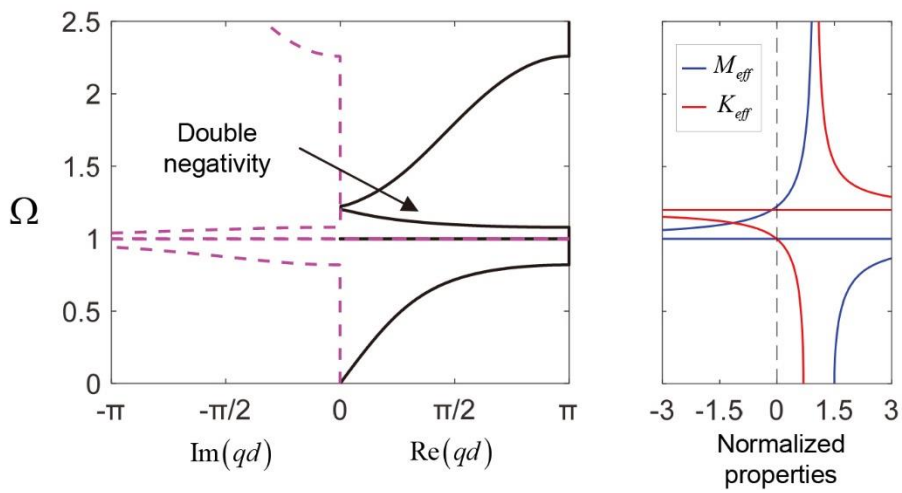


Fig. 2.9 Dispersion curve for a simple mass-spring lattice with frequency dependent effective mass and stiffness specially tuned to have overlapped negative region to yield negative curve.

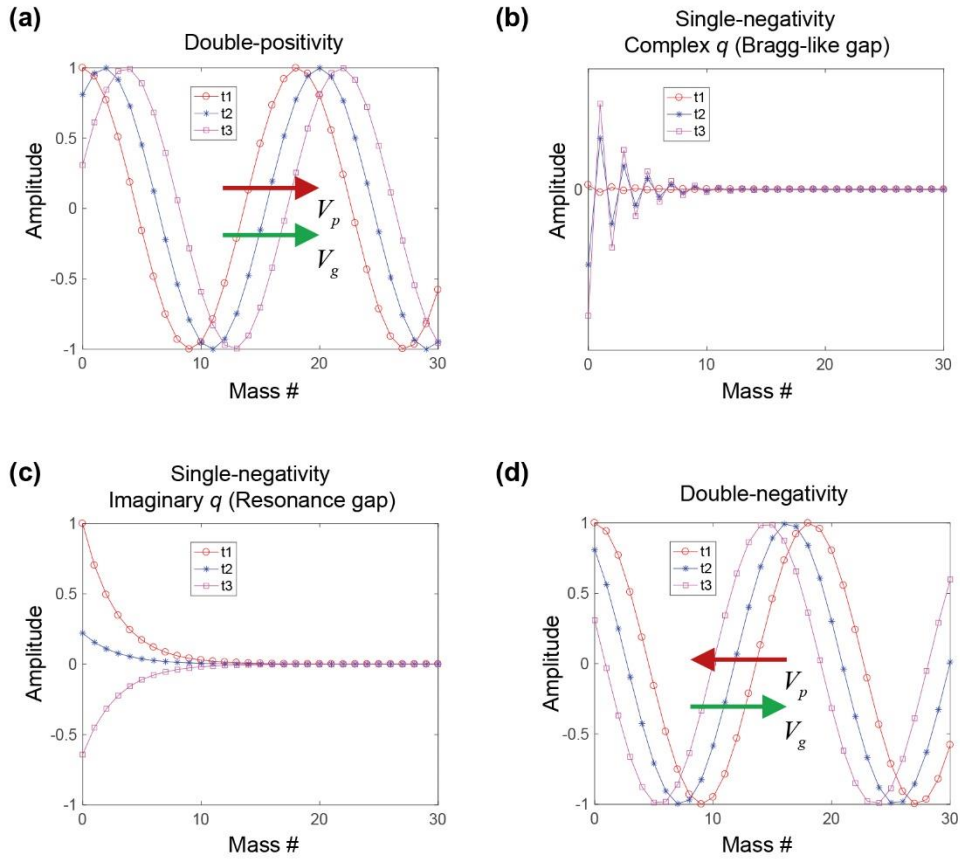


Fig. 2.10 Displacement plots of the particles for (a) double-positivity, (b) single-negativity where q is complex, (c) single-negativity where q is purely imaginary, and (d) double-negativity cases with respect to time variance where $t_1 < t_2 < t_3$. The group and phase velocities are denoted by V_g and V_p , respectively. All plots are calculated by a finite lattice composed of 30 mass elements.

<CHAPTER 3>

PROPOSITION OF TRANSFER MATRIX METHOD FOR SUBSTRUCTURE DESIGN AND ANALYSIS

3.1 Chapter Overview

To fully comprehend all the underlying behaviors of elastic metamaterials, characterizing the “effective properties” is crucial. By this definition, a metamaterial is assumed to function as a homogeneous medium with equivalent effective material properties. Most importantly, this assumption is valid only in the long-wavelength regime where relatively large wavelength penetrates through the unit cell without being affected by microscopic geometries, so that the details of metamaterials can be omitted. In other words, the unit cell must be within quarter wavelength scale to be defined as metamaterials with effective properties.

In fact, there have been three major studies to calculate the effective properties and predict the wave characteristics arising from themselves.

1. The very basic technique is by implementing analytic models composed

of lumped mass and spring elements. This modelling is a powerful approach to accurately reflect the structural dynamics arising from local resonators. Oh *et al.* [38], and Lee *et al.* [66], established explicit models to investigate various structures and their characteristics. However, such methods were based on calculating the mass and stiffness components in the static regime, thus inevitably yielding severe errors in the dynamic responses especially in the high frequency ranges.

2. Another technique that considers the dynamic responses is by “wave-field-averaging” method [41]. Instead of using an analytical method that calculates the mass and stiffness based on geometric parameters [38], this method retrieves the effective parameters by calculating the external boundary responses at every frequency. This method is especially efficient for an elastic unit cell that accompanies the frequency-dependent structural dynamics that stems from the complex local properties, which can be conveniently integrated as the global response along the external boundaries. However, conventional methods were focused on just averaging the unit cell and not considering the inner mechanisms and physics. In other words, concrete principles and tuning mechanisms of effective parameters and their relation with global responses had not been investigated.

3. Another realistic and practical technique is by “S-parameter retrieval method” [67, 68]. The properties of the target material is calculated by measuring the reflected and transmitted field. The reason that this method is practical is

because such wave fields can be conveniently obtained not only by simulations but also from experiments. Although recently proposed S-parameter retrieval method [66] is capable of calculating complex elastic tensorial fields (even the off-diagonal terms), this method is advantageous only within the non-resonant regime. In other words, when the target frequency gets close to the Bragg-gap or resonance gap regime, the retrieved properties are physically meaningless because this method assumes the target material to be a “homogeneous continuum” structure so that the anomalous phenomena cannot be expressed in the normal material properties.

To overcome the shortcomings and combine the advantages of the aforementioned methods, a new method is proposed in this chapter to precisely represent elastic metamaterials and thus accurately calculate the effective properties. First, all the continuum elastic metamaterials are modeled by the lumped elements to functionally divide the unit cell into mass and stiffness parts. Then, to define their dynamic responses like wave-field-averaging and S-parameter retrieval method, explicit transfer matrix method is employed. By constructing various transfer matrix and establishing their applications to wave harmonics, concrete definitions for metamaterial impedance and dispersion relation and also wave transmission analysis are presented in this chapter.

3.2 Transfer Matrix Method

Transfer matrix method is a powerful tool to evaluate the reflected and transmitted wave fields of multiple cells and even to characterize the unit cell itself. The

transfer matrix is defined by considering the continuity of displacements (or velocity) and forces at the boundaries of dissimilar media. Therefore, such method can be implemented not only for harmonic analysis but also transient analysis for any numbers of layers or cells [69].

First of all, it may be worthwhile to review this method implemented in a normal homogeneous elastic medium as shown in Fig. 3.1. The transfer matrix \mathbf{T} is defined as

$$\begin{bmatrix} u_{x+d} \\ F_{x+d} \end{bmatrix} = \mathbf{T} \begin{bmatrix} u_x \\ F_x \end{bmatrix} = \begin{bmatrix} T_{11} & T_{12} \\ T_{21} & T_{22} \end{bmatrix} \begin{bmatrix} u_x \\ F_x \end{bmatrix}, \quad (3.1)$$

in terms of the boundary displacements u_x , u_{x+d} and forces F_x , F_{x+d} , where d is the periodicity. The harmonic displacement field in the elastic medium shown in the figure is defined as

$$u(x,t) = (Ae^{-ikx} + Be^{ikx})e^{i\omega t}, \quad (3.2)$$

where k is the wavenumber and ω is the angular frequency. Similarly, the displacement and force components at the boundaries can be defined as (here, $e^{i\omega t}$ term is omitted for simplicity):

$$\begin{bmatrix} u_{x^+} \\ F_{x^+} \end{bmatrix} = \mathbf{M} \begin{bmatrix} A \\ B \end{bmatrix}, \quad (3.3a)$$

$$\begin{bmatrix} u_{x+d^-} \\ F_{x+d^-} \end{bmatrix} = \mathbf{M}\mathbf{N}|_d \begin{bmatrix} A \\ B \end{bmatrix}, \quad (3.3b)$$

where

$$\mathbf{M} = \begin{bmatrix} 1 & 1 \\ -i\omega Z & i\omega Z \end{bmatrix}, \quad (3.4)$$

while

$$\mathbf{N}|_d = \begin{bmatrix} e^{-ikd} & 0 \\ 0 & e^{ikd} \end{bmatrix}. \quad (3.5)$$

Here, $F = \sigma S$ is used for the elastic medium, where the stress term σ can be expressed as $\sigma(x,t) = C_{11}(\partial u / \partial x)$ (C_{11} is the x -directional component of the stiffness tensor in Voigt notation) and S is the cross-sectional area. The symbol Z denotes the mechanical impedance $\rho c S$ (ρ is the density, c is the phase velocity, and S is the cross-sectional area). In the plane-stress condition, which is applied throughout this work, $C_{11} = E / (1 - \nu^2)$, where E is the Young's modulus and ν is the Poisson's ratio.

Using the continuity condition,

$$\begin{bmatrix} u_{x^-} \\ F_{x^-} \end{bmatrix} = \begin{bmatrix} u_x \\ F_x \end{bmatrix} = \begin{bmatrix} u_{x^+} \\ F_{x^+} \end{bmatrix}, \quad (3.6a)$$

$$\begin{bmatrix} u_{x+d^-} \\ F_{x+d^-} \end{bmatrix} = \begin{bmatrix} u_{x+d} \\ F_{x+d} \end{bmatrix} = \begin{bmatrix} u_{x+d^+} \\ F_{x+d^+} \end{bmatrix}, \quad (3.6b)$$

and combining with Eqs. (3.3a) and (3.3b), the transfer matrix \mathbf{T} can be expressed as

$$\mathbf{T} = \mathbf{M} \mathbf{N}|_d \mathbf{M}^{-1}, \quad (3.7)$$

and thus becomes

$$\mathbf{T} = \begin{bmatrix} \cos(kd) & \frac{1}{\omega Z} \sin(kd) \\ -\omega Z \sin(kd) & \cos(kd) \end{bmatrix}. \quad (3.8)$$

It can be clearly observed that this matrix is composed of the intrinsic terms of the material only, meaning that the boundary terms are dependent only on the embedded material. Therefore, calculating and defining the transfer matrix of various systems is the enabling tool to estimate wave characteristics of the system embedded in arbitrary outer medium.

As for lumped elements, characterization with transfer matrix method is also applicable by structural dynamics. In the next subsections, two major lumped element structures are presented in which all of them contain mass and spring components together. The main reason is to consider the compatibility with continuum versions where both density and stiffness matter simultaneously. Therefore, when modeled by the transfer matrix method, even the continuum material can be defined with respect to the corresponding lumped element model. The following explicit analysis with mass-spring models conceptually explains how the elastic parameters can be controlled by the structural dynamics in time-harmonic wave condition.

3.2.1 Spring-Mass-Spring model (M_{eff} -substructure)

A modified version of the basic dipolar resonator by adding two springs on the both sides are shown in Fig. 3.2(a). This spring-mass-spring model will be denoted as

“ M_{eff} -substructure” for convenience. The reason is that this substructure mainly manipulates the mass term while merely affecting the stiffness term, which will be discussed later. Also, this lumped model will be the basic model to design a continuum M_{eff} -substructure unit cell. In this context, the springs are attached as so in order to not only express a symmetric and reciprocal system but also continuum system which is governed both by the mass and stiffness properties. Corresponding simplified model for transfer matrix definition is drawn in Fig. 3.2(b). Here, as derived in Chapter 2, $M_{eff} = M_m + m_m / (1 - \omega^2 / \omega_r^2)$. Also, it should be noted that although the spring term is denoted as K_{eff} , it does not experience resonance state. Instead, this expression is only to consider the variance of the stiffness component in the continuum version under dynamic motion. Here, it should be noted that because a unit cell is composed of two springs, each spring is considered to have a stiffness of $2K_{eff}$, so that as in the case of a series configuration, they can contribute to the stiffness of K_{eff} in the entire unit cell ($1/K_{eff}^{whole} = (1/2K_{eff} + 1/2K_{eff})$). In this way, for the sake of convenience, a unit cell can be considered to have just M_{eff} and K_{eff} for further calculations related to periodic systems.

Based on the equation of motion and the time-harmonic wave assumption at an angular frequency of ω , the equations of motion are derived as

$$M_{eff} \frac{\partial^2 u_n^M}{\partial t^2} = 2K_{eff} (u_n + u_{n+d}) - 4K_{eff} u_n^M, \quad (3.9a)$$

$$F_n = 2K_{eff} (u_n^M - u_n), \quad (3.9b)$$

$$F_{n+d} = 2K_{eff} (u_{n+d} - u_n^M). \quad (3.9c)$$

Then, by using harmonic assumption $\partial^2 u_n^M / \partial t^2 = -\omega^2 u_n^M$ and substituting Eq. (3.9b) into Eq. (3.9a), we can express u_{n+d} in terms of the quantities (u_n, F_n) in its left-hand side as

$$u_{n+d} = \left(\frac{2K_{eff} - \omega^2 M_{eff}}{2K_{eff}} \right) u_n + \left(\frac{4K_{eff} - \omega^2 M_{eff}}{4K_{eff}^2} \right) F_n. \quad (3.10)$$

Similarly, by substituting Eq. (3.10) into Eq. (3.9c), the right side force F_{n+d} can be expressed as

$$F_{n+d} = (-\omega^2 M_{eff}) u_n + \left(\frac{2K_{eff} - \omega^2 M_{eff}}{2K_{eff}} \right) F_n. \quad (3.11)$$

Thus, the transfer matrix \mathbf{T} becomes

$$\mathbf{T} = \begin{bmatrix} \frac{2K_{eff} - \omega^2 M_{eff}}{2K_{eff}} & \frac{4K_{eff} - \omega^2 M_{eff}}{4K_{eff}^2} \\ -\omega^2 M_{eff} & \frac{2K_{eff} - \omega^2 M_{eff}}{2K_{eff}} \end{bmatrix}. \quad (3.12)$$

3.2.2 Mass-Spring-Mass model (K_{eff} -substructure)

Similar to the former case, the original monopolar resonator with attached masses

on both sides is illustrated in Fig. 3.3(a). This mass-spring-mass model will be denoted as “ K_{eff} -substructure” for convenience. The reason is the same with that of the abovementioned M_{eff} -substructure case. The attached masses are responsible for the density terms in the actual continuum cell. In addition, M_{eff} is equally divided for a symmetric and reciprocal assumption. Most importantly, similar to the M_{eff} -substructure case, M_{eff} does not experience resonance state because a dipolar resonator cannot be divided into two pieces.

The equation of motion can be written as

$$K_{eff}(u_{n+d} - u_n) - F_n = \frac{M_{eff}}{2} \frac{\partial^2 u_n}{\partial t^2}, \quad (3.13a)$$

$$F_{n+d} + K_{eff}(u_n - u_{n+d}) = \frac{M_{eff}}{2} \frac{\partial^2 u_{n+d}}{\partial t^2}. \quad (3.13b)$$

Re-writing Eq. (3.13a) with respect to u_{n+d} becomes

$$u_{n+d} = \left(\frac{2K_{eff} - \omega^2 M_{eff}}{2K_{eff}} \right) u_n + \frac{1}{K_{eff}} F_n. \quad (3.14)$$

Substituting Eq. (3.14) into Eq. (3.13b) yields

$$F_{n+d} = -\omega^2 M_{eff} \left(1 - \frac{\omega^2 M_{eff}}{4K_{eff}} \right) u_n + \left(\frac{2K_{eff} - \omega^2 M_{eff}}{2K_{eff}} \right) F_n. \quad (3.15)$$

Consequently, the transfer matrix for the K_{eff} -substructure can be obtained as

$$\mathbf{T} = \begin{bmatrix} \frac{2K_{eff} - \omega^2 M_{eff}}{2K_{eff}} & \frac{1}{K_{eff}} \\ -\omega^2 M_{eff} \left(1 - \frac{\omega^2 M_{eff}}{4K_{eff}}\right) & \frac{2K_{eff} - \omega^2 M_{eff}}{2K_{eff}} \end{bmatrix}. \quad (3.16)$$

3.3 Transfer Matrix Method Employed in Theoretical Domain

Transfer matrix evaluation can be significantly useful to predict various wave characteristics. As mentioned above, a material's transfer matrix contains its own intrinsic physical features. Therefore, the transfer matrix itself well represents the material's properties in the wave aspect. Also, when combined with other environments (e.g., embedded in dissimilar medium, free-end reflection condition, attached on hard boundary, etc.), transfer matrix can be conveniently implemented to investigate the wave physics by considering boundary conditions.

In this chapter, crucial methods to derive the essential wave characteristics using transfer matrixes will be presented.

3.3.1 Dispersion curve evaluation

As discussed in Chapter 2, the dispersion curve is the basic plot for a material's wave behavior. By the Bloch-Floquet theorem, the properties of the boundaries are also governed by periodicity such that

$$\begin{bmatrix} u_{x+d} \\ F_{x+d} \end{bmatrix} = \lambda \begin{bmatrix} u_x \\ F_x \end{bmatrix} = e^{iqd} \begin{bmatrix} u_x \\ F_x \end{bmatrix}, \quad (3.17)$$

where λ denotes eigenvalues of the periodic equation. By substituting Eq. (3.1) into Eq. (3.17), the nontrivial solution can be obtained from

$$\det(\mathbf{T} - \lambda \mathbf{I}) = 0, \quad (3.18)$$

so that

$$\lambda^2 - (\text{tr}\mathbf{T})\lambda + \det(\mathbf{T}) = 0. \quad (3.19)$$

Here, because the system is energy conservative, employing $\det(\mathbf{T})=1$ and solving Eq. (3.19) yields

$$\lambda = e^{iqd} = \frac{\text{tr}\mathbf{T}}{2} \pm i \sqrt{1 - \left(\frac{\text{tr}\mathbf{T}}{2}\right)^2}. \quad (3.20)$$

Finally, only considering the real parts, the dispersion relation regarding the transfer matrix can be expressed as

$$\cos(qd) = \frac{\text{tr}\mathbf{T}}{2} = \frac{T_{11} + T_{22}}{2}. \quad (3.21)$$

If the system is reciprocal as those mentioned above, $T_{11} = T_{22}$ and Eq. (3.21) can be simplified to

$$\cos(qd) = T_{11}. \quad (3.22)$$

As shown in Fig. 3.4(a), M_{eff} -substructure and K_{eff} -substructure models are equivalent in infinite series. Therefore, they both have the same dispersion relation (they have the same T_{11} and T_{22} components)

$$\cos(qd) = \frac{2K_{eff} - \omega^2 M_{eff}}{2K_{eff}}, \quad (3.23)$$

which is the same as (only without the dynamically effective properties) that of simple mass-spring lattice in Eq. (2.6).

3.3.2 Characteristic impedance evaluation

Characteristic impedance is a fundamental property of a material that defines its resistance subject to outer force. Specifically, mechanical impedance is defined as the ratio of force exerted to velocity. In this subsection, characteristic impedances of M_{eff} -substructure and K_{eff} -substructure models will be analytically formulated. Then, the general impedance retrieval equation will be deduced using the transfer matrix components.

Impedance for M_{eff} -substructure model

Fig. 3.4(b) shows the schematic drawing to calculate the characteristic impedance Z_M for the M_{eff} -substructure model. The impedance term is defined by

$$Z_M \dot{u}_n = f_{n,n-d}, \quad (3.24)$$

where $f_{n,n-d}$ is the force exerted by the mass in $(n-d)^{th}$ cell to boundary n , so that

$$f_{n,n-d} = 2K_{eff} (u_{n-d}^M - u_n), \quad (3.25)$$

and \dot{u}_n the velocity of n^{th} boundary. Substituting the basic governing Eq. (3.9a)

and the Bloch periodicity condition $u_{n-d} = e^{-iqd} u_n$ into Eq. (3.25) and Eq. (3.24) yields

$$-i\omega Z_M = \frac{2K_{eff} \left[2K_{eff} (e^{-iqd} - 1) + \omega^2 M_{eff} \right]}{4K_{eff} - \omega^2 M_{eff}}. \quad (3.26)$$

Modifying e^{-iqd} to $\cos(qd) - i \sin(qd)$ yields

$$Z_M = \frac{4K_{eff}^2 \sin(qd)}{\omega(4K_{eff} - \omega^2 M_{eff})}. \quad (3.27)$$

Finally, the mechanical impedance becomes

$$Z_M = \frac{\sqrt{M_{eff} K_{eff}}}{\cos\left(\frac{qd}{2}\right)}. \quad (3.28)$$

Note that the impedance term is purely real and does not contain any imaginary value.

Impedance for K_{eff} -substructure model

Similar to the former procedure, Fig. 3.4(c) will be utilized to calculate the impedance Z_K for the K_{eff} -substructure model. In this case, the governing equation regarding the impedance term is as below:

$$Z_K \dot{u}_n = f_{n,n-d} + \frac{1}{2} M_{eff} \ddot{u}_n, \quad (3.29)$$

where $f_{n,n-d}$ is the force exerted by the boundary $n-d$ to boundary n , so that

$$f_{n,n-d} = K_{eff} (u_{n-d} - u_n). \quad (3.30)$$

Similar to the former procedure, Eq. (3.29) can be solved as

$$-i\omega Z_K = K_{eff} (e^{-iqd} - 1) + \frac{1}{2} \omega^2 M_{eff}, \quad (3.31)$$

so that

$$Z_K = \frac{K_{eff}}{\omega} \sin(qd), \quad (3.32)$$

and the mechanical impedance for the K_{eff} -substructure model finally becomes

$$Z_K = \sqrt{M_{eff} K_{eff}} \cos\left(\frac{qd}{2}\right). \quad (3.33)$$

This impedance is also purely real just like the former one.

General Impedance Definition with Transfer Matrix Components

Now let us derive the general impedance definition for arbitrary material with known transfer matrix components. The conceptual configuration is presented in Fig. 3.4(d). With this method, “effective impedance” can be defined for any material that can be characterized by a transfer matrix. As shown in the figure, the impedance will be determined by the boundary terms. From the transfer matrix definition in Eq. (3.1) of which

$$u_{n+d} = T_{11}u_n + T_{12}F_n, \quad (3.34)$$

the system impedance term Z_S can be induced such as

$$e^{iqd} = T_{11} + i\omega T_{12}Z_S, \quad (3.35)$$

so that,

$$i\omega T_{12}Z_S = \cos(qd) + i\sin(qd) - T_{11}. \quad (3.36)$$

Finally, the real and imaginary parts of the system impedance can be represented as

$$Z_r = \frac{\sin(qd)}{\omega T_{12}}, \quad (3.37a)$$

$$Z_i = \frac{(T_{11} - \cos(qd))}{\omega T_{12}}. \quad (3.37b)$$

Here, it must be noted that in symmetric (reciprocal) systems where $T_{11} = T_{22}$, the numerator of Eq. (3.37b) becomes 0 (thus, $Z_i = 0$), making the system impedance purely real like the former examples. However, it must be noted that the real part “can” also be imaginary due to the anomalous effective properties. In other words, the system impedance has purely real part for normal materials, but is allowed to possess also imaginary terms if the properties are single-negative for metamaterials. This general (“effective”) impedance definition has much potential to be applied especially for various lumped element systems where transfer matrix components can be explicitly determined. Detailed studies will be further presented in section 3.4.

3.3.3 Transmission spectra of multiple lumped-element structures embedded within continuum media

Calculation of wave transmission in dissimilar media or layered multiple structures is crucial for system analysis and design. Although there have been clear

investigations for transmission properties in continuum media, no analysis for lumped elements embedded within continuum media has been performed. As mentioned before, the metamaterials with effective properties are well interpreted with lumped models and they are installed within continuum structures for practical use. Therefore, a unique analysis to derive transmission spectra for lumped elements interacting with continuum media will be presented in this subsection.

Simplified N^{th} power transfer matrix for multiple unit cells

Fig. 3.5 shows an illustration to investigate the physics of multiple unit cells embedded in a continuum elastic medium. Here, the drawing is from the example of M_{eff} -substructure. However, it should be noted that the following analysis applies to all types of symmetric (reciprocal) cells, even continuum cells. First of all, because multiple N number of unit cells can be considered, N^{th} power transfer matrix definition is required. For N unit cells, the components of the transfer matrix are denoted as

$$\begin{bmatrix} u_{n+Nd} \\ F_{n+Nd} \end{bmatrix} = \mathbf{T}^N \begin{bmatrix} u_n \\ F_n \end{bmatrix} = \begin{bmatrix} T_{11}^N & T_{12}^N \\ T_{21}^N & T_{22}^N \end{bmatrix} \begin{bmatrix} u_n \\ F_n \end{bmatrix}. \quad (3.38)$$

Since the system is linear and reciprocal, the transfer matrix is unimodular, which means that $\det(\mathbf{T})=0$. In this special case, the N^{th} power of a unimodular matrix is given by (Appendix A) [70, 71]

$$\mathbf{T}^N = \begin{bmatrix} T_{11}U_{N-1}(a) - U_{N-2}(a) & T_{12}U_{N-1}(a) \\ T_{21}U_{N-1}(a) & T_{22}U_{N-1}(a) - U_{N-2}(a) \end{bmatrix}, \quad (3.39)$$

where

$$a = \frac{1}{2}(T_{11} + T_{22}), \quad (3.40a)$$

$$U_N(a) = \frac{\sin[(N+1)\cos^{-1}a]}{\sqrt{1-a^2}}. \quad (3.40b)$$

In the present periodic mass-spring system (including both the M_{eff} -substructure and K_{eff} -substructure models), Eqs. (3.40a) and (3.40b) become

$$a = \cos(qd), \quad (3.41a)$$

$$U_N(a) = \frac{\sin[(N+1)qd]}{\sin(qd)}. \quad (3.41b)$$

Substituting Eqs. (3.41a) and (3.41b) into Eq. (3.39) yields the simplified N^{th} power transfer matrix as

$$\mathbf{T}^N = \begin{bmatrix} \cos(Nqd) & T_{12} \frac{\sin(Nqd)}{\sin(qd)} \\ T_{21} \frac{\sin(Nqd)}{\sin(qd)} & \cos(Nqd) \end{bmatrix}. \quad (3.42)$$

Transmitted elastic wave characterization

On the other hand, the harmonic displacement field in the outer elastic medium shown in Fig. 3.5 is defined as

$$u(x,t) = (A_1 e^{-ikx} + B_1 e^{ikx}) e^{i\omega t}, \quad (x \leq 0) \quad (3.43a)$$

$$u(x,t) = (A_2 e^{-ik(x-Nd)} + B_2 e^{ik(x-Nd)}) e^{i\omega t}, \quad (x \geq Nd) \quad (3.43b)$$

Similarly, the displacement and force components can be defined as (here, $e^{i\omega t}$ term is omitted for simplicity):

$$\begin{bmatrix} u(x,t) \\ F(x,t) \end{bmatrix} = \mathbf{M} \begin{bmatrix} A_1 e^{-ikx} \\ B_1 e^{ikx} \end{bmatrix}, \quad (x \leq 0) \quad (3.44a)$$

$$\begin{bmatrix} u(x,t) \\ F(x,t) \end{bmatrix} = \mathbf{M} \begin{bmatrix} A_2 e^{-ik(x-Nd)} \\ B_2 e^{ik(x-Nd)} \end{bmatrix}, \quad (x \geq Nd) \quad (3.44b)$$

where \mathbf{M} is as defined in Eq. (3.4). At the input and output boundaries, as shown in the figure, the continuous condition for the displacements and forces can be expressed as

$$\begin{bmatrix} u(x,t) \\ F(x,t) \end{bmatrix}_{x=0^+} = \begin{bmatrix} u(x,t) \\ F(x,t) \end{bmatrix}_{x=0^-} = \mathbf{M} \begin{bmatrix} A_1 \\ B_1 \end{bmatrix}, \quad (3.45a)$$

$$\begin{bmatrix} u(x,t) \\ F(x,t) \end{bmatrix}_{x=Nd^-} = \begin{bmatrix} u(x,t) \\ F(x,t) \end{bmatrix}_{x=Nd^+} = \mathbf{M} \begin{bmatrix} A_2 \\ B_2 \end{bmatrix}. \quad (3.45b)$$

Combining this with the transfer matrix as

$$\begin{bmatrix} u(x,t) \\ F(x,t) \end{bmatrix}_{x=Nd^-} = \mathbf{T}^N \begin{bmatrix} u(x,t) \\ F(x,t) \end{bmatrix}_{x=0^+}, \quad (3.46)$$

we get

$$\begin{bmatrix} A_2 \\ B_2 \end{bmatrix} = \mathbf{M}^{-1} \mathbf{T}^N \mathbf{M} \begin{bmatrix} A_1 \\ B_1 \end{bmatrix} = \mathbf{S} \begin{bmatrix} A_1 \\ B_1 \end{bmatrix}, \quad (3.47)$$

where \mathbf{S} is the scattering matrix of N metamaterial unit cells. The components of \mathbf{S} become

$$S_{11} = \frac{1}{2} \left[(T_{11}^N + T_{22}^N) - i \left(\omega Z T_{12}^N - \frac{1}{\omega Z} T_{21}^N \right) \right], \quad (3.48a)$$

$$S_{12} = \frac{1}{2} \left[(T_{11}^N - T_{22}^N) + i \left(\omega Z T_{12}^N + \frac{1}{\omega Z} T_{21}^N \right) \right], \quad (3.48b)$$

$$S_{21} = \frac{1}{2} \left[(T_{11}^N - T_{22}^N) - i \left(\omega Z T_{12}^N + \frac{1}{\omega Z} T_{21}^N \right) \right], \quad (3.48c)$$

$$S_{22} = \frac{1}{2} \left[(T_{11}^N + T_{22}^N) + i \left(\omega Z T_{12}^N - \frac{1}{\omega Z} T_{21}^N \right) \right], \quad (3.48d)$$

Assuming no reflection from the right side, B_2 becomes 0 (therefore, $S_{21}A_1 + S_{22}B_1 = 0$), and hence we can derive the transmission coefficient T as

$$T = \frac{A_2}{A_1} = S_{11} - \frac{S_{12}S_{21}}{S_{22}}. \quad (3.49)$$

Since input and output materials are the same, $\det(\mathbf{S})=1$ and Eq. (3.49) becomes

$T = 1/S_{22}$ and thus

$$T = \frac{2}{(T_{11}^N + T_{22}^N) + i \left(\omega Z T_{12}^N - \frac{1}{\omega Z} T_{21}^N \right)}. \quad (3.50)$$

Substituting the simplified N^{th} power transfer matrix Eq. (3.42) into Eq. (3.50) yields

$$T = \frac{2}{2 \cos(Nqd) + i \left(\omega Z T_{12} - \frac{1}{\omega Z} T_{21} \right) \sin(Nqd) / \sin(qd)}. \quad (3.51)$$

In order to efficiently explore the transmitted wave characteristics based on the effective properties, we simplify Eq. (3.51) by adopting the aforementioned

effective impedance definition. Substituting Eq. (3.37a) into Eq. (3.51), we can re-write T as

$$T = \frac{2}{2 \cos(Nqd) + i \left(\frac{Z}{Z_s} + \frac{Z_s}{Z} \right) \sin(Nqd)}, \quad (3.52)$$

which is similar to that of the continuum version [36, 69]. Specifically, if series of M_{eff} -substructure (K_{eff} -substructure) model is embedded, Eq. (3.28) (Eq. (3.33)) should be implemented as system impedance Z_s .

3.4 Transfer Matrix Method Employed in Numerical Simulation Domain with Actual Continuum Structures

In the former section, fundamental studies on implementing transfer matrix method to theoretically evaluate wave characteristics were carried out. In this section, validation of such studies will be given to retrieve the wave characteristics. As mentioned above, the biggest advantage of utilizing the transfer matrix is that it considers only the unit cell's boundary terms (u, F). In other words, the transfer matrix components are closely related to the boundary terms and even can be expressed by them under following conditions. Throughout this work, we consider only lossless materials (energy conservative) so that $\det(\mathbf{T})=0$. Also, we consider symmetric (reciprocal) materials and lumped elements so that $T_{11}=T_{22}$. Under these two conditions, the transfer matrix in Eq. (3.1) can be re-written with respect

to the boundary terms as

$$T_{11} = \frac{F|_{x=d} u|_{x=d} + F|_{x=0} u|_{x=0}}{F|_{x=0} u|_{x=d} + F|_{x=d} u|_{x=0}}, \quad (3.53a)$$

$$T_{12} = \frac{(u|_{x=d})^2 - (u|_{x=0})^2}{F|_{x=0} u|_{x=d} + F|_{x=d} u|_{x=0}}, \quad (3.53b)$$

$$T_{21} = \frac{(F|_{x=d})^2 - (F|_{x=0})^2}{F|_{x=0} u|_{x=d} + F|_{x=d} u|_{x=0}}, \quad (3.53c)$$

$$T_{22} = \frac{F|_{x=d} u|_{x=d} + F|_{x=0} u|_{x=0}}{F|_{x=0} u|_{x=d} + F|_{x=d} u|_{x=0}}. \quad (3.53d)$$

The conceptual drawing for numerical (also experimentally valid) domain is shown in Fig. 3.6. One of its advantages is that such method is feasible both for simulation and experiment. Conventionally in experiments, especially in the acoustic regime, the well-known 4-point-method has been generally utilized [69]. However, it requires some suitable space to measure the fields. Also, to exactly measure the transmission coefficient, non-reflecting boundary conditions were necessary. It should be noted that in contrast to this method, the transfer matrix method does not require any non-reflecting boundaries (in simulation, also known as perfectly matched layers) which is not practical to realize. As proved in Eq. (3.50), the original components can be analytically substituted to calculate transmission coefficients for the main cell embedded in any arbitrary outer media.

Mainly, in this chapter, we will verify the validity of the transfer matrix method by actually adapting it to the continuum forms of M_{eff} -substructure and K_{eff} -

substructure models. With the theoretical evaluation in the previous section, we will calculate the characteristic impedance, dispersion curve, and transmission coefficients for both substructures. Then, the effective parameters retrieval, which is the most fascinating functionality of this method, will be introduced.

First, the continuum versions of cells will be briefly introduced. In Fig. 3.7(a), the continuum M_{eff} -substructure and its geometrical features are given. The continuum version is designed to behave like the lumped model which is depicted on the upper side. It has the main outer thick boundaries which play the role of both the main mass and symmetric outer springs. Inside the cell, a uniquely designed structure with slits are attached which acts as the local resonator. Specifically, the slits near the both end sides drastically weakens the stiffness in the x -direction, which is responsible in controlling the resonance frequency. In other words, these geometrical feature plays the role of the resonator spring term k_m .

To investigate the physics behind this cell, the mode shape near the resonance frequency is shown in Fig. 3.7(b). Here, the color plot represents the x -directional displacement fields. Also, the black cones visualizes the direction and magnitudes of the displacement fields. As initially intended when designing the system, the whole cell displays the dipolar resonance. By the dynamic vibration of this local resonator near the resonance frequency, the outer boundaries of the whole cell experiences negative (positive) values of inertia, thus exhibiting negative (extreme) values of mass terms.

On the other hand, the continuum version of the K_{eff} -substructure is depicted in Fig.

3.8(a). Here, the inclined red beam in the lumped element model (upper side) is similarly realized in the continuum cell with slope of $\theta = \tan^{-1}(1/3)$. The inner resonators are connected to the outer boundaries with the inclined beams. When the resonators vibrate in the y -direction near the resonance frequency as shown in Fig. 3.8(b), the inclined beams transfer such motion into x -directional forces so that the monopolar resonance can be successfully realized. The outer firm boundaries are intended to behave as the both-sided masses.

As such, the continuum versions of each cell have been uniquely designed to induce dipolar and monopolar resonance, respectively. In the next subsections, we will confirm the validity of these substructures by checking the dispersion relation, characteristic impedance, transmission spectra along with effective mass and stiffness properties that will all be retrieved by our own transfer matrix method.

In addition, although the higher modes of the elastic metamaterials can induce new mechanisms (by torsional and bending modes, etc.), we will only consider the specific frequency ranges of basic dipolar and monopolar resonances throughout the work. The main reason is that such resonances are the key factors for manipulating the very basic elastic constitutive properties. Also, the mass-spring model should possess simplicity as to intuitively design and analyze the continuum elastic metamaterial cell based on themselves.

Also, it should be noted that the following continuum modellings are not the only solutions. At the target frequencies, various cells can be proposed to satisfy the desired properties.

3.4.1 Dispersion curve, characteristic impedance, and transmission coefficient retrieval

The retrieval method in this subsection is based on the transfer matrix mentioned in section 3.3. The only difference is that the transfer matrix components can be numerically calculated by simulations with actual cells. Therefore, it would be worthwhile to re-write the theoretical equations by substituting numerical components here. As for the dispersion curve, Eq. (3.21) for symmetric systems can be modified as

$$\cos(qd) = \frac{\text{tr}\mathbf{T}}{2} = \frac{T_{11} + T_{22}}{2} = \frac{F|_{x=d} u|_{x=d} + F|_{x=0} u|_{x=0}}{F|_{x=0} u|_{x=d} + F|_{x=d} u|_{x=0}}, \quad (3.54)$$

so that

$$qd = \cos^{-1} \left(\frac{F|_{x=d} u|_{x=d} + F|_{x=0} u|_{x=0}}{F|_{x=0} u|_{x=d} + F|_{x=d} u|_{x=0}} \right). \quad (3.55)$$

In this way, the dispersion relation of any material embedded in arbitrary medium (as in Fig. 3.6) can be numerically evaluated. As for the impedance term, Eq. (3.37) can be modified as

$$Z_s = \frac{\sin(qd)}{\omega T_{12}} = \frac{\sin(qd)}{\omega} \left(\frac{F|_{x=0} u|_{x=d} + F|_{x=d} u|_{x=0}}{(u|_{x=d})^2 - (u|_{x=0})^2} \right), \quad (3.56)$$

where the Bloch wavenumber term must initially be derived from Eq. (3.55) and then substituted here. Similarly, the transmission coefficient in Eq. (3.50) can be

modified as

$$\begin{aligned}
T &= \frac{2}{(T_{11} + T_{22}) + i\left(\omega Z T_{12} - \frac{1}{\omega Z} T_{21}\right)} \\
&= \frac{2(F|_{x=0} u|_{x=d} + F|_{x=d} u|_{x=0})}{2(F|_{x=d} u|_{x=d} + F|_{x=0} u|_{x=0}) + i\left(\omega Z \left[(u|_{x=d})^2 - (u|_{x=0})^2\right] - \frac{1}{\omega Z} \left[(F|_{x=d})^2 - (F|_{x=0})^2\right]\right)}
\end{aligned} \tag{3.57}$$

The above three major equations are crucial in investigating the wave characteristics of any arbitrary material by just “boundary responses”. To demonstrate this method for actual metamaterials, we employ the aforementioned two cells by setting the simulation as shown in Fig. 3.6. We impose periodic boundary conditions at the upper and lower boundaries for plane wave assumption. The harmonic x -directional force (for longitudinal wave generation) is exerted at the left side within the outer medium. Although PMLs are not required theoretically, we impose them for clearer results. For practical feasibility, the cells are materialized by aluminum plate with thickness of 0.5 mm. The outer medium is also set to be an aluminum plate with the same thickness for simplicity.

Wave characteristics of the M_{eff} -substructure (dipolar cell)

The three major wave characteristics of the M_{eff} -substructure is shown in Fig. 3.9(a). The resonance frequency is set to be slightly above 100 kHz for convenience. As a result, the resonance gap opens up just above 100 kHz which is shown in the dispersion curve retrieved by Eq. (3.55). The corresponding relative impedance

(Z_M/Z) is also displayed below. The impedance definition of the M_{eff} -substructure is written inside the graph for assistance. According to the definition, the relative impedance exceedingly increases below the resonance frequency so that the impedance matching condition can be satisfied. Actually, the relative impedance starts from less than 1 value at static regime (0 kHz) because the cell has lowered value of impedance due to perforated regions. As the frequency increases, the relative impedance increases owing to the resonance effect. This is because the M_{eff} term is increased due to the dipolar resonance to compensate for the decreased impedance. In another point of view, the impedance matching condition is from the $\cos(qd/2)$ term that converges to 0 value just below the resonance gap so that Z_M remarkably increases to compensate the lowered impedance. The underlying physics behind these explanations will be specifically dealt with in the next subsection. Consequently, the transmission spectra shows total transmission phenomenon at the impedance matched frequency. It should be noted that this condition occurs just below the resonance gap. Above that, the transmission is severely dropped owing to the resonance gap.

Wave characteristics of the K_{eff} -substructure (monopolar cell)

The same procedures have been performed with the K_{eff} -substructure and the results are shown in Fig. 3.10(a). Similar to the former case, the resonance gap around the resonance frequency can be observed from the dispersion curve. In contrast to the

dipolar case, the relative impedance curve exhibits a totally different aspect. The impedance matching condition is fulfilled above the resonance gap whereas it was achieved below the gap in the M_{eff} -substructure case. The originally lowered impedance of the K_{eff} -substructure is compensated “above” the resonance frequency. In other words, the impedance matching condition for the M_{eff} -substructure occurs at the upper end of the lower passband whereas for the K_{eff} -substructure, it happens at the lower end of the upper passband. Also, the effect of the $\cos(qd/2)$ term is insignificant in this case. Therefore, this cell is mainly dominated by the effective properties M_{eff} and K_{eff} , which will be thoroughly discussed in the next subsection. Consequently, the transmission curve decreases near the resonance gap and then fulfills the total transmission condition as the frequency increases.

3.4.2 Effective parameter retrieval

To begin with, the concept of effective parameter retrieval method will be explained. Similar to the S-parameter method [67, 68], the effective properties can be calculated by considering boundary responses when exerted by external harmonic wave forces. The only difference is that in the S-parameter method, the incident, reflected, and the transmitted wave fields are employed whereas in transfer matrix method, all the terms are compiled in the boundary terms. The various terms are actually theoretically compatible with each other. The basic principle of the S-parameter method can be explained from the transfer matrix perspective by utilizing Eq. (3.1) and Eq. (3.8) so that

$$\rho_{eff} = \frac{kZ}{\omega S} = \frac{\cos^{-1}(T_{11}) \sin(\cos^{-1}(T_{11}))}{Sd\omega^2 T_{12}}, \quad (3.58a)$$

$$E_{eff} = \frac{\omega Z}{kS} = \frac{\sin(\cos^{-1}(T_{11}))d}{T_{12} \cos^{-1}(T_{11})}. \quad (3.58b)$$

where S is the cross-sectional area. Here, numerically derived (or experimentally obtained) transfer matrix components are required to calculate the effective mass density and Young's modulus properties. Based on the similar procedures, the effective properties of the lumped element models will be derived.

Effective parameter retrieval for the M_{eff} -substructure (dipolar cell)

With Eq. (3.1) and Eq. (3.12), the effective parameters for the M_{eff} -substructure (dipolar cell) can be retrieved as

$$M_{eff} = -\frac{T_{21}}{\omega^2}, \quad (3.59a)$$

$$K_{eff} = \frac{T_{21}}{2(T_{11} - 1)}. \quad (3.59b)$$

Because the components of the transfer matrix are frequency dependent, the corresponding effective parameters are exclusively obtained at every frequency. The semi-analytical results from the actual cell in Fig. 3.7(a) are shown in Fig. 3.9(b). As intended and expected when designing the cell, only the M_{eff} term undergoes resonant state whereas K_{eff} remains almost constant. In particular, as frequency increases, M_{eff} first drastically exceeds to the positive infinite value

and then after the resonance frequency, it starts from the negative infinite value and eventually recovers to the positive value. Therefore, for the impedance increasing phenomenon just below the resonance frequency, it can be concluded that both the amplified M_{eff} value and the effect of lowered $\cos(qd/2)$ terms are mainly responsible. In other words, the M_{eff} -substructure is capable of compensating the impedance for total transmission just below its resonance frequency.

Effective parameter retrieval for the K_{eff} -substructure (monopolar cell)

With Eq. (3.1) and Eq. (3.16) the effective parameters of the K_{eff} -substructure (monopolar cell) can be deduced as

$$M_{eff} = -\frac{2(T_{11} - 1)}{\omega^2 T_{12}}, \quad (3.60a)$$

$$K_{eff} = \frac{1}{T_{12}}. \quad (3.60b)$$

The results from the actual monopolar cell (Fig. 3.8(a)) is shown in Fig. 3.10(b). In contrast to the M_{eff} -substructure, only the K_{eff} term experiences resonance state whereas M_{eff} remains rather constant as intended. Also, as analytically calculated in Chapter 2, K_{eff} first goes to negative infinity first and then starts from positive infinity after the resonance frequency. In other words, the resonance phenomena of K_{eff} and M_{eff} have somewhat opposite aspects. Most importantly, it can be inferred from the impedance term that the amplified K_{eff} is the one that is mainly

responsible for impedance compensation. Therefore, total transmission occurs at the beginning of the higher branch where K_{eff} is extremely amplified.

Remarks on effective parameter retrieval procedure with transfer matrix method

Compared to the analytic method with static estimation by Oh *et al.* [38], our method is capable of computing the actual ‘dynamic’ values of the effective properties that absolutely correlate with the transmission, dispersion curve, and the impedance values. Even more, compared to the S-parameter retrieval method [67] which is only feasible with homogenized continuum materials as in Eq. (3.58), our method is optimal to retrieve the proper values for metamaterials containing local resonators. In other words, the conventional method could not retrieve meaningful values for metamaterials especially near the resonance where dynamic fluctuations take place.

For example, the effective properties of the two cells have been retrieved with the S-parameter method (Eqs. (3.58a-b)) and the results are shown in Fig. 3.11. In other words, the metamaterial cells were assumed to behave as a homogenized material with anomalous properties as depicted inside the graphs. In contrast to the appropriate values that had been discussed above, both ρ_{eff} and E_{eff} are shown to experience resonance phenomena for both the dipolar case (Fig. 3.10(a)) and monopolar case (Fig. 3.10(b)).

It can be confirmed that wrong assumption of the cell provides meaningless values

of properties. In other words, the conventional S-parameter retrieval method is not suitable for estimating the properties of metamaterials with resonant characteristics. The S-parameter retrieval method has been limited to estimate the effective property values by considering it as a fully homogenized material. Yet, the local dynamics within the metamaterials cannot be completely expressed with homogenized material assumptions. However, our method fully describes the geometrical features of the metamaterial cell by the lumped element model and thus enables retrieval of the correct values.

In a similar context, the lumped element model must also be chosen carefully regarding the eigen mode shape of the continuum cell. For example, the properties of the M_{eff} -substructure (dipolar continuum cell) is retrieved by the K_{eff} -substructure model (monopolar lumped element model) as shown in Fig. 3.12(a). Similar to the former inappropriate assumption, the properties are somewhat coupled near the resonance frequency. The main reason is that the monopolar model cannot characterize the dipolar mode shape into valid properties. The inertia term is managed by both the spring and mass term, thus inducing unwanted resonance state of effective stiffness values. Although one may question that this could indicate a meaningful value, the different aspect of the K_{eff} -curve from the theoretical analysis (Fig. 2.8(b)) proves it wrong. Such invalid values have occurred to just satisfy the boundary responses of the M_{eff} -substructure.

On the other hand, the retrieved values of the K_{eff} -substructure (monopolar cell) by assuming it as a M_{eff} -substructure model (dipolar lumped element model) are

shown in Fig. 3.12(b). Alike the former case, the properties seem correlated such that both of them undergo resonance states in a similar manner. Here, unwanted properties of M_{eff} have occurred because the monopolar mode shape is forcefully expressed by the inertia term of the rigid mass outer mass. One should be aware that this is an invalid value because the aspect of the M_{eff} -curve does not follow the theoretically evaluated form as derived in Fig. 2.8(a).

As such, choosing the proper basic unit cell does matter in characterizing a target material although they make up the same system (mass-spring lattice) in infinite series. As discussed in Chapter 2, each model has totally different physics behind them, which goes the same for the continuum cells. Consequently, it should be noted that a proper model must be considered to retrieve the meaningful effective properties from the target cell. In other words, contrary to the wave characteristics (dispersion relation, impedance, and transmission), effective parameter retrieval can be subjective and it depends on proper choice from various models of which the cell is assumed to be.

3.5 Summary

A concrete method based on the transfer matrix is proposed in this chapter to exclusively evaluate the wave characteristics. The major breakthrough was to correct the conventional homogenized models that were insufficient to estimate the properties especially for the metamaterials containing local resonators, even under

the long-wavelength assumption. The main reason is that the local dynamics cannot be precisely expressed with the terms belonging to the homogenized materials. In order to overcome the limitations, we have devised explicit lumped element models and their transfer matrixes to accurately define and evaluate the wave features of metamaterials. From the actual boundary responses in harmonic condition for every frequency, the three major (dispersion relation, characteristic impedance, and transmission coefficient) characteristics that define the unit cell have been successfully estimated.

The essential contribution of this chapter is our unique way of retrieving the effective mass and stiffness properties by assuming the continuum cell to behave as a lumped mass-spring model. In contrast to conventional methods, exact and meaningful properties can be retrieved, which also explain the underlying physics very reasonably. Most of all, the effective properties that were derived from our methods are completely compatible with the wave characteristics in all frequency ranges. Finally, it should also be noted that the wave characteristics and the effective properties are all based on the explicitly devised transfer matrix method for lumped element models, which provides the unity in various analyses.

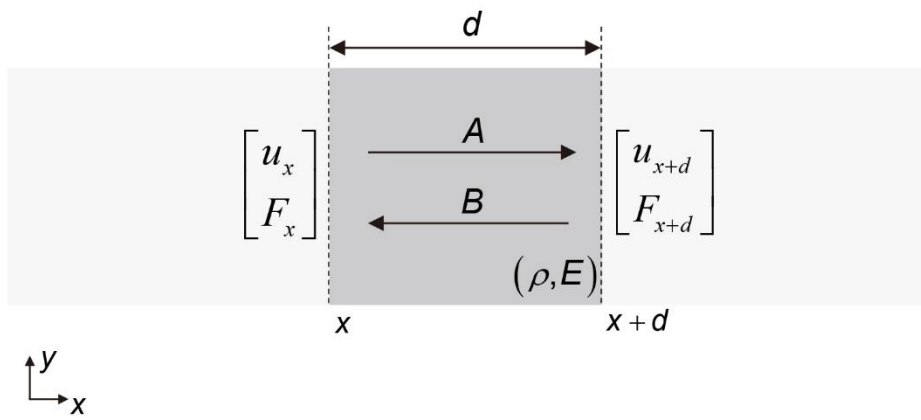


Fig. 3.1 Schematic drawing for the transfer matrix calculation.

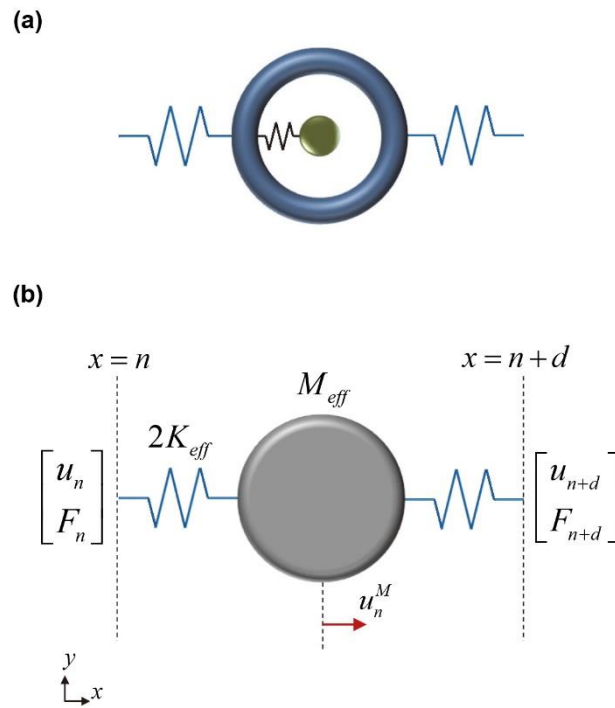


Fig. 3.2 (a) Dipolar resonator with springs attached on both sides to represent the continuum unit cell which contains both density and stiffness components. (b) Simplified model for the transfer matrix definition.

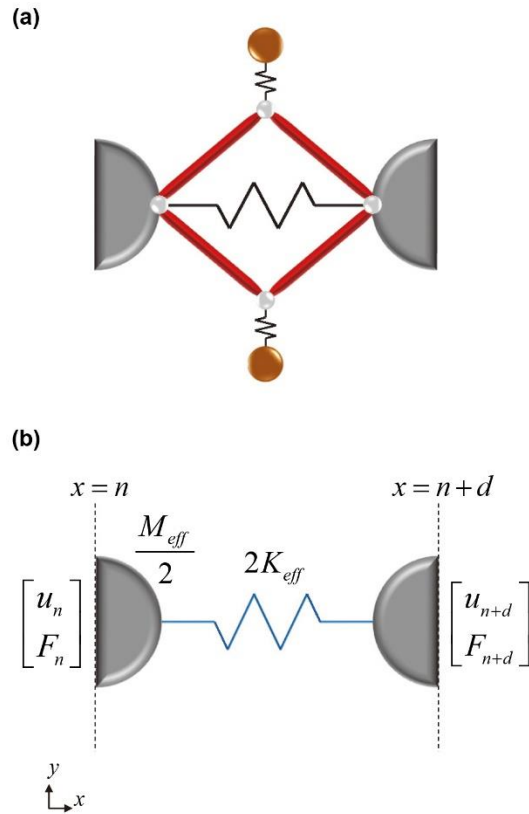


Fig. 3.3 (a) Monopolar resonator with rigid masses attached on both sides to represent the continuum unit cell which contains both density and stiffness components. (b) Simplified model for the transfer matrix definition.

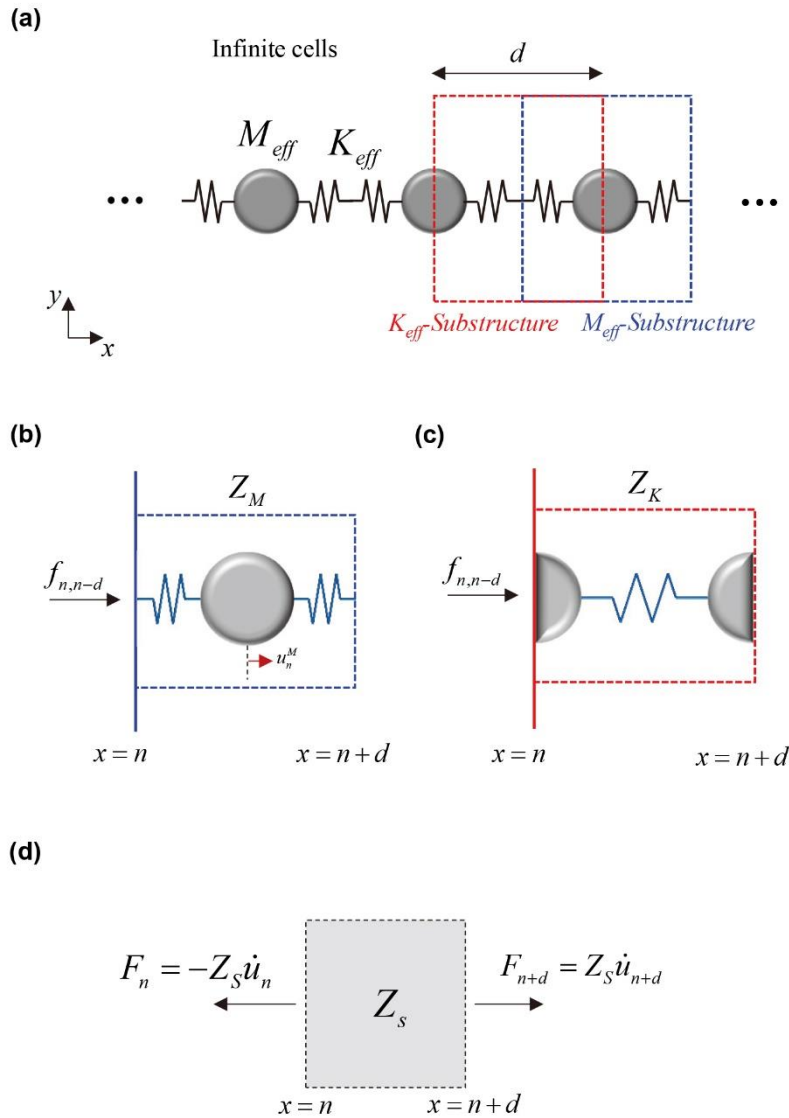


Fig. 3.4 (a) Infinite series of mass-spring containing effective properties. (b) Schematic drawing to calculate the mechanical impedance of the M_{eff} substructure. (c) Schematic drawing to calculate the mechanical impedance of the K_{eff} substructure. (d) Schematic drawing to retrieve effective impedance term from an arbitrary material.

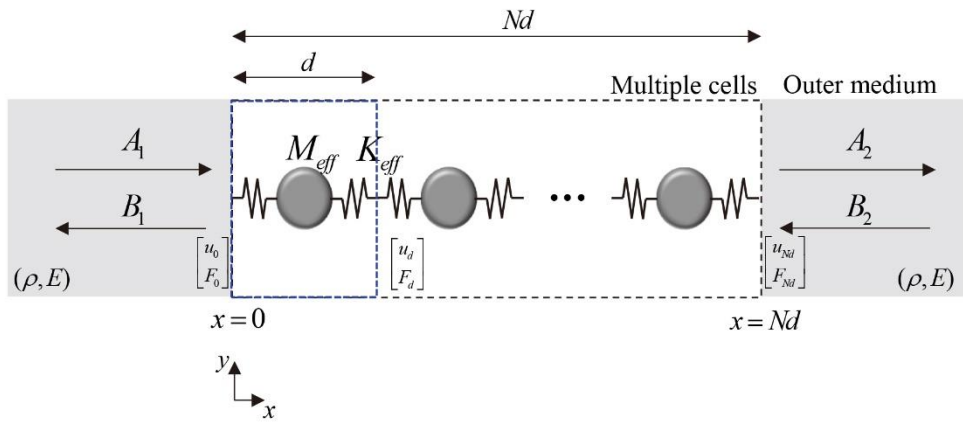


Fig. 3.5 Lumped element model composed of unit cells embedded within continuum outer elastic medium for wave transmission analysis.

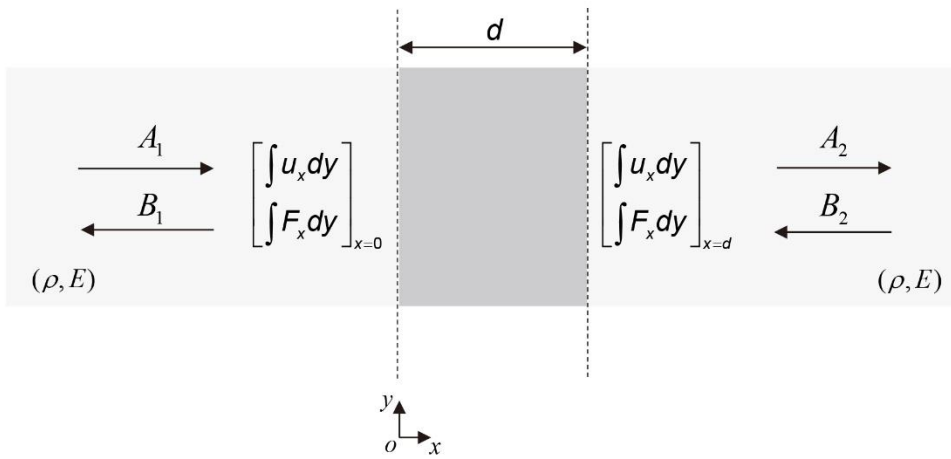


Fig. 3.6 Numerical simulation model (also experimentally feasible) to calculate the transfer matrix components.

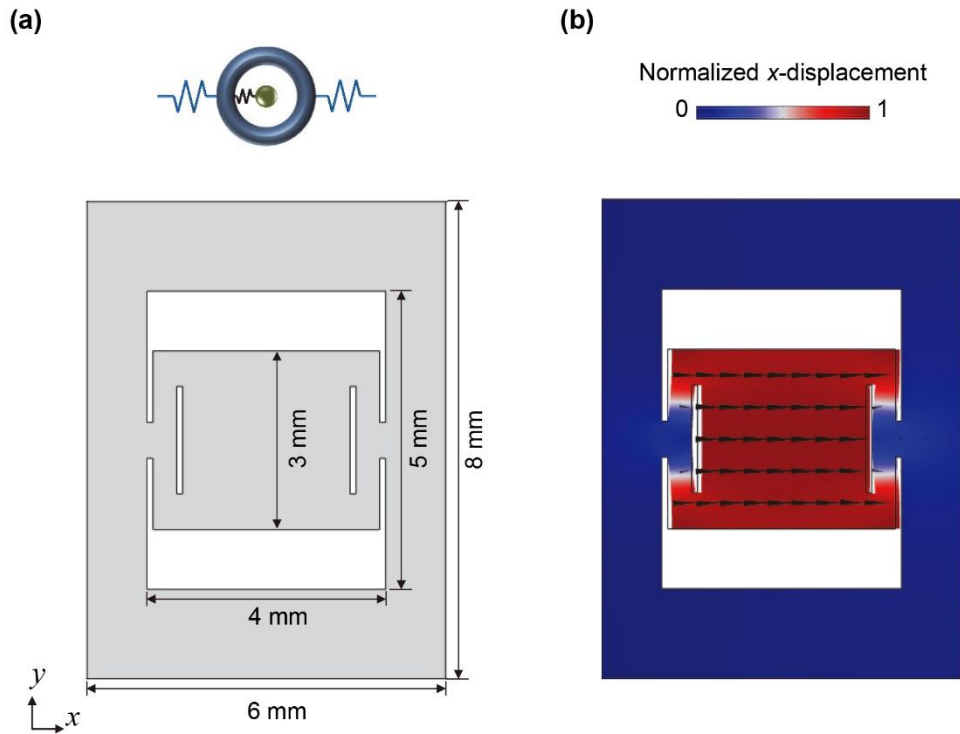


Fig. 3.7 (a) Dipolar cell design for single-phase continuum material. (b) Dipolar resonance mode shape near the resonance frequency.

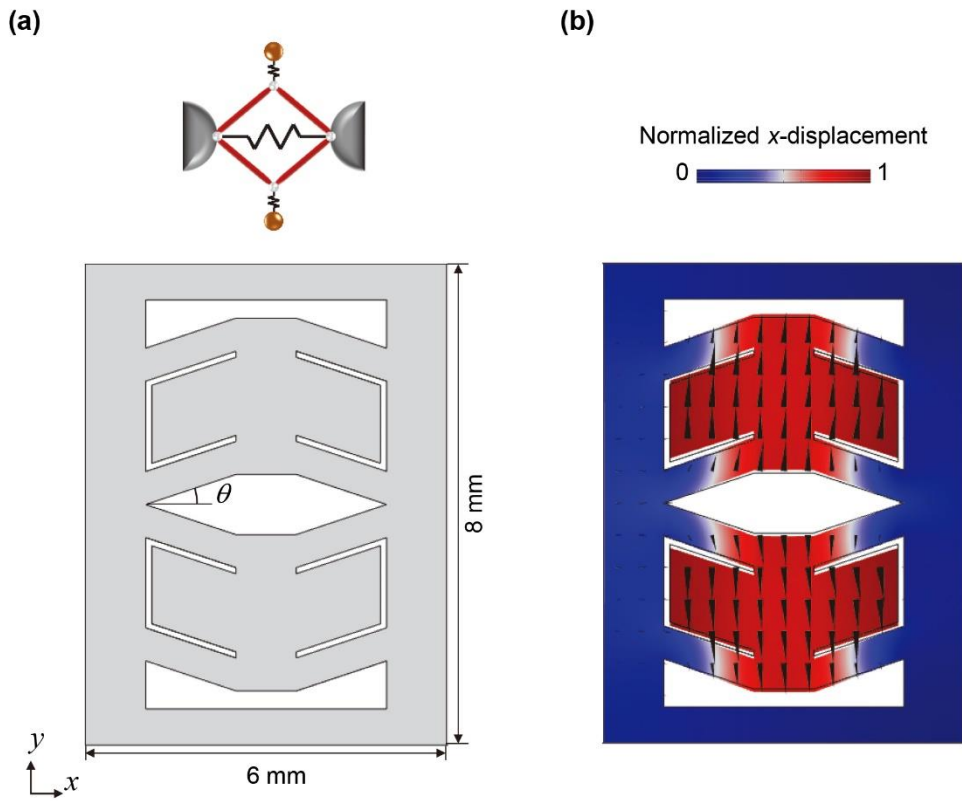


Fig. 3.8 (a) Monopolar cell design for single-phase continuum material. (b) Monopolar resonance mode shape near the resonance frequency.

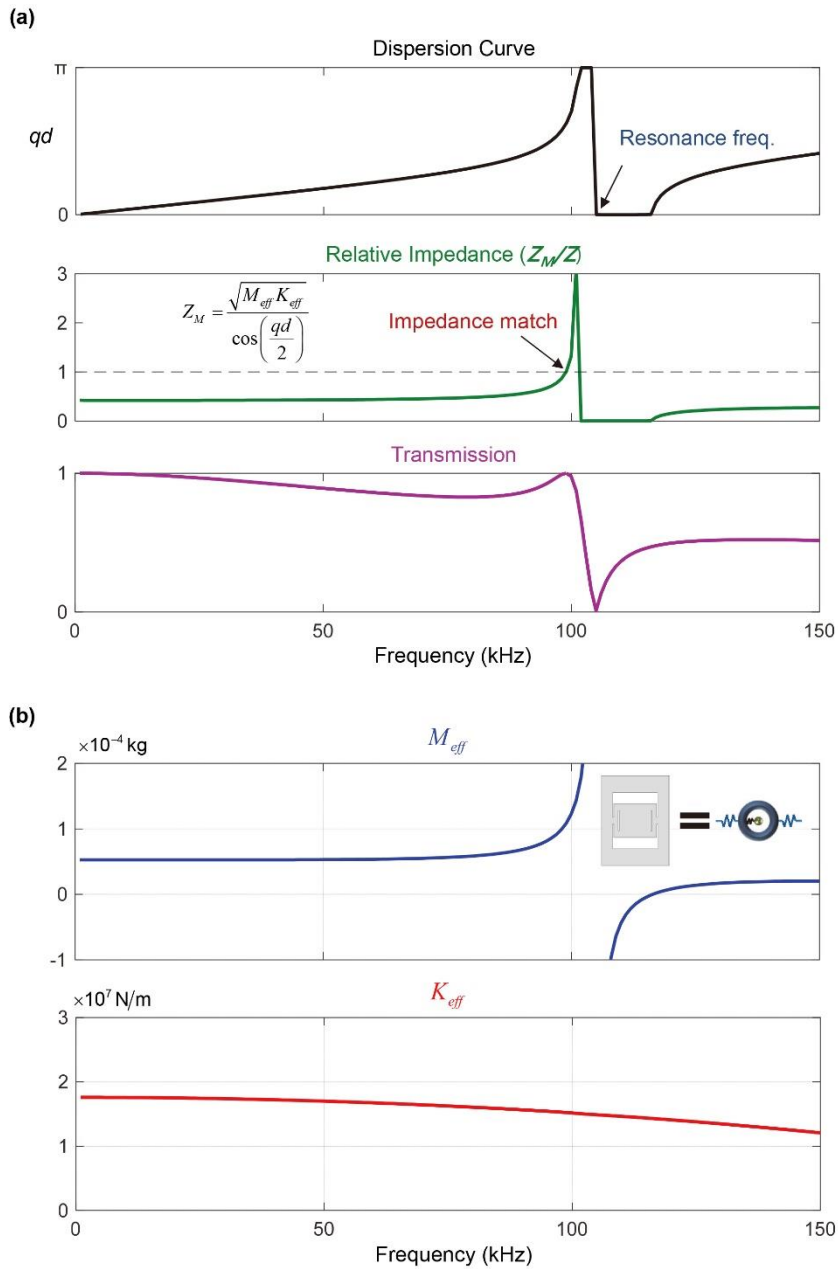


Fig. 3.9 Numerical analysis for the dipolar cell. (a) (From top to bottom) Dispersion curve, relative impedance, and transmission spectrum retrieved by the transfer matrix method. (b) Effective parameters retrieved by the transfer matrix method.

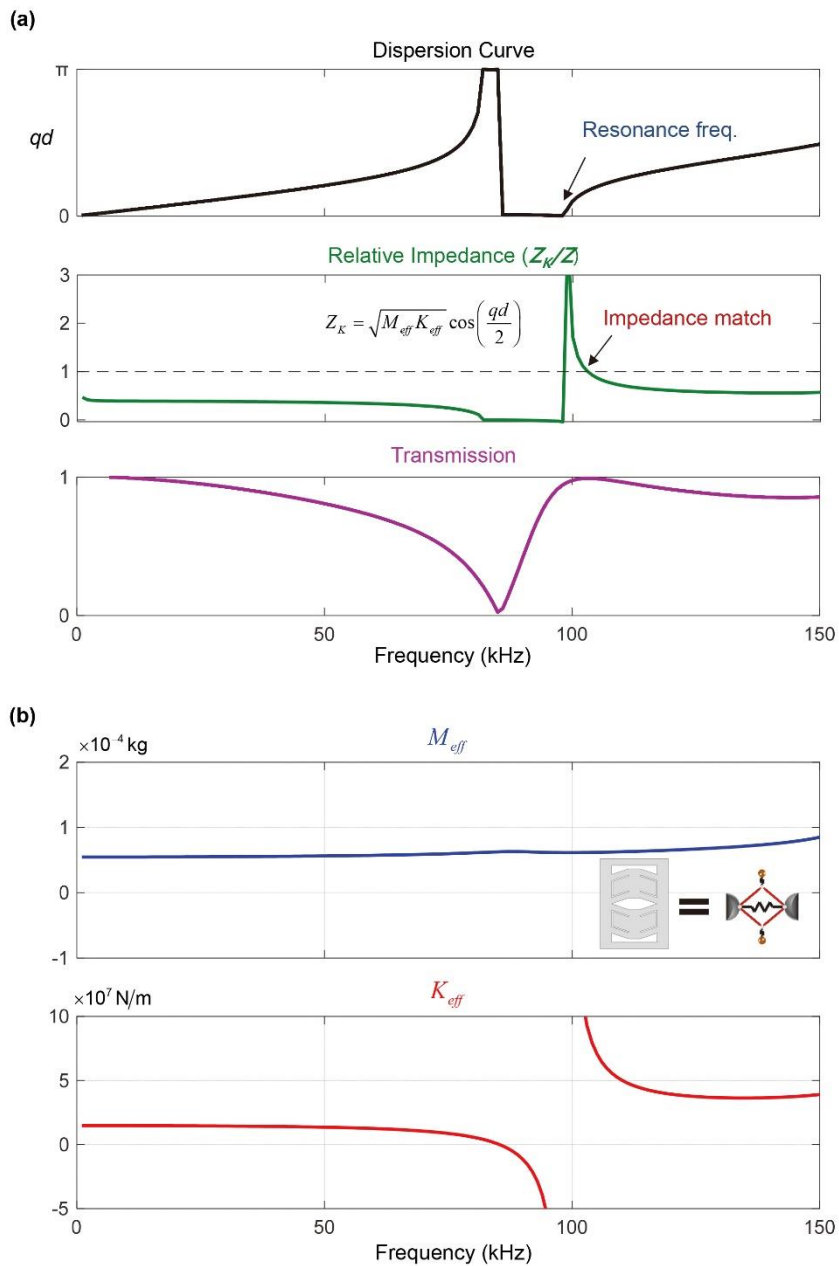


Fig. 3.10 Numerical analysis for the monopolar cell. (a) (From top to bottom) Dispersion curve, relative impedance, and transmission spectrum retrieved by the transfer matrix method. (b) Effective parameters retrieved by the transfer matrix method.

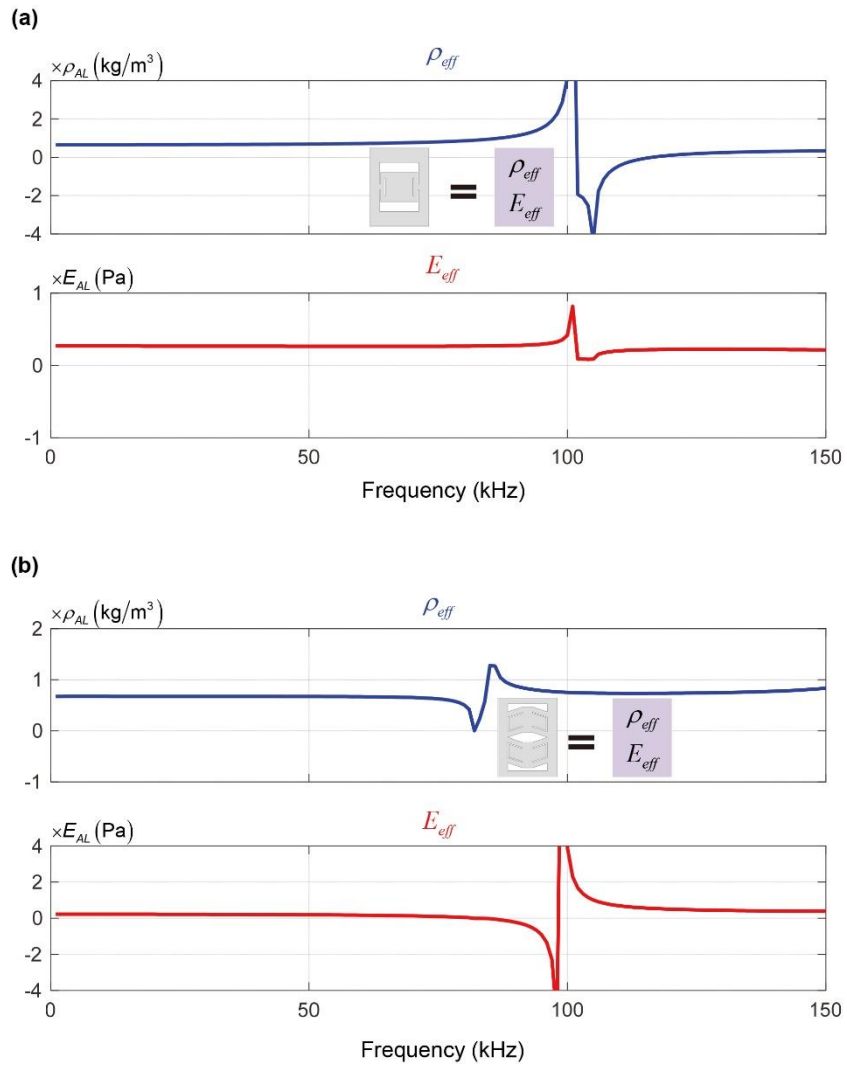


Fig. 3.11 (a) Dipolar and (b) monopolar cells retrieved with homogenized material assumption

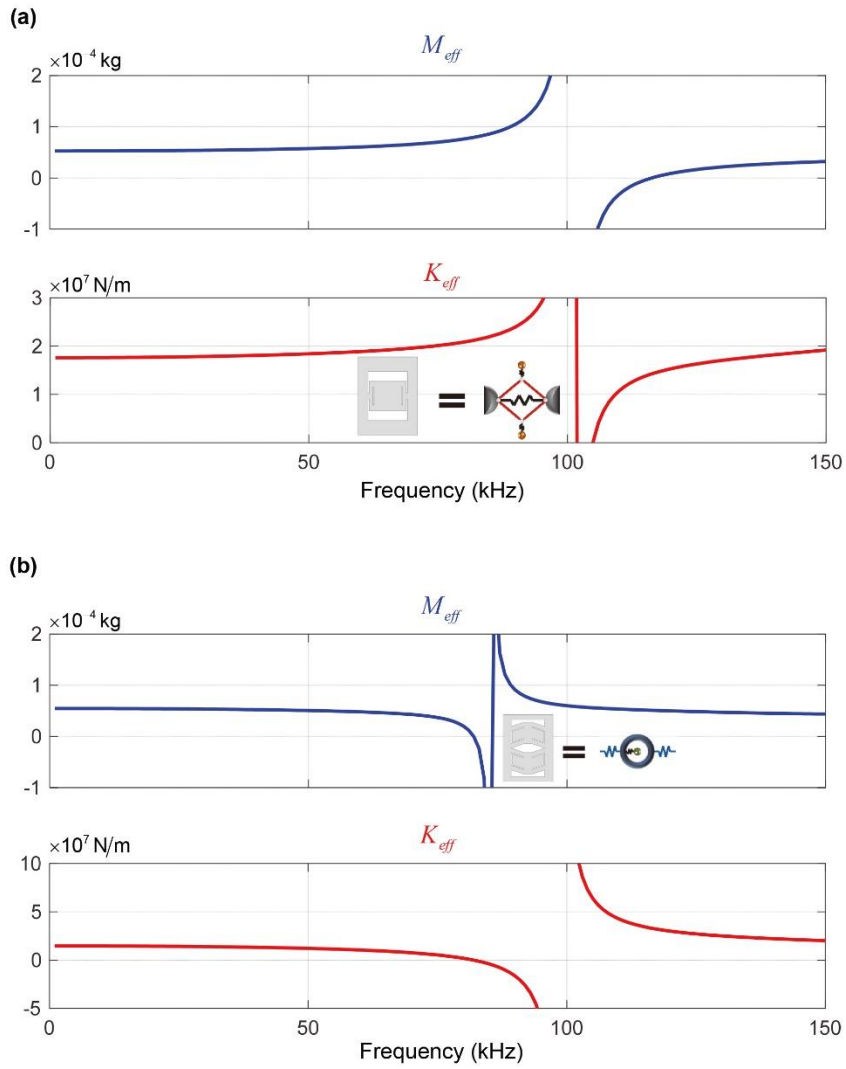


Fig. 3.12 (a) Dipolar and (b) monopolar cells retrieved by other models (monopolar and dipolar, respectively).

<CHAPTER 4>

ELASTIC METASURFACE FOR HIGH TRANSMISSION ANOMALOUS BEAM REFRACTION

4.1 Chapter Overview

Metasurfaces [31, 32, 72, 73] have recently opened doors for innovative ways to manipulate the wave fields owing to its fascinating capability of realizing the extreme features of bulky metamaterials within a much more compact and easily-fabricated form. The very basic priority of such concept is to abruptly shift the phase within a subwavelength structural layer. Related works including anomalous refraction [33, 34, 74-80] and reflection [81-86], control of polarization [87, 88], holography techniques [89, 90], self-accelerating beams [91-93] and even cloaking phenomena [94-96] have succeeded in both optics and acoustics. On the other hand, to achieve the best performance, extended works [33, 34, 74-79] were established so that every sub-element realizes not only the abrupt phase change but also high and even energy transmission, ensuring that none of any parts distort the designed beam pattern.

As for the elastic counterpart, it is also no exception that such a highly performing

metasurface technique is significantly demanded regarding the broad range of potential applications including bio-medical imaging and non-destructive evaluation. However, analogous research still remains formidable due to lack of methodology to ensure the abrupt phase shift as well as high transmission which are governed by elastic constitutive parameters; density and stiffness. In fact, according to the well-known Ashby chart [97, 98], these factors show intrinsic proportionality (stiffness \propto mass) in most natural elastic solids even including engineered cellular structures [99-101] and single-phase elastic metamaterials [35-39, 102, 103]. In particular, conventional elastic metamaterials demonstrating wide range of M_{eff} and K_{eff} based on resonant mechanism [35, 36, 38, 39] also suffer from the intrinsic coupling of the parameters due to structurally connected deformation. Such innate feature is the main obstacle especially for designing a metasurface structure because there exists an inevitable trade-off between phase velocity ($\propto \sqrt{K_{eff}/M_{eff}}$) and impedance ($\propto \sqrt{M_{eff}K_{eff}}$), which are responsible for the phase shift and transmission, respectively. For example, a recently proposed elastic metasurface [104] relied on local resonance effect to obtain amplified M_{eff} only to ensure the 2π phase span, which consequently resulted in a very low transmission efficiency of 25%. Although more recently Liu *et al.* [37] compensated impedance by evanescent modes for flexural Lamb waves, decreased M_{eff} and K_{eff} fundamentally hinders the full transmission condition. As such,

designing the ‘best-functioning’ elastic metasurface requires not only opposite but also delicate tuning of M_{eff} and K_{eff} so that no trade-off between the phase shift and transmission exists.

Thus, in this chapter, we propose a novel approach to spatially decompose into parts that exclusively contribute to M_{eff} and K_{eff} against incoming elastic longitudinal waves. In contrast to the traditional approaches that implemented resonances [35, 36, 38, 39] or composites [41-43] concerning elastic metamaterials, our structure is composed of spatially separated substructures so that each property is actually decoupled by its own geometrical parameter. In this way, each substructure embedded in elastic solids actually behave as the mass and spring parts, respectively, equivalent to the analytic mass-spring model which is well-known for its excellent analogy [35, 36, 38, 39] for designing elastic metamaterials. Our theoretical approach by the analytical discrete mass-spring model mainly concerns to find the right design parameters to ensure the whole 2π phase span as well as impedance matching condition when assembled into an elastic metasurface structure.

For the actual realization of the metasurface, we employ a single-phase elastic medium (here, aluminum) for convenient fabrication and integration. The K_{eff} - substructure is actualized as an elastic block with multiply-perforated thin slits for minimal air filling fraction to minimize the effect on M_{eff} [102, 103, 105]. Similar to the labyrinthine metamaterial [79, 80, 83] belonging to the acoustic

counterpart, we obtain high refractive index (slow medium) in a non-resonant manner by weakening K_{eff} to conveniently accumulate the wave phase within subwavelength scale. On the other hand, the M_{eff} -substructure is realized as a continuum block containing a local resonator to induce the dipolar resonance. This mechanism is confirmed to particularly tune and amplify M_{eff} just below the resonance frequency, which is crucial for matching the impedance as well as lowering the phase velocity. The decoupling is also attributed to the fact that both substructures have relatively firm continuum boundaries so that they affect each other only little. Therefore, the independent tuning of M_{eff} and K_{eff} by employing the substructures allows easy adjustments of the design parameters necessary for both the full 2π phase coverage and high transmission. For further validation, numerical simulation and experiment employing in-plane elastic longitudinal waves are provided to confirm the feasibility of high transmission anomalous beam steering based on the generalized Snell's law. The proposed substructure theory along with promising results are expected to offer a powerful design methodology especially for elastic metasurfaces which can be used in various applications.

4.2 Generalized Snell's Law

The basic principle is to break the classical Snell's law where the main assumption lies in the fact that phase at the boundary stays unchanged. The Generalized Snell's

law [31, 32, 72, 73] considers an extra phase accumulation within the boundary to yield any arbitrary refracted beam profile as shown in Fig. 4.1(a). This theorem revises the classical Snell's law by imposing extra phase gradient term $d\varphi/dx$ in the transverse direction (x -direction) as

$$k_0 \sin \theta_t = d\varphi/dx + k_0 \sin \theta_i. \quad (4.1)$$

where θ_i is incident angle, θ_t , refracted angle, and k_0 , the wavenumber of outside medium. The gradient phase accumulations induce an additional wave momentum that enables the design of any artificially engineered refracted beam pattern. Therefore, it is important to design the unit cells of different phase shifts while achieving even and high transmission.

4.3 Mechanics of Substructured Unit Cell

Fig. 4.1(b) schematically shows the anomalous beam steering that we aim to achieve using our elastic metasurface. Throughout this study, elastic waves are assumed to be incident upon the metasurface along the x -direction and the wave motions are polarized (longitudinal) in the x -direction. When a plane wave is incident upon the stacked structure composed of elastic unit cells, the transmitted beam can have any arbitrary form depending on the combination of unit cells. The total thickness of the four-unit stacks as well as the interval between the neighboring unit cells in the y -direction are all within the subwavelength scale. The configuration of the constituent unit cell is shown in Fig. 4.2(a). The uniqueness of

the proposed unit cell lies in the fact that it is spatially substructured into two microstructural parts, namely the M_{eff} -substructure and K_{eff} -substructure, as shown in the figure. The independent, arbitrary mass-stiffness tuning substructures allow full-transmission 2π phase change over the subwavelength metasurface.

The analytic discrete model of the substructured unit cell is shown in Fig. 4.2(b). The continuum counterparts of the discrete mass and stiffness elements are also shown in the figure. The main mass denoted by M consists of a local resonator (mass m with spring k_r), and is connected to each other by an effective spring. The blue part predominantly controls M_{eff} whereas the red part controls K_{eff} . Due to the unique configurations of the two substructures, the effective stiffness can be weakened to obtain a high refractive index (phase velocity $\propto \sqrt{K_{eff}/M_{eff}}$) while the effective mass can be amplified for impedance compensation (impedance $\propto \sqrt{M_{eff}K_{eff}}$). The weakened stiffness is represented as springs of reduced stiffness, which are actualized by the off-centered perforated double slits [102, 103]. On the other hand, for controlling, we utilize a local dipolar resonator, which is realized as a small mass attached to the two slender vertical beams connected to the base medium. In the continuum model, the stiffness k_r (which consequently manipulates M_{eff}) and K_{eff} can be tuned by the width w of the slender beam in the M_{eff} -substructure and the slit length l in the K_{eff} -substructure, respectively.

The underlying physics of the substructures can be found in Figs. 4.3(a) and 4.3(b)

by observing each of their eigenmodes. The M_{eff} -substructure is designed to exhibit dipolar behavior to effectively manipulate M_{eff} . At the target frequency of 100 kHz, the width (w) of the slender beam directly affects k_r , which mainly adjusts the resonance frequency while barely affecting the overall stiffness of the unit cell. Accordingly, the numerically retrieved parameters in Fig. 4.3(c) show that M_{eff} attains a wide range of values due to the resonant behavior, whereas K_{eff} remains unaffected by the w values. The effective parameters are normalized to those of aluminum (M_{al}, K_{al}), which has the same size as the unit cell (details are presented in Table. 4.1).

On the other hand, the K_{eff} -substructure is designed to exhibit a non-resonant mechanism by perforating multiple thin slits that efficiently harness a low stiffness value. As shown in Fig. 4.3(b), extreme deformation is confined to both sides of the perforated regions (K_{eff} -substructures), thus inducing the whole unit cell to react in a much softer manner. Small filling ratios are implemented for the air-perforated slits (which possess much lower stiffness than the base metal) in order to produce little effect on M_{eff} , while their elongated geometry in the y -direction substantially lowers K_{eff} (see subsection 4.3.2 for further analysis). Thus, K_{eff} decreases with increase in slit length l , whereas M_{eff} remains rather unaffected. While calculating M_{eff}/M_{al} and K_{eff}/K_{al} for the M_{eff} -substructure, the region

originally hosting the slits is assumed to be fully filled with the base medium (as shown in Fig. 4.3(a)). On the other hand, while calculating M_{eff}/M_{al} and K_{eff}/K_{al} for the K_{eff} -substructure, the region originally hosting the central resonator is also assumed to be fully filled with the base medium (as shown in Fig. 4.3(b)). In this way, we can ascertain how the constitutive properties are affected by each substructure embedded in the base medium having the same periodicity. To investigate the combined effect of both the substructures, we also derive the effective properties of the entire unit cell, which is shown in Fig. 4.3(e-f).

The contours in Figs. 4.3(e) and 4.3(f) clearly show that M_{eff} and K_{eff} are predominantly determined by the geometrical parameters w and l , respectively. Hence, our whole unit cell structure can be tuned by adjusting the beam width of the M_{eff} -substructure and the slit length of the K_{eff} -substructure.

4.3.1 Analysis on each substructure

a) Linear superposition

In order to deeply understand the mechanism of substructuring, we retrieve the effective parameters for each substructure as shown in Fig. 4.4(a). Each substructure by itself shows great tunability for their responsible parameters, which has already been proven in Fig. 4.3. Each parameter is normalized to the properties of the background medium of corresponding dimension as stated in Table 4.1. Also,

we further investigate their robustness by linear superposition as shown in Fig. 4.4(b). When linearly superposed, the total value of M_{eff} and K_{eff} for the whole unit cell is drawn in the figure. The masses are summed up linearly, whereas the spring term is calculated as a series spring. Both the effective parameters retrieved from superposing discrete substructures and the whole unit cell show great agreement, thus confirming the suitability of treating the whole unit as a combination of the constituent substructures.

b) Transmission/Phase of metasurface composed of each substructure only

We also investigate the transmission and phase spectra with metasurfaces that are composed of each substructure, respectively, to confirm the necessity of substructuring to eventually obtain independent tuning of the effective properties. For the M_{eff} -substructure case as shown in Fig. 4.5(a), the results show that near the resonant state (near $w=0.45$ mm), abrupt phase shift accompanies severe transmission loss as proven in previous works [4]. To conserve the periodicity, aluminum blocks are utilized to replace the K_{eff} -substructures. Thus, we fix K_{eff} value to carefully investigate the transmission and phase spectra only depending on M_{eff} (by changing w). On the other hand, the K_{eff} -substructure case as shown in 4.5(b), gradual phase shift based on non-resonant manner similar to labyrinthine or coiling-up metamaterials [5] can be observed. However, this method inevitably induces huge impedance mismatch so that the transmission dip occurs as shown in

the figure. Overall, theoretical prediction by mass-spring model agrees very well with the simulation. These results well summarize our main idea to pursue simultaneous implementation of low K_{eff} and high M_{eff} to ensure high transmission.

4.3.2 Analysis on the geometry of slits to control stiffness

In this subsection, we introduce the backgroun of designing the K_{eff} -substructure to exclusively tune K_{eff} while little affecting M_{eff} . The design can be conceptually explained with Fig. 4.6(a) which represents the composite laminate structure composed of metal and air. The anisotropic elastic modulus and scalar mass density can be defined as

$$E_x = f_m E_m + f_a E_a \quad (\text{rule of mixture}), \quad (4.2a)$$

$$E_y = \left(\frac{f_m}{E_m} + \frac{f_a}{E_a} \right)^{-1} \quad (\text{inverse rule of mixture}) \quad (4.2b)$$

$$\rho = f_m \rho_m + f_a \rho_a, \quad (4.2c)$$

where the subscripts m and a denote for metal and air, respectively. Here, $f_m = V_m / (V_m + V_a)$ and $f_a = V_a / (V_m + V_a)$ are the volume fraction. Because we utilize aluminum, the properties will be $E_m = 70\text{GPa}$, $E_a = 101\text{kPa}$ (air in constant temperature), $\rho_m = 2700\text{kg/m}^3$, and $\rho_a = 1\text{kg/m}^3$. Because the properties of the metal are extremely greater than that of air, wide range of tuning

can be possible with various geometrical design.

The K_{eff} -substructure is conceptually decomposed into multiple layered structures as shown in 4.6(b). The yellow rectangles denote the metal-air sub-elements. Three of the yellow rectangles and the background metal medium make up the whole unit cell. The sub-composites denoted with yellow rectangles are the enabling key for lowering the stiffness in the x -direction. The elastic modulus of a sub-composite can be calculated as

$$E_x^* = 16 \left(\frac{15}{E_m} + \frac{1}{E_a} \right)^{-1} \quad (\text{inverse rule of mixture}), \quad (4.3)$$

considering the dimensions stated in the figure. Then, summing three of these parts and the background medium, the elastic modulus and mass density can be derived as

$$E_x^{total} = [3E_x^* + (10 - 3l)E_m] / 10 \quad (\text{rule of mixture}), \quad (4.4a)$$

$$\rho^{total} = \frac{(16 - 0.1 \times 3l)\rho_m + 0.1 \times 3l\rho_a}{16}. \quad (4.4b)$$

By substituting the aforementioned material properties into Eqs. (4.4a-b), we can visualize the relation of modulus and mass density with respect to the slit length as shown in Fig. 4.6(c). One can clearly see that even with minimal air filling fraction, the geometrical factor can extremely affect the modulus while merely affecting the mass density.

In Fig. 4.7, the design issues of the slits are shown by comparing the off-centered triple slits with single-slit geometries. In Fig. 4.7(a), the original unit cell having

off-centered multiple slits and its effective properties are plotted as functions of the slit length l . The eigen-mode shapes at specific points on the dispersion curves are also presented. The examination of the mode shapes confirms the physical mechanism of resonance phenomena which was also explained by the lumped mass-spring model. In Fig. 4.7(b), such single-slit unit cell is considered to justify the effectiveness of the original unit cell. To properly compare how the slit length change the parameter, we set l^* to be $2l$ because the two aligned slits dominantly weaken the overall stiffness in the original unit cell. The obtained effective properties of the single-slit unit cell confirm that it can achieve the target stiffness at a specific frequency. However, the weakened bending stiffness of the single-slit unit cell forms an additional unwanted mode shape at a lower frequency as can be seen in the dispersion curve. The slits exhibit flappy motions (unwanted resonance due to weakened bending stiffness) at around 50 kHz. This unwanted and unexpected phenomenon causes severe mismatch between the semi-analytical and numerical results. Although this unit cell can achieve the desired parameter at the target frequency (magenta line), the unwanted mode shape is not desirable for lumped system based design. On the other hand, the proposed multiple slits stabilize the continuum structure so that only the longitudinal stiffness can be dominantly controlled. As a result, our unit cell is well matched with the lumped mass-spring model even in the lower frequency region.

4.3.3 Dispersion relation

Since the system is designed as a periodic structure, it is governed by the well-known Bloch relation. The dispersion of the 1st Brillouin zone for the case of $w=0.5$ mm and $l=2.5$ mm is shown in Fig. 4.8(a). The circles are obtained from the eigen-frequency analysis module embedded in COMSOL Multiphysics. The solid lines are drawn by substituting the retrieved effective parameters from Fig. 4.8(b) into Eq. (3.23). They are described as ‘semi-analytical’ because M_{eff} and K_{eff} in Fig. 4.8(b) are calculated numerically (using Eqs. (3.59a-b)) and then substituted into the theoretical Eq. (3.23). As shown in Fig. 4.8(a), the dispersion curves drawn by both methods show a good agreement. The dispersion curve represents how the wavenumber of the metasurface can be manipulated to increase greater than that of the outer medium (which is responsible for lowering the phase velocity) at the target frequency (indicated by the magenta line) depending on the effective properties.

4.4 Transmission and Phase Spectra for Multiple Unit Cells

To thoroughly characterize the transmitted wave, we derive the transmission coefficient of the elastic metasurface structure (N layers of unit cells) embedded in a continuum elastic medium as shown in Fig. 4.9(a). Here we can utilize the transmission coefficient that were derived in Eq. (3.52) with the system impedance term for the M_{eff} -substructure model such that

$$T = \frac{2}{2 \cos(Nqd) + i \left(\frac{Z}{Z_s} + \frac{Z_s}{Z} \right) \sin(Nqd)}, \quad (4.5)$$

where

$$Z_M = \frac{\sqrt{M_{eff} K_{eff}}}{\cos\left(\frac{qd}{2}\right)}, \quad (4.6)$$

so that

$$T = \frac{2}{2 \cos(Nqd) + i \left(\frac{Z \cos(qd/2)}{\sqrt{M_{eff} K_{eff}}} + \frac{\sqrt{M_{eff} K_{eff}}}{Z \cos(qd/2)} \right) \sin(Nqd)}. \quad (4.7)$$

Then, the phase shift can be straightforwardly derived as

$$\varphi = \arg \left[- \left(\frac{Z \cos(qd/2)}{\sqrt{M_{eff} K_{eff}}} + \frac{\sqrt{M_{eff} K_{eff}}}{Z \cos(qd/2)} \right) \tan(Nqd) \right], \quad (4.8)$$

In this way, we can efficiently explore the transmitted wave characteristics based on the effective properties. Additionally, the simulation shown in Fig. 4.9(b) illustrates how the metasurface structure squeezes the wave phase within itself compared to that of the base medium in order to shift the phase abruptly at the output boundary. Here, the input longitudinal wave was exerted on the left side, whereas the PML conditions were applied at the ends to eliminate the reflected waves (not shown in the figures for brevity). In addition, periodic boundary conditions were applied to the upper and lower boundaries in accordance with the plane wave assumption. Detailed description of the simulation set-up along with

various cases of transmission by using different unit cells is presented in Fig. 4.10. In Fig. 4.10(a), the whole simulation set-up for the case of full transmission (Fig. 4.9(b)) is presented. The PMLs at the ends rapidly eliminate wave reflection, thus satisfying the reflection-free assumption. The magnitude of the x -directional displacements are plotted to visualize the exact wave fields in all regions. Fig. 10(b) shows the transmission plots for different (l,w) combinations. If the geometric parameters (l,w) are not properly selected, $|T|$ can be much smaller than unity. The transmission coefficients are calculated numerically using Eq. (3.57).

To verify the effects of number of unit cells on transmission spectra, we compare the results both by theoretical analysis and numerical calculation as shown in Fig. 4.11. In Fig. 4.11(a), the effective properties are initially calculated with a ‘single cell’ by the numerical method described in subsection 3.4.2. The semi-analytical dispersion curve can thus be obtained by Eq. (3.55). Here, $w=0.5$ mm and $l=2.5$ mm are applied, which are the same as those used in Fig. 4.8. For the transmission, we utilized both the semi-analytical and numerical methods. As explained above, the semi-analytical results can be obtained by substituting the retrieved effective parameters into the transmission coefficient of the lumped mass-spring model. On the other hand, the numerical results are obtained by substituting the boundary responses in Eqs. (3.53a-d) into the transmission formula as in Eq. (3.57). The equations are shown in the figure for convenience. It should be noted that as for one cell, the semi-analytical and the numerical results are the same because the effective parameters are derived from one cell.

For multiple N cells as shown in Fig. 4.11(b), we compare the transmission curves obtained from the semi-analytical and numerical methods. It can be clearly observed that the results obtained by both methods show good agreement with each other. It can also be observed that in addition to the impedance matching condition (which is fixed at a specific frequency), more tunneling frequencies appear as N increases.

4.4.1 Full transmission condition due to impedance matching and tunneling

To ensure the full transmission condition (viz., $|T|=1$), we mainly consider the impedance matching condition as

$$Z_M = Z \quad \text{equivalently,} \quad M_{eff} = \frac{4K_{eff}Z^2}{4K_{eff}^2 + (\omega Z)^2}. \quad (4.9)$$

Alternatively, $|T|=1$ can be achieved if the following tunneling condition [50] is satisfied:

$$Nqd = m\pi \quad \text{equivalently,} \quad M_{eff} = \frac{4K_{eff}}{\omega^2} \sin^2\left(\frac{m\pi}{2N}\right) \quad (m=1,2,\dots,N-1). \quad (4.10)$$

The tunneling condition is similar to the well-known Fabry-Perot condition and is dependent on the thickness of the material.

Figs. 4.12(a) and (b) visualize the parametric studies on how M_{eff} and K_{eff} change the metasurface properties at the target frequency of 100 kHz. Fig. 4.12(a)

shows the contour plots of the relative impedance $Z_r = Z_M / Z$ and the phase velocity (V_p) of the discrete mass-spring system [41] defined as

$$V_p = d \sqrt{\frac{K_{eff}}{M_{eff}}} \left| \frac{\sin(qd / 2)}{qd / 2} \right|, \quad (4.11)$$

These plots are considered to check whether the exact impedance match (i.e., $Z_r = 1$) can be realized within the M_{eff} and K_{eff} ranges of our substructured unit cell stacks, and whether the phase velocities can be varied sufficiently to cover the 2π phase change. The first observation is that there exists a line satisfying Eq. (4.9) or $Z_r = 1$ within the selected ranges of M_{eff} and K_{eff} , implying that we can choose a different (M_{eff}, K_{eff}) combination along the line in order to attain the desired phase change. The phase velocity contour plot also suggests that a wide range of phase velocities can be selected while $Z_r = 1$ is satisfied.

Fig. 4.12(b) shows the contour plots of the transmission and phase changes on the $M_{eff} - K_{eff}$ plane. On the transmission contour, the full transmission occurs either along the $Z_r = 1$ (impedance matching) curves or the lines of $m=1, 2,$ and 3 (tunneling). Besides the points on the curve or lines, there are many points on the contour where nearly full transmission occurs. Therefore, our substructured unit cell configuration offers a wide selection of (M_{eff}, K_{eff}) combinations as far as the transmission is considered. The phase-change contour on the right side of Fig. 4.12(b) shows that the full span of 2π phase shift can be achieved with the selected

ranges of M_{eff} and K_{eff} . These ranges are selected because they can be realized with the proper selection of the design parameters (w, l). The points where the full transmission occurs are also plotted as the impedance-matched curves of M_{eff} and K_{eff} tunneling lines of $m=1, 2$, and 3 . While each of the tunneling lines gives the same phase change, the impedance-matching line covers a wide range of phase shifts. Therefore, we utilize the $M_{eff} - K_{eff}$ zone of low stiffness and enhanced mass near the impedance-matching curves for our metasurface design.

For the above mentioned analysis, we set the number of unit cells to be $N=4$, so that it efficiently covers the 2π phase span, while still retaining the total length (Nd) within the subwavelength scale. The theoretical transmission/phase spectra and phase shift coverage depending on the number of unit cell(s) are shown in Fig. 4.13. From the figures, it can be implied that the range of phase coverage increases along with the number of unit cells. To properly ensure the whole 2π coverage, we utilize 4 stacks of unit cells in this work regarding Fig. 4.13(d). In addition, although it is clear that more stacks of unit cells allow wider phase coverage, we choose N to be 4 so that the whole thickness of the metasurface structure is within subwavelength scale.

4.4.2 Unit cell geometry variation for both full transmission and 2π phase coverage

For the specific design of our metasurface, we perform simulation with the actual

cell by varying the geometrical variables. We first evaluate the characteristic impedance and phase velocity of a single unit cell by substituting the retrieved effective properties into theoretical Eqs. (4.6) and (4.11), respectively. The corresponding results are shown in Fig. 4.14(a). Here, the impedance matching line can be drawn as similar to the theoretical analysis in Fig. 4.12. Additionally, the phase velocity plot shows that the impedance matching curve passes through wide range of phase velocities.

In Fig. 4.14(a), we plot the transmission and phase contours on the l - w plane and the 12 points that can shift the phase by $30^\circ \times n$ (where n varies from 1 to 12). The contour plots in Fig. 4.14(a) were drawn with increments of $50 \mu\text{m}$ and $2 \mu\text{m}$ for l and w , respectively. The impedance matching and tunneling curves based on the obtained effective parameters are also illustrated in this figure. For choosing specific subunits, we use 12 unit cells of varying configuration to achieve the 2π phase span along the y -direction. The geometric values for the 12 unit cells can be selected near the impedance matching curve as shown in Fig. 4.14(b). It is worth noting that the dimensions and step sizes of the geometrical parameters have been selected in such a way that they are feasible with the current manufacturing technology. Thus, some feasible candidates are chosen outside the impedance matching curve. It is also worth pointing out that slight discrepancies exist between the analytically derived curves (which are calculated by substituting the numerically retrieved parameters into Eqs. (4.9) and (4.10)) and the transmission spectra, where the values possess full transmission on the curves. The main reason

can be attributed to the local interactions among the multiply stacked continuum unit cells, which cannot be fully expressed by the analytical discrete mass-spring model. Nevertheless, the proposed metasurface achieves almost full transmission as well as complete 2π phase shift if the design parameters (l,w) of the substructured unit cell are properly chosen. The specific values of (l,w) for the 12 unit cells are summarized in Table 4.2.

The transmission ratio and the amount of phase shift for each of the selected unit cells are plotted in Fig. 4.14(c). Representatively, unit cells #1 and #11, which have quite different geometric parameters, are shown within the graph. For all the chosen unit cells, the transmissions are guaranteed to be higher than 0.9, in addition to their phase intervals being well matched to the desired phase profiles. It should be noted that the discrepancy in the theoretical calculation (where transmission should be unity) can be attributed to the interactions of the elastic unit cells, whose original characteristics as a single unit cell are affected when stacked together. On the other hand, it should also be noted that various other candidates with different phase shifts could be chosen as well to obtain an elastic metasurface. Such flexibility provides a concrete design chart for various properties in numerous cases.

Fig. 4.15(a) shows the phase shift plot in an elastic medium where the designed substructured unit cells of various geometries are inserted. The results are for unit cells whose phases are shifted by multiples of 60° . The incident wave is a plane elastic longitudinal wave. The cases with phase shifts of multiples of 45° are

presented in Fig. 4.15(b). Figs. 4.15(a-b) clearly show how effectively and accurately the designed unit cells achieve the required phase shift by slowing the wave to accumulate the phase within them. Since each of the designed unit cells has a transmission ratio of over 90%, they can serve as excellent elements for exclusively tuning the elastic longitudinal mode.

In summary, it would be worthwhile noting that the main purpose of the analytical lumped model is to “facilitate the design of the unit cell and to provide a solid physical explanation.” With the help of our analytic model, we were able to find the essential effective parameters of the unit cell, and then realize them by the substructuring mechanism.

Furthermore, we were able to estimate the impedance matching condition (which is explicitly derived by our model for a discrete system) and the range of phase shift within a given range of mass and stiffness properties. Even when they were multiply aligned, we could calculate the transmitted wave characteristics with the transfer matrix method. Inversely, we were able to calculate the necessary values of mass and stiffness that a unit cell should possess to induce the impedance matching condition as well as ensuring 2π phase change.

We can summarize how our analytical model is utilized to estimate any desired conditions as below.

1. By Fig. 4.12, we theoretically showed the relation between impedance (transmission) and phase velocity (phase shift within the structure) with respect to the effective mass and stiffness, to conveniently visualize the desired values.

2. The transmission and phase shift of metasurfaces consisting of only one kind of substructure (shown in Fig. 4.5) are analyzed both numerically and theoretically. This figure also justifies the necessity of both substructures to construct a metasurface structure for full transmission.
3. The minimum number of unit cells to cover the 2π phase shift range was estimated (shown in Fig. 4.13).

4.5 Numerical Simulation of the Refracted Beam Pattern Manipulation

In this section, we numerically investigate how effectively our substructured metasurface manipulates the beam patterns. We consider three cases of beam pattern manipulation, and the finite element results obtained from COMSOL Multiphysics are shown in Fig. 4.16. To send an incident longitudinal wave into the metasurface, a 0.3 m-wide line source with a harmonic force in the perpendicular direction (x -direction) was placed 0.15 m below the metasurface. In all the plots shown in Fig. 4.16, the divergence of the displacement field is presented to represent the longitudinal wave components. In addition, the divergence is normalized to that of the input maximum.

Fig. 4.16(a) shows the case of $d\varphi/dy = \pi/6h$. There are three superlattices along the y -direction, and each of them is composed of 12 unit cells. The values of their geometric parameters (l , w) are provided in Supplementary Table 4.2 and their

phase-shifting performance can be verified from Fig. 4.15(a). According to Eq. (4.1), the theoretically calculated refraction angle in this case is $\theta_t = (1/k_0) \sin^{-1}(\pi/6h) \approx 26.7^\circ$, which corresponds well with the simulation as indicated in Fig. 4.16(a). As shown in the lower part of Fig. 4.16(b), we developed the metasurface in a somewhat different manner by utilizing pairs of $\pi/4$ steps of unit cells to realize a phase gradient of $d\varphi/dy = \pi/8h$. Similar to that in the former case, the theoretical refraction angle $\theta_t = (1/k_0) \sin^{-1}(\pi/8h) \approx 19.7^\circ$ matches well with the simulation result, confirming the effectiveness of our substructured metasurface even with less discretized units having larger phase steps. We also designed a flat focal lens with a phase profile

$$\varphi(y) = k_0(\sqrt{f_l^2 + y^2} - f_l), \quad (4.12)$$

where f_l is the focal length (in this case, f_l is set to 0.15 m) as shown in Fig. 4.16(c). As shown in the lower part of the figure, the discretized $\pi/6$ steps of the unit cells are utilized to form a hyperbolic profile as accurately as possible. The theoretical focal spot indicated by the black arrows match well with the intensified field in the simulation. Overall, it can be clearly seen that the designed beam profiles are successfully realized due to the highly transmissive unit cells. Especially, with respect to the focal lens shown in Fig. 4.16(c), the fields within the focal regions (presented in white) exceed the range of the color bar, meaning that the impinging wave was successfully concentrated.

The robustness of this metasurface can also be proved by performing oblique

incident simulations as shown in Fig. 4.17. Also, the mode conversion phenomena, which is a peculiar characteristic in the elastic wave regime, will be discussed. In the upper region, the divergence fields ($\nabla \cdot \mathbf{u}$) representing the longitudinal component are presented. In the lower region, the curl fields ($\nabla \times \mathbf{u}$) representing the shear component are shown for all cases. The angles of the transmitted waves (θ_t^L : longitudinal wave, θ_t^S : shear wave) are also presented with the simulations for both the divergence and curl plots. The superscripts L and S corresponds to the longitudinal and shear waves, respectively. The transmitted arrows are drawn by the theoretical angles calculated from the generalized Snell's law, which match excellently with the simulations. One can notice that no shear wave coming from the sources is observable because only longitudinal components were actuated. Instead, on the transmitted field, shear wave components with certain angles are observed. Such phenomena can be explained with elastic mode conversion at dissimilar boundaries, which follows the refraction rule $\frac{\sin \theta_t^L}{\sin \theta_t^S} = \frac{c_L}{c_S}$ (c : wave speed). In other words, shear waves are generated due to the “obliquely transmitted” longitudinal waves.

In addition, the ratios of the longitudinal and shear wave components are analyzed in Fig. 4.18. For simplicity, we only consider the wave impinging perpendicularly to the metasurface as shown in Fig. 4.18(a). From the power conservation theory, the following equation can be evaluated to observe the relations between the amplitudes and the transmitted angles

$$\frac{A_1^2}{c_L} = \frac{A_2^2}{c_L} \cos \theta_i^L + \frac{B_2^2}{c_S} \cos \theta_i^S, \quad (4.13)$$

where A_1 , A_2 and B_2 are the amplitudes of the input longitudinal wave, transmitted longitudinal wave, and the transmitted shear wave, respectively. The corresponding power and amplitude graphs are shown in the right side of Fig. 4.18(a). From the equation, it can be clearly inferred that as the refracted angle increases, the amplitude of the transmitted shear wave also increases while the amplitude of the transmitted longitudinal wave stays unity due to total transmission condition. To confirm the theoretical analysis, simulations of various transmitted angles are presented in Fig. 4.18(b). The results show good accordance with the theoretical results by depicting increased shear amplitudes as the refracted angles become larger.

4.6 Experimental Validation

To validate the beam controlling capability of the designed metasurface experimentally, we fabricated the metasurface structure ($360 \text{ mm} \times 24 \text{ mm} \times 0.5 \text{ mm}$) in the middle of the base aluminum plate ($800 \text{ mm} \times 600 \text{ mm} \times 0.5 \text{ mm}$) by laser precision cutting, as shown in the right side of Fig. 4.19(a). The minimal radius of the laser point used in the cutting process is $20 \text{ }\mu\text{m}$. This value ensures fine resolution for precisely cutting even the minimal dimension within the unit cell, which is $100 \text{ }\mu\text{m}$ as shown in the magnified unit cell image. In addition, it should be noted that a very thin plate (0.5 mm in thickness) is employed to comply with

the plane-stress condition, which is applied throughout this work. Accordingly, the lowest symmetric Lamb wave (S_0), which is a good approximation [36, 39] for in-plane longitudinal wave in thin plates, is implemented for the experiment.

The experimental set-up for visualizing the wave propagation is shown in Fig. 4.19(b). The host plate is fixed along a metallic wall by using magnet blocks. Specifically, four magnets are placed between the plate and the wall near the four corners, and additional magnets are attached on the other side of the plate to fix itself along the wall. In this way, we can realize the traction-free as well as plane-stress condition by freeing the plate from the wall. It should be noted that the magnet blocks are placed far enough from the source transducer to avoid undesirable interference on the magnetostriction phenomenon of the employed transducer.

On the other hand, to experimentally realize the widely-uniform S_0 wave, as employed in the simulation in Fig. 4.16, we implemented a giant MPT, as shown in Fig. 4.19(b). This lab-made ultrasonic transducer consists of permanent magnets, a solenoid copper coil array, and an acrylic housing to configure the components in their positions. Most importantly, a magnetostrictive material (here, we utilize a nickel patch of dimension: $300 \text{ mm} \times 25 \text{ mm} \times 0.1 \text{ mm}$) must be bonded onto the plate to induce strain, which is responsible for the elastic wave generation. In this work, we utilize a shear couplant to couple the patch with the plate. When the giant MPT is installed onto the plate, the dynamic magnetic field induced into the coil of the MPT generates a strain in the patch, which in turn induces a strain in the plate.

In this particular structural assembly, our MPT predominantly generates the longitudinal mode due to the orthogonally arranged copper coil array and static magnetic field [106]. Additionally, the MPT was tuned to our target frequency (100 kHz) by setting the interval to half wavelength. In a thin plate, this induces the lowest-symmetric Lamb (S_0) mode, as explained above. For more information on the detailed working principles of such MPTs, see Refs [66, 103, 106].

The source signal for the experiment was initially generated using a function generator (Agilent 33220A), then amplified by a power amplifier (AE TECHRON 7224), and then sent to the MPT. As for the input signal, a Gabor pulse (or modulated Gaussian pulse) of 100 kHz, which is shown in Fig. 4.19(b), was used to ensure adequate frequency localization. A digital oscilloscope was used to conveniently handle the source and received signals. The transmitted field is picked up by a laser scanning vibrometer (Polytec PSV-400), which is aimed perpendicular to the plate surface in order to scan the displacement fields. The received data were automatically averaged 800 times to remove unwanted signal noises. Additionally, a band-pass filter embedded in the laser vibrometer software was employed to eliminate unwanted frequency components.

As shown in Fig. 4.20, we scanned the transmitted regions, which are indicated by the purple squares in Figs. 4.16(a) and 4.16(c), for the refraction and focusing cases, respectively. The zoomed-in views at specific times (t) from the transient wave simulations are shown in Figs. 4.20(a) and (b), along with the coordinate information with respect to the x - y axes to specifically denote the region of interest.

We set the scanning region to be $0.2 \text{ m} \times 0.15 \text{ m}$ for the refraction case as shown in Fig. 4.20(a). The mesh grid was set to $14.3 \text{ mm} \times 15 \text{ mm}$ in order to divide the entire region into 15×11 points to ensure that the neighboring measurements are within the subwavelength scale. The sequential images with about $4 \text{ }\mu\text{s}$ of time interval match well with the simulation, which also reveal the actual propagation phenomenon in the region of interest.

On the other hand, for the focusing case, which is shown in Fig. 4.20(b), we plot the fields with a scale that is 1.75 times greater than that for the refraction case (shown in Fig. 4.20(a)) in order to properly display the enhanced amplitudes resulting from the concentration. For these two cases and the others throughout this work, the input power is fixed to 1 (in units of normalized divergence) for consistency. We utilized the same mesh dimension as in the former case; however, here 11×9 points were fit into the region of interest. The experimental results shown in Fig. 4.20(b) are also in good agreement with the simulation result. The numerical and experimental results, which match well with the theoretical prediction, demonstrate the excellent performance of the designed substructured metasurfaces in beam pattern manipulation.

Remarks on the experimental results

For the experimental results, the sequential images are captured from an imaging program embedded in the laser scanning vibrometer (Polytec PSV-400). In other words, no signal post-processing was performed and the propagating wave fields

are drawn from the raw data only. Although band-pass filter and averaging method were applied beforehand, we did not perform any signal processing with the raw data to observe the actual results in real environment. Therefore, unlike the results from simulations, the experimental results contain some noises from other frequency components due to high sensitivity of the laser vibrometer. Nevertheless, the results confirm that the beams are successfully refracted and focused by the subwavelength metasurface layers.

To thoroughly investigate the experimental results, we additionally analyzed the raw data. We performed Fast-Fourier-Transforms (FFT) to efficiently derive the frequency components. As can be seen in Fig. 4.21, the raw data (although containing other noise components) has predominantly 100 kHz component which was in fact the frequency at the input source.

4.7 Summary

We proposed, for the first time, a fully-transmissive elastic metasurface consisting of uniquely designed substructures that decouple the intrinsic relation of mass and stiffness within elastic medium. In this way, we realized the followings:

1. Delicate tuning of both transmission and phase shift, which had been impractical with normal materials.
2. A new substructuring design framework to fulfill any desired profiles, as to facilitate the manipulation of the transmitted wave within subwavelength scale.
3. An innovative elastic wave controlling system in a much more compact and

easily-fabricated form.

Our work provides the basic groundwork for designing a high-transmission elastic metasurface, which is ideal for longitudinal in-plane elastic waves. The design of the substructures also possesses low complexity and intuitive geometrical features, which enable convenient realization and fabrication of the elastic metasurface structure. Such innovative elastic wave control is expected to have great potential for various ultrasonic wave engineering applications including structural health monitoring and bio-medical imaging. In particular, the proposed elastic metasurface is expected to be highly compatible with conventional systems owing to its planar and slim geometry. Consequently, arbitrary steering and focusing of waves will be possible by just mounting our metasurface structures onto transducers. Therefore, our future research interest will focus on extending this work to the fabrication of 3-dimensional and practicable forms that can be integrated into actual inspection structures. This work is expected to pave the way for powerful methods to manipulate ultrasonic waves in much more compact and novel ways.

Table 4.1 Values of M_{al} , K_{al} , etc.

Mass	M_{al}^M	3.78×10^{-5} kg
	M_{al}^K	2.16×10^{-5} kg
	M_{al} ($M_{al} = M_{al}^M + 2M_{al}^M$)	8.1×10^{-5} kg
Stiffness	M_{al}^M	1.403×10^8 N/m
	M_{al}^M	2.455×10^8 N/m
	K_{al} ($\frac{1}{K_{al}} = \frac{1}{K_{al}^M} + \frac{2}{K_{al}^K}$)	6.546×10^8 N/m

※ The values were derived as below:

$M_{al} = \rho V = \rho \times d \times l \times t$, where V is the volume, ρ is density (here, 2700 kg/m^3 for aluminum), and t is thickness (here, 0.5 mm).

$K_{al} = \frac{C_{11}A}{d} = \frac{C_{11} \times l \times t}{d}$, where A is the cross-sectional area, C_{11} is x -directional component of the elastic stiffness tensor in plane-stress condition (here, 78.56GPa for aluminum).

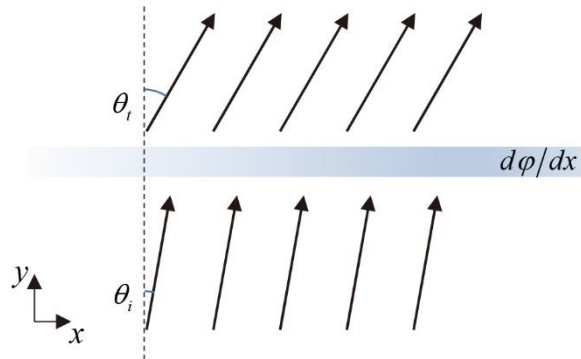
※ The K_{eff} -substructure is 0.16 mm wide and the M_{eff} -substructure is 0.28 mm wide.

Table 4.2 Structural parameters of chosen unit cells and their transmission/phase shift values

Unit cell #	Transmission (%)	Phase shift (deg)	l (mm)	w (mm)
1	98	359	3.9	0.6
2	99	30	3.65	0.51
-	98	47	3.5	0.5
3	94	60	3.45	0.5
4	96	94	3.15	0.49
5	95	122	2.75	0.48
-	96	134	2.6	0.48
6	97	153	2.45	0.48
7	99	179	2.15	0.48
8	100	209	1.65	0.48
-	99	225	1.3	0.48
9	100	239	0.9	0.48
10	99	270	0.35	0.49
11	98	300	0.2	0.56
-	98	314	2.8	0.468
12	92	333	2.75	0.468

-: the unit cell parameters belonging to the 45° steps.

(a)



(b)

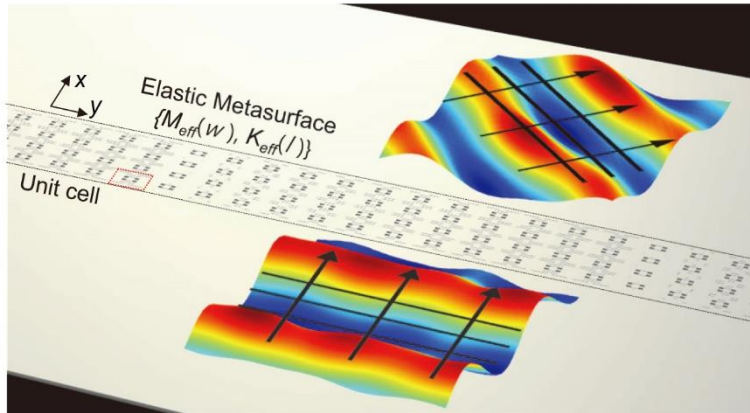


Fig. 4.1 (a) Schematic drawing of the Generalized Snell's law (b) Beam steering by the elastic metasurface composed of unit cells stacked together within a subwavelength layer.

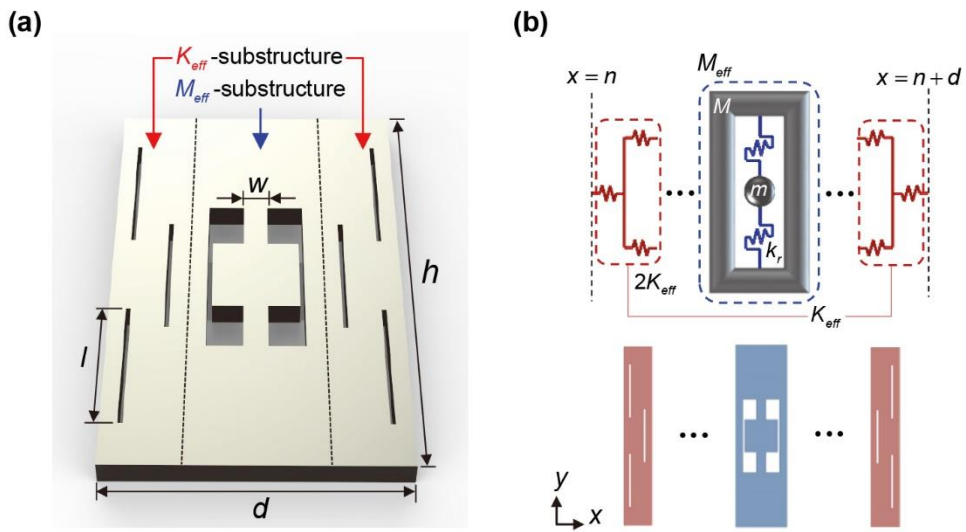


Fig. 4.2 Unit cell consisting of two independent substructures, the M_{eff} - and K_{eff} - substructures ($d=6$ mm, $h=10$ mm, thickness=0.5 mm, and l, w : design parameters). (c) Analytic mass-spring model of the unit cell composed of M_{eff} - and K_{eff} - substructures.

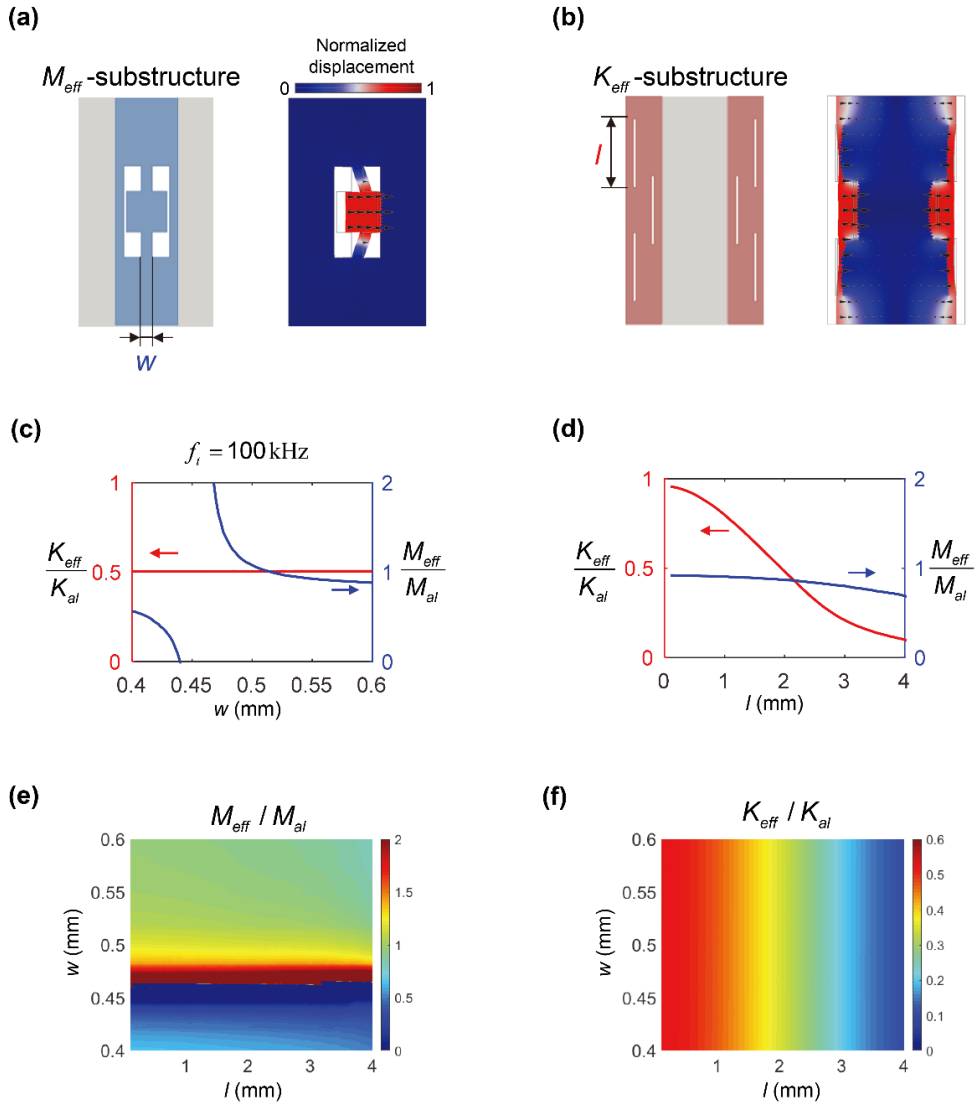
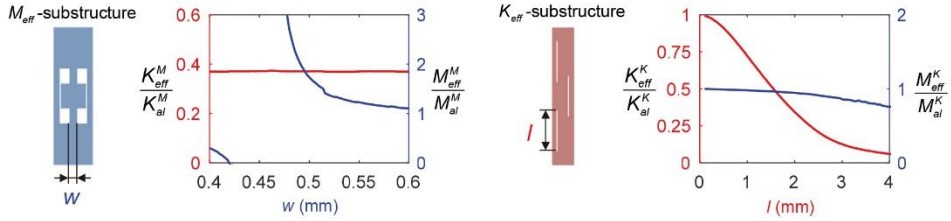


Fig. 4.3 Substructures for independent tuning of mass and stiffness. (a) M_{eff} - substructure and its eigenmode (dipolar mode) at 100 kHz. (b) K_{eff} -substructure and its eigen mode (softening mode) at 100 kHz. The black arrows within the eigenmode plots represent the vector magnitude of displacements. (c, d) Graphs of how effective parameters (M_{eff} and K_{eff}) change at the target frequency of 100 kHz depending on the two geometrical parameters w and l , respectively. (e,f) Contour plots of M_{eff} and K_{eff} , respectively, determined by the geometrical parameters w and l .

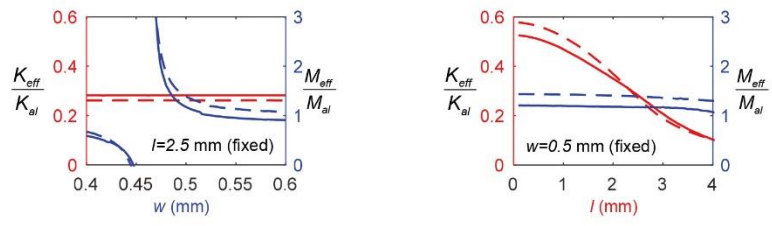
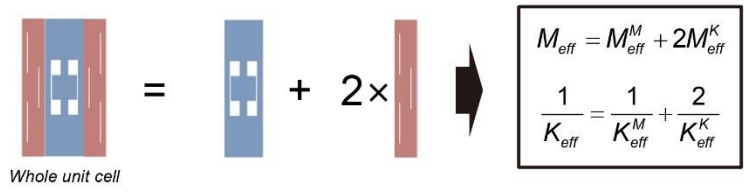
(a)

Numerically retrieved effective parameters for each substructure



(b)

Superposition of each substructure



----- (dashed lines): Superposition of discrete parts
 ——— (solid lines): Whole unit cell

Fig. 4.4 Superposition of retrieved parameters from discrete substructures. (a) Numerically retrieved effective parameters for discrete substructures. (b) Superposition of the retrieved parameters.

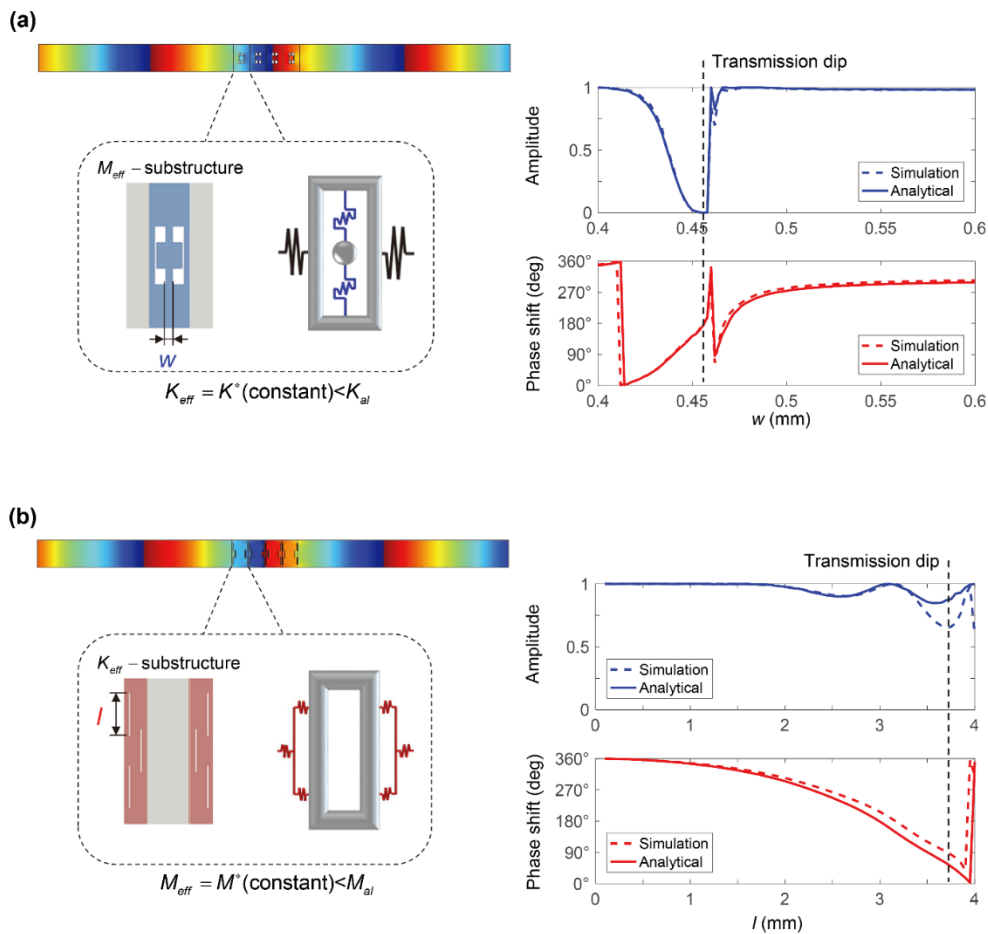


Fig. 4.5 Transmission and phase shift of metasurfaces consisting of each substructure only. (a) Simulation set-up with a metasurface composed of only the M_{eff} -substructures and its corresponding analytic mass-spring model. (b) Another metasurface unit is composed of only the K_{eff} -substructures while maintaining the periodicity by replacing the M_{eff} -substructure with an aluminum block.

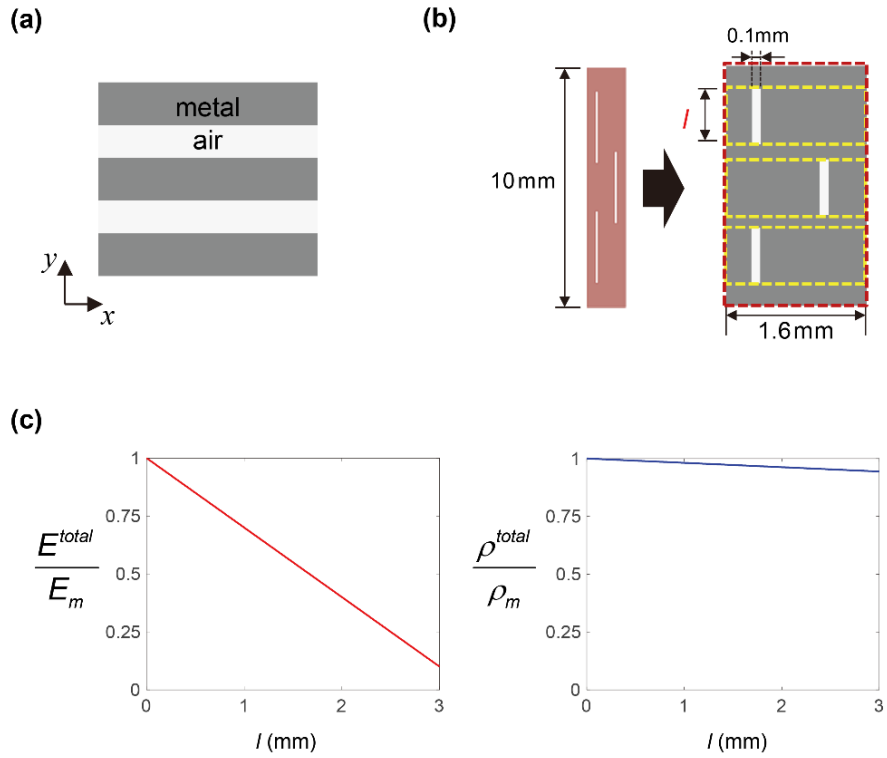


Fig. 4.6 Concept of rule of mixture applied to the substructure. (a) The layered composite consisting of metal and air. (b) The K_{eff} -substructure and its analogous model to be calculated as mixture of layered stacks. (c) The calculated stiffness and mass density properties with respect to l .

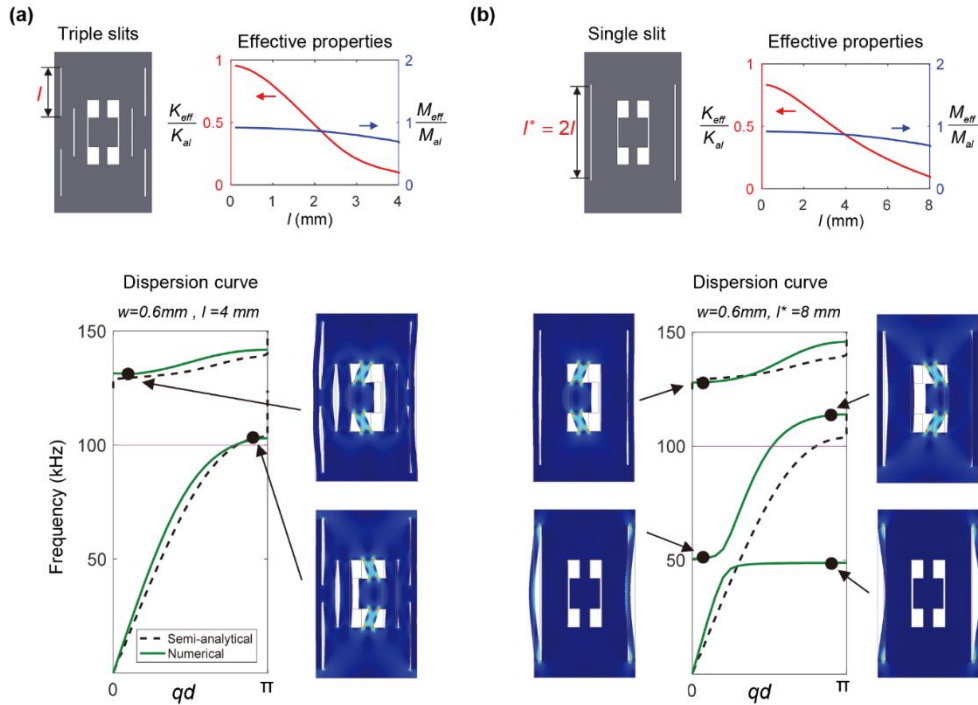


Fig. 4.7 Comparison of off-centered triple slits with single-slit unit cells. (a) The original unit cell having off-centered multiple slits and its effective properties plotted as functions of the slit length l . (b) A single-slit unit cell to be compared with the original unit cell in (a).

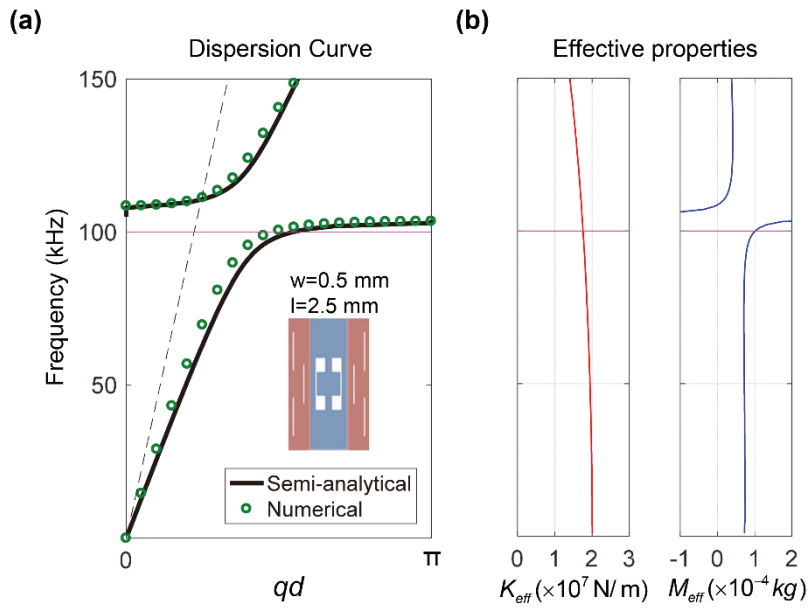


Fig. 4.8 (a) Dispersion curves of a substructured unit cell with $w=0.5$ mm and $l=2.5$ mm for its 1st Brillouin zone. (b) Numerically retrieved effective stiffness and mass for the unit cell. The magenta line denotes the target frequency of 100 kHz.

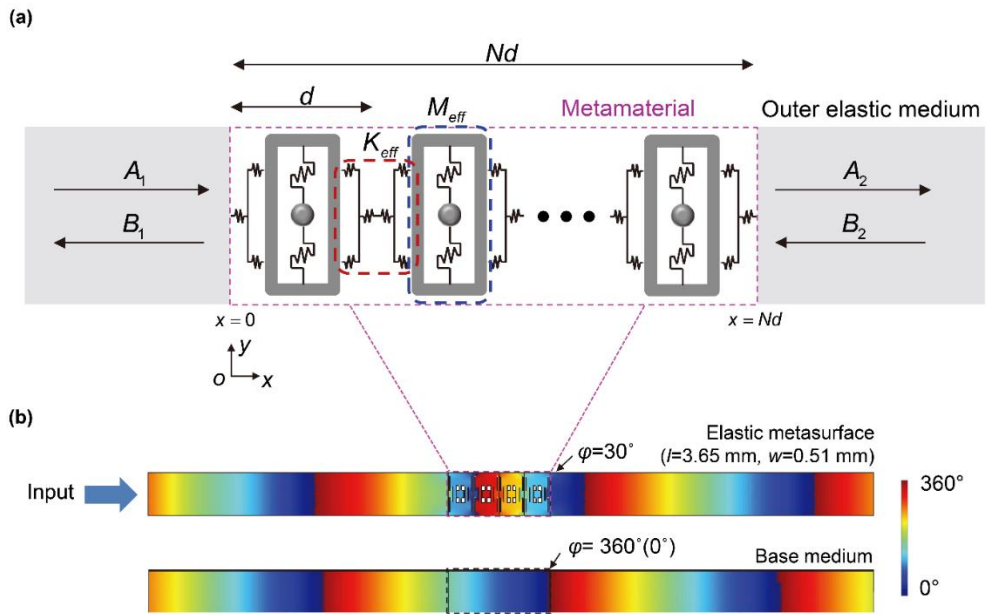


Fig. 4.9 (a) Discrete mass-spring model of unit cells within continuum outer elastic medium. (b) Corresponding numerical simulation with actual elastic metasurface structure embedded within continuum elastic medium.

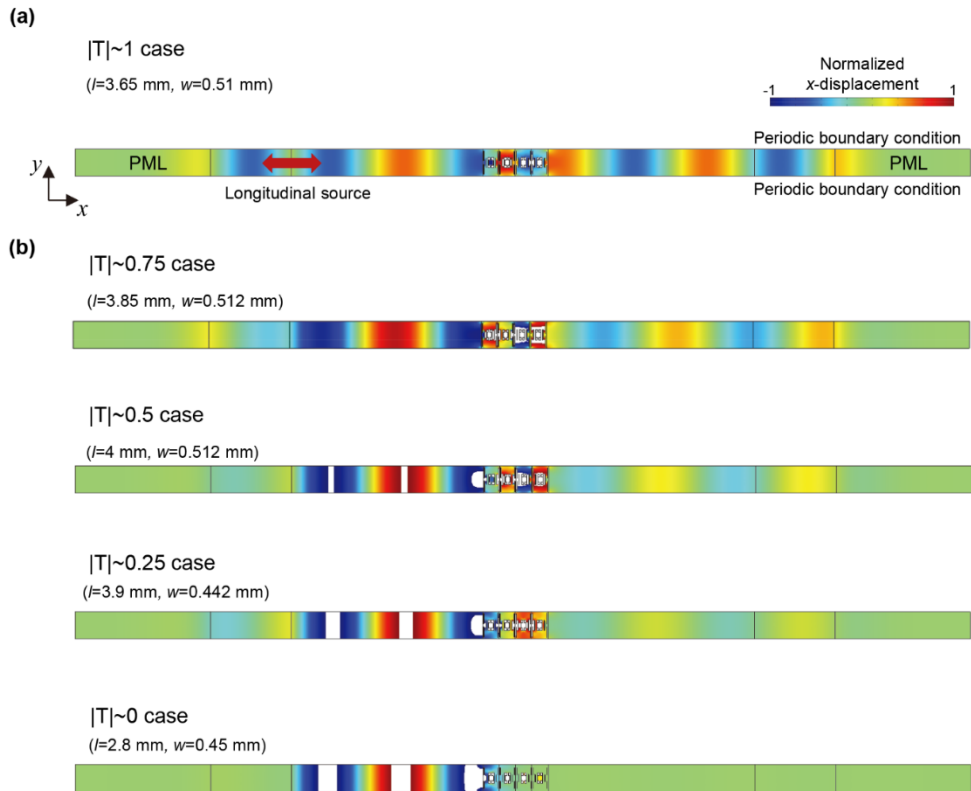


Fig. 4.10 The wave transmission plots for various geometric parameters with the specific simulation set-up. (a) The whole simulation set-up. (b) Various plots for the cases of transmissions less than unity.

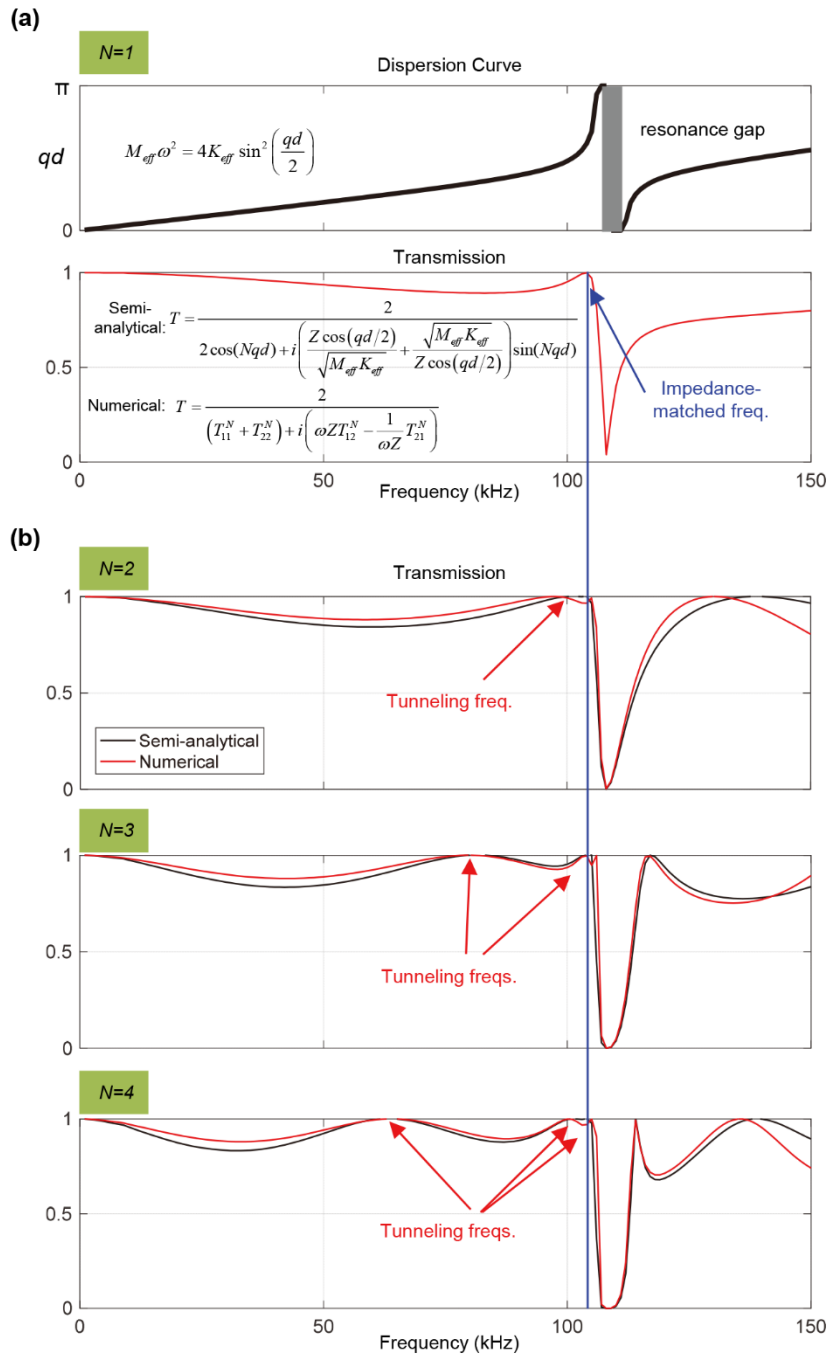


Fig. 4.11 Frequency-dependent transmission spectra estimation for (a) a single cell and (b) multiple cells.

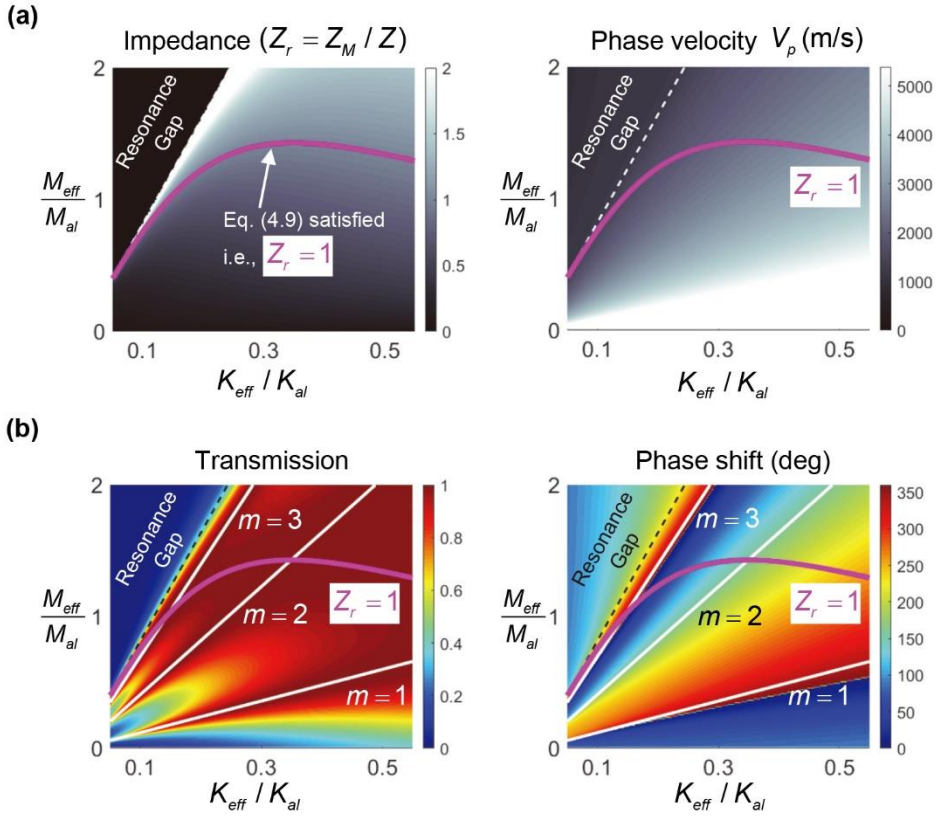


Fig. 4.12 (a) The contour plots of impedance ($Z_r = Z_M / Z$) and phase velocity (V_p) plotted on the $M_{eff} - K_{eff}$ plane. (b) The contour plots of transmission and phase shift plotted on the $M_{eff} - K_{eff}$ plane. In (b), the $Z_r=1$ line indicates the curve of matched impedance and the $m=1, 2$, and 3 lines indicate the satisfied tunneling condition. For (a,b), the analytic model was used for calculation.

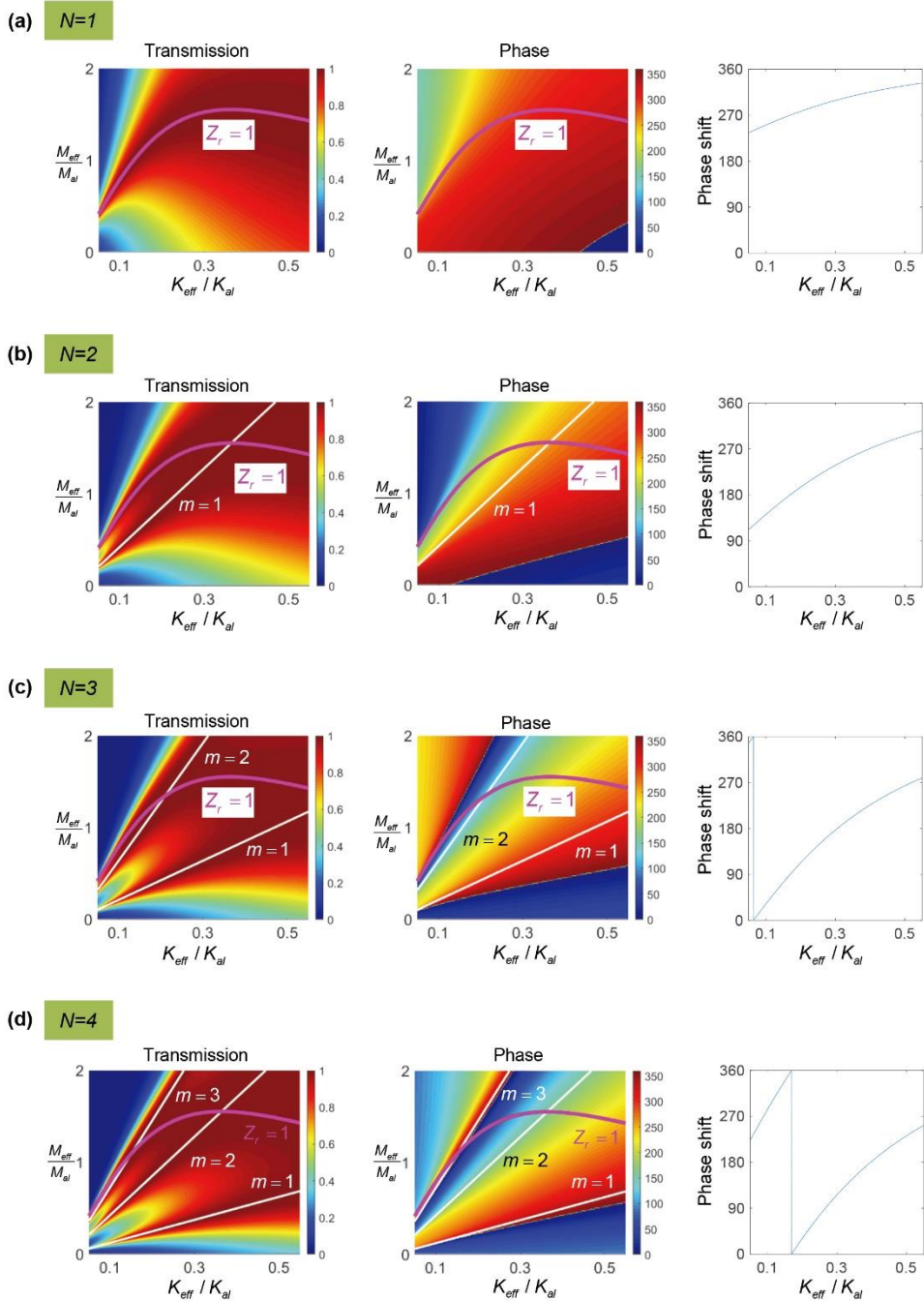


Fig. 4.13 Transmission/Phase spectra and the phase shift range along the impedance matching line for (a) $N=1$, (b) $N=2$, (c) $N=3$, and (d) $N=4$ case.

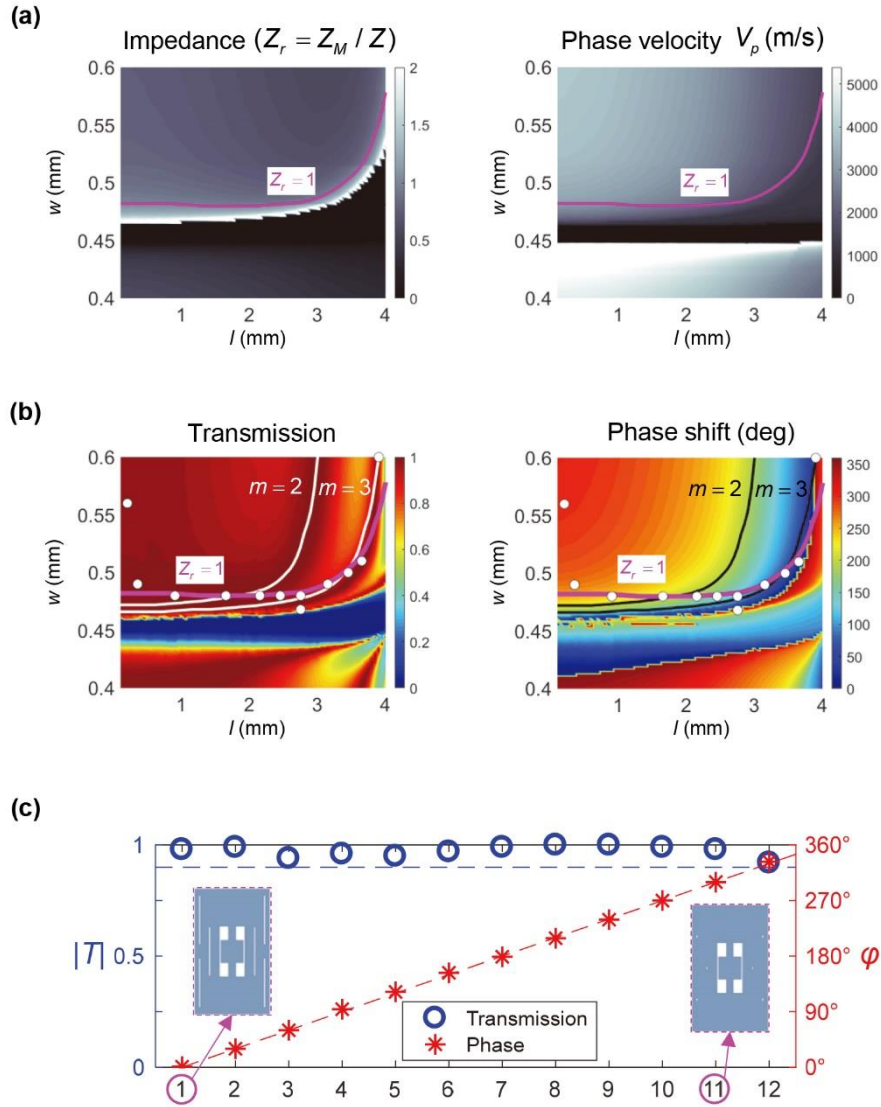


Fig. 4.14 Characteristics on functions of geometrical parameters from the simulation. (a) Semi-analytical values of relative impedance and phase velocity from effective parameters retrieved in Fig. 4.3(e-f). (b) Numerically calculated contour plots of transmission and phase on the l - w plane. The transmission and phase shift of the selected 12 unit cells exhibiting $\pi/6$ phase steps. The insets sketch the unit cells #1 and #11, which have extreme l values. (c) The phase simulation plots for odd-numbered unit cells corresponding to the phase shift of multiples of $\pi/3$.

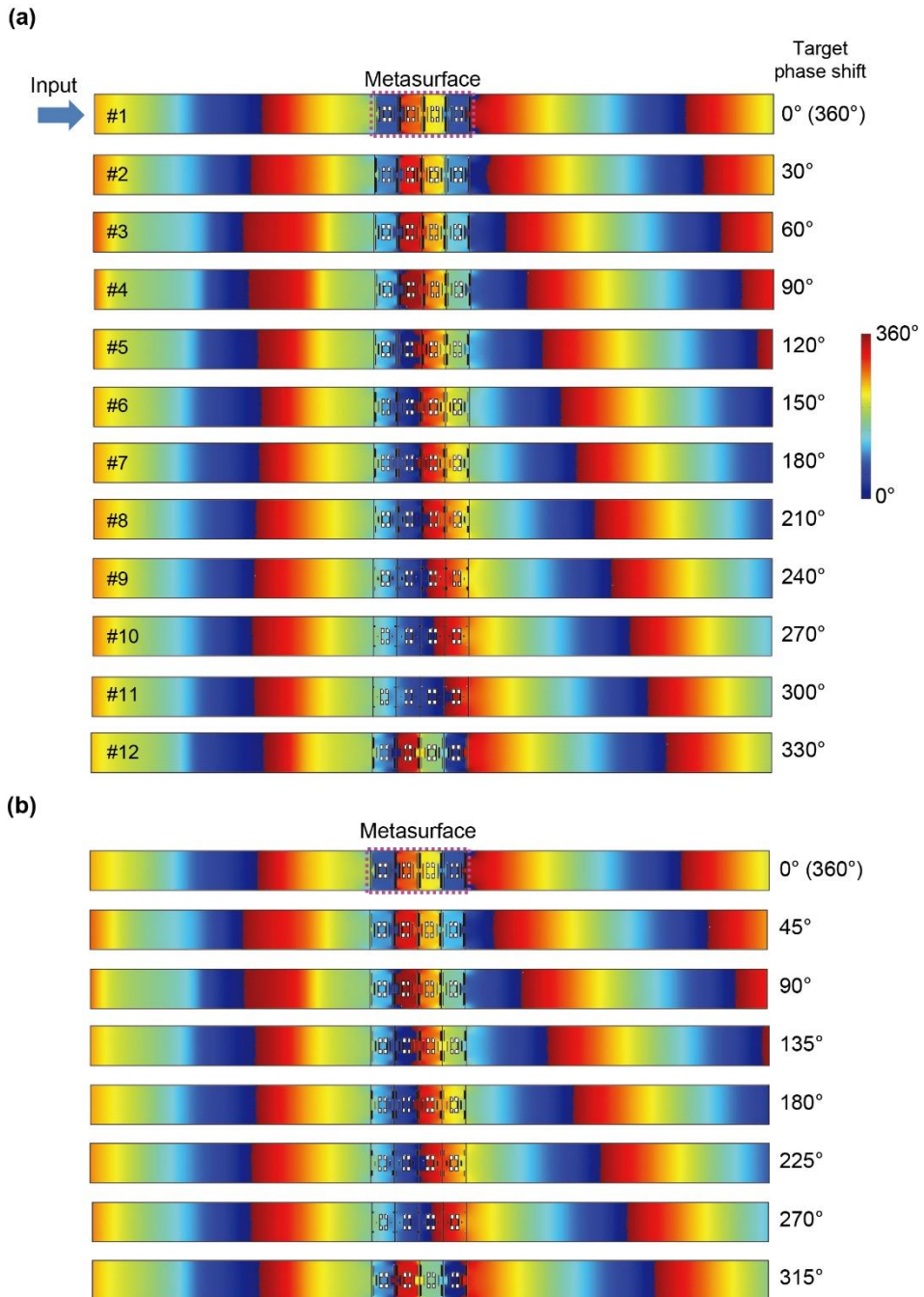


Fig. 4.15 The phase simulation plots for odd-numbered unit cells corresponding to the phase shift of multiples of (a) $\pi/3$ and (b) $\pi/4$.

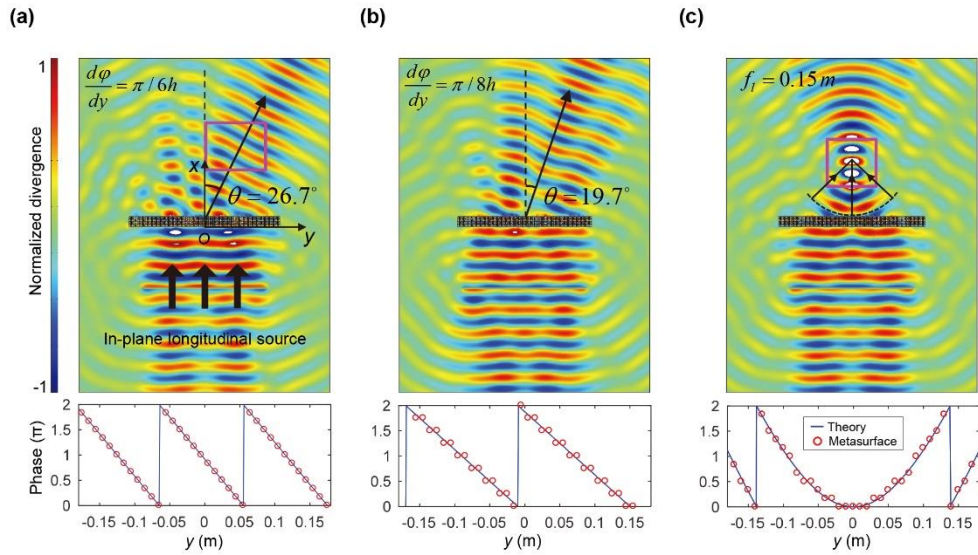


Fig. 4.16 Engineering longitudinal ultrasonic beam by elastic metasurface. (upper) The two-dimensional simulation of refraction with (a) $d\phi/dy = \pi/6h$, (b) $d\phi/dy = \pi/8h$, and (c) $f_l = 0.15m$ cases. The corresponding phase profiles are also shown below.

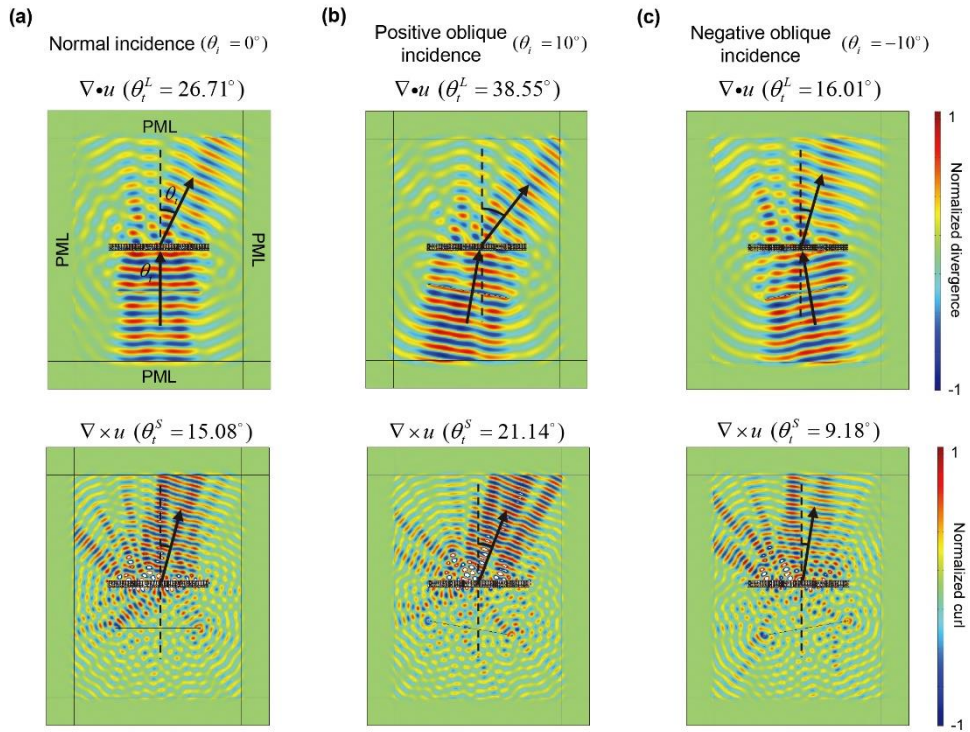


Fig. 4.17 Simulations for various incident angles of longitudinal sources where (a) $\theta_i=0^\circ$, (b) $\theta_i=10^\circ$, and (c) $\theta_i=-10^\circ$.

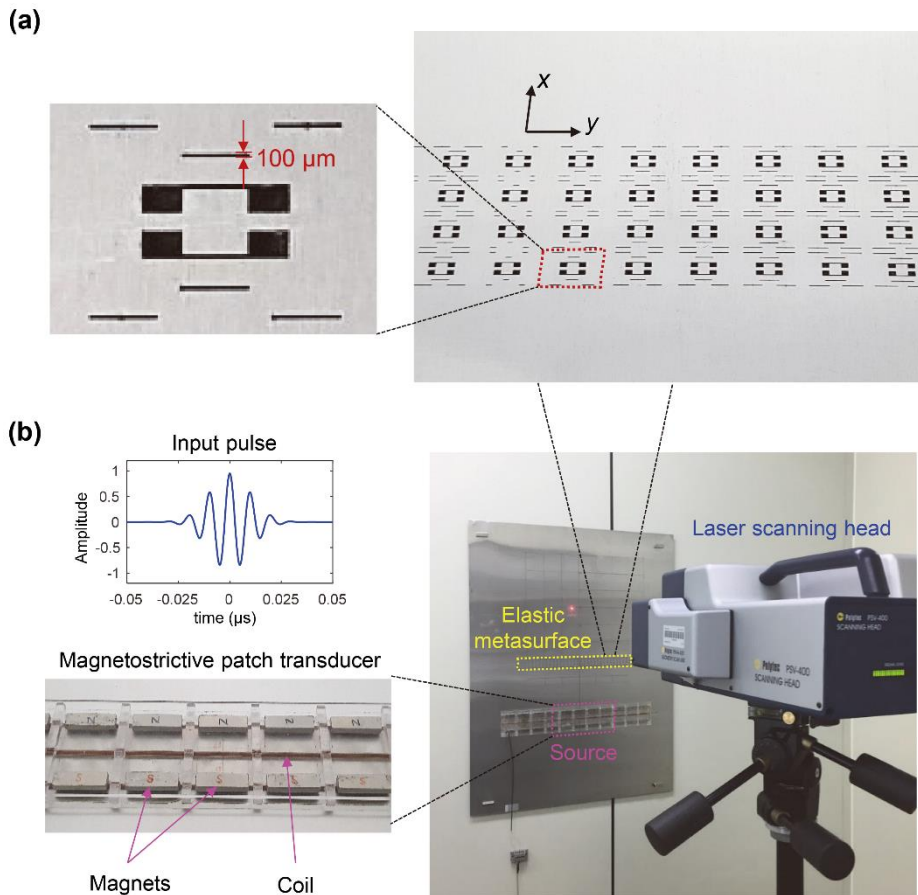


Fig. 4.19 Experimental set-up. (a) The fabricated elastic metasurface structure and the magnified image showing the details of a unit cell. (b) The experimental set-up with a giant magnetostrictive patch transducer (MPT) for generating ultrasonic 100 kHz S_0 wave. The measurement is carried out by the laser scanning vibrometer.

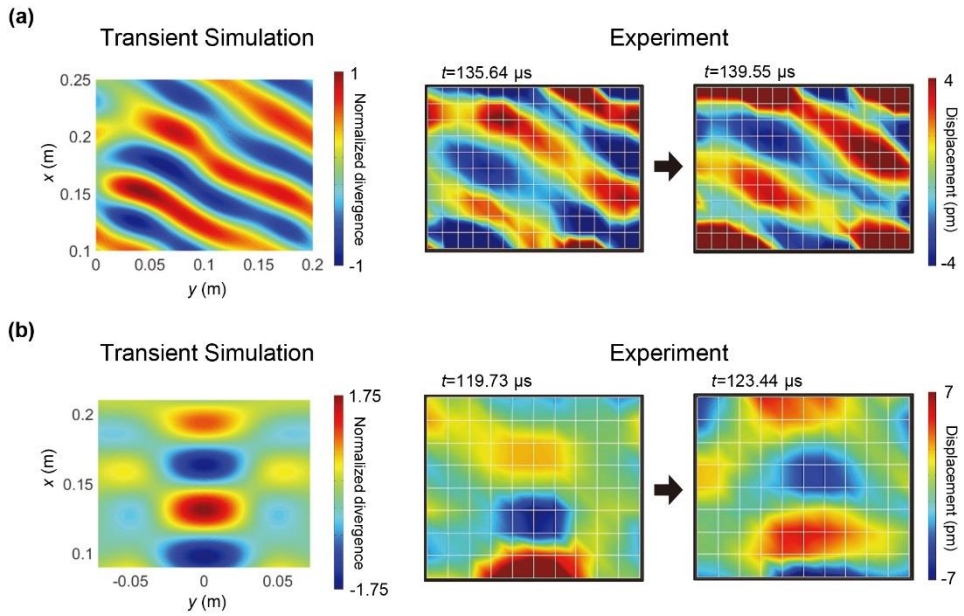


Fig. 4.20 Comparison of numerical and experimental results obtained for the rectangular regions marked in Figs. 4.17(a,c). Transient simulation results and experimentally retrieved sequential images for (a) the beam steering case considered in Fig. 4.17(a), and (b) the beam focusing case considered in Fig. 4.17(c).

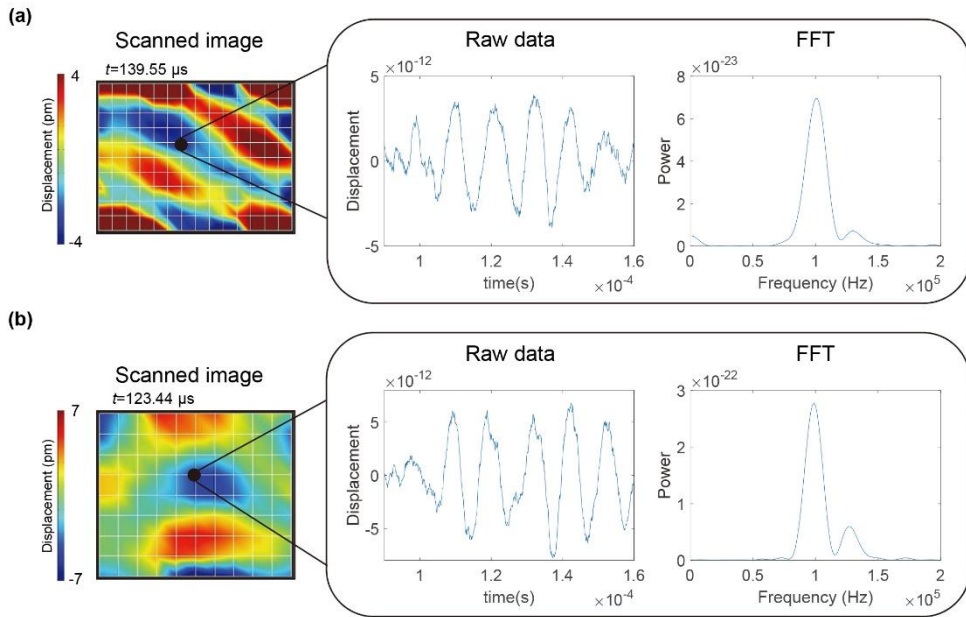


Fig. 4.21 Post-processing with the experimental results. (a) For the refraction case, the original signal is extracted at the point denoted with the black dot. Although the raw data contain minor peaks of noises, the dominant frequency (target frequency) component of the whole wavelet is 100 kHz. This is confirmed by Fast-Fourier-Transform (FFT) as shown in the figure. (b) The same procedure has been demonstrated for the focusing case.

<CHAPTER 5>

HYPERBOLIC ELASTIC METAMATERIAL LENS FOR TOTAL TRANSMISSION SUPER-RESOLUTION IMAGING

5.1 Chapter Overview

Pursuing fine quality subwavelength imaging of high transmission and low loss has been a critical issue for several decades. Since perfect lens [1] was proposed as a means to retain evanescent components, many researches on superlenses involving the anomalous negative refraction and amplification of evanescent waves have been reported [5, 107, 108]. Nevertheless, the performance of such methods were limited by transmission losses and inherent limitation of restoring only part of evanescent waves [109, 110]. As an alternative, anisotropic metamaterials with hyperbolic [19, 20, 111, 112] or eccentric elliptic equi-frequency contours that can support propagation of high wavevectors (evanescent components) have drawn much attention due to their capability to resolve subwavelength objects and design flexibility. Their equi-frequency contours that stretch out larger than that of a background medium make evanescent waves converted into propagating modes

inside the metamaterial and transferred to the other side of the lens, thus preserving subwavelength information. Subwavelength imaging with such metamaterial lenses for electromagnetic [21, 113-121], acoustic [18, 122], and elastic waves [102, 123] has been successfully demonstrated by highly anisotropic characteristics.

On the other hand, several studies to enhance the transmission through the lenses have been reported. Higher optical transmission was realized with the Fabry-Perot resonance mechanisms [17, 124, 125] and the radius-dependent permeability for an impedance-matched condition [22]. In the acoustic counterpart, the zero-mass effect has been implemented [126-128] to overcome the limitation arising from thickness resonance based lens [129, 130] which restricts the device's thickness to be chosen depending on the operating frequency. Specifically, clamped membranes installed along the slits make the Drude-form resonant state [131] to realize zero effective mass fulfilling impedance matching condition, thus ensuring complete transmission regardless of the lens's thickness. As such, material properties were delicately tuned to satisfy the conditions for total transmission.

Researches on elastic metamaterial lens for total transmission, however, have not been performed despite increasing demand for a broad range of applications including non-destructive evaluation and biomedical screening. The main reason is that in an elastic solid, unlike electromagnetic and acoustic metamaterials, coupling of shear, bending, and extensional motion makes it difficult to independently control and realize elastic constitutive parameters. Although recent research on elastic metamaterials with local resonances [35, 41, 42, 132, 133] paved a way for

achieving unique and anomalous effective properties, such methods still have not succeeded in realizing their specific parameters for continuum media. One of the convenient and efficient ways to fabricate such metamaterials may be to fabricate with a single medium by perforating air holes as recently demonstrated [39]. Nevertheless, this method inevitably decreases the mass density and stiffness of the metamaterial and eventually disturbs wave transmission due to highly mismatched impedance.

In this article, we propose and experimentally demonstrate total transmission subwavelength imaging with a hyperbolic elastic metamaterial lens. The key idea is to use extreme stiffness realized by the properly-designed unit cells of the metamaterial. It is composed only of a single elastic medium, aluminum with voids. The translational resonance of its local resonators induces an extreme stiffness value for waves propagating along the desired direction. So the extreme stiffness compensates for the decreased effective property (effective mass density), thus making total transmission possible. Although several works to independently control elastic stiffness in the specific direction have been reported [58, 65], extreme stiffness realization with continuum media evidenced by experimental demonstration has never been done. In addition to that, negative mass perpendicular to the desired wave propagation direction occurs simultaneously due to the same translational resonance, thus forming hyperbolic dispersion for subwavelength imaging. The theoretical explanations why such parameters are essential to achieve both the hyperbolic dispersion and impedance match condition

are given by using our explicit analysis of structural dynamics with an equivalent mass-spring model to simulate our continuum version. As for experimental verification, a slab-like lens composed of 21×10 unit cells is fabricated in a base plate. Two subwavelength longitudinal wave sources of 35.48 kHz are generated by magnetostrictive transducers [106, 134-136] which are proven to have good wave mode tunability. The transmitted wave at the imaging side of the lens is measured with a laser scanning vibrometer. The obtained results are in a good agreement with numerical simulation. Moreover, wave motions at the inside structures of the lens are measured as well to confirm its feasibility of directly transmitting the subwavelength details. The theoretical and experimental results clearly verify the feasibility for total transmission subwavelength imaging with elastic waves, and the results are expected to offer new design methodology for ultrasonic imaging applications.

5.2 Mechanics of Highly Anisotropic Unit Cell

Fig. 5.1 schematically shows the total transmission subwavelength imaging phenomenon with our elastic metamaterial lens. Two subwavelength incident waves (the source width, the distance between the sources, and the center-to-center distances are all of subwavelength scale) impinge perpendicularly in the y -direction on the lens, and the unbounded spectrum of spatial frequencies are transmitted to the other side of the lens to form subwavelength images without any loss. The key idea for the complete transmission of subwavelength images is based on satisfying

two essential requirements: total transmission condition in a wave propagation direction and a hyperbolically flat dispersion curve over a wide range of transverse wavevectors. At the selected target frequency of 35.48 kHz, we ensure that the parameters of the lens satisfy the following conditions:

$$M_{x,eff}^m < 0, K_{y,eff}^m \gg K_y^{al} \text{ and } Z_{y,eff}^m = Z_y^{al}. \quad (5.1)$$

In Eq. (5.1), the indices m and al stand for metamaterial and aluminum, respectively. The condition of $M_{x,eff}^m < 0$ in Eq. (5.1) means that the effective mass is negative in the x direction. Specifically, this single negativity (mass density) in the x direction makes a hyperbolic dispersion, similar to negative permittivity/permeability in optical counterparts [115]. In the y direction, extremely large stiffness compensates for decreased $M_{x,eff}^m$ from air perforation, thus fulfilling the impedance matching condition where impedance is $\sqrt{M_{y,eff}^m K_{y,eff}^m} \cos(q_y l / 2)$ from Eq. (3.33) (details will be discussed later). The extreme stiffness value is vital to total transmission regardless of the lens thickness. This intriguing parametric feature can be obtained with our uniquely designed unit cell shown in Fig. 5.2(a). Particular explanations will be made in the next subsection.

5.2.1 2-D mass-spring model

In this subsection, we present the 2-D mass-spring system to induce anisotropic mass and stiffness values in orthogonal directions. Here, because the resonators

will be shared for the properties in both axes, we analyze the effective parameters rather different from the one presented in Chapter 3. First, we deliberately define new unit cell boundaries to conveniently derive the effective properties. As a unit cell, we choose the mass-spring system enclosed in the red box shown in Fig. 5.2 (b). The mass M is considered to be connected with mass m . Therefore, one can model this system by an equivalent system consisting of effective mass and stiffness in x and y directions as suggested at the right side of Fig. 5.2(b). The horizontal and vertical displacements of mass M at the $(i,j)^{\text{th}}$ unit cell are denoted by $U_{i,j}$ and $V_{i,j}$, respectively. The mass M is connected to the mass in the adjacent unit cell by spring s , and local resonators by coupled springs as illustrated in the figure. The coefficients (α, β, γ) of the coupled spring can be defined as

$$\begin{bmatrix} F_x \\ F_y \end{bmatrix} = \begin{bmatrix} \alpha & \gamma \\ \gamma & \beta \end{bmatrix} \begin{bmatrix} u \\ v \end{bmatrix} \quad \text{or} \quad \begin{bmatrix} F_x \\ F_y \end{bmatrix} = \begin{bmatrix} \alpha & -\gamma \\ -\gamma & \beta \end{bmatrix} \begin{bmatrix} u \\ v \end{bmatrix}. \quad (5.2)$$

where F_i is the applied force in the i ($i=x,y$) direction and the displacement components of mass m in the x, y directions are denoted by u and v . Stiffness α represents shear stiffness while β , normal stiffness. The off-diagonal term γ is the coupling stiffness appearing due to the inclination of the elastic medium connecting M and m . The displacement variables of two resonator masses are denoted by $(u_{i,j}^l, v_{i,j}^l)$ and $(u_{i,j}^r, v_{i,j}^r)$.

5.2.2 Basic equation for simple mass-spring system with respect to

effective parameters

To evaluate the effective properties of the complicated system, it is worth to examine it in each principal direction. Furthermore, we will estimate the system analogous to the simple mass-spring system in each axis. Therefore, it is worth to review and re-write the simple dispersion relation in Eq. (2.4) with respect to the mass and stiffness terms. For example, we will consider the x -directional equation. The equilibrium equation of the (i,j) th mass in the x direction can be expressed in terms of the x -directional displacement $U_{i,j}$ as

$$M_{x,eff} \frac{\partial^2 U_{i,j}}{\partial t^2} = K_{x,eff} (U_{i+1,j} - U_{i,j}) - K_{x,eff} (U_{i-1,j} - U_{i,j}). \quad (5.3)$$

Assuming time harmonic wave motion at an angular frequency of ω , the displacement $U_{i,j}$ is re-written as $U_{i,j} \exp[i(\omega t - q_x d)]$. By using $\partial^2 U_{i,j} / \partial t^2 = -\omega^2 U_{i,j}$, $U_{i+1,j} = \exp(-iq_x d) U_{i,j}$, and $U_{i-1,j} = \exp(iq_x d) U_{i,j}$ the dispersion relation can be expressed as

$$-\omega^2 M_{x,eff} = K_{x,eff} (\exp(-iq_x d) + \exp(iq_x d) - 2). \quad (5.4)$$

This is the basic form of simple periodic mass-spring relation with respect to mass and stiffness properties and will be applied in the following subsections to derive the effective parameters.

5.2.3 x -directional parameters: resonant mass density

Let us first derive the parameters in the x direction. Because we consider only

longitudinal wave motion, the vertical displacements of M , $V_{i,j}$, will be omitted.

Also, from the symmetric condition, $v_{i,j}^l = v_{i,j}^r = 0$. Thus, the equations of motion

for the mass components in the (i,j) th cell become

$$M \frac{\partial^2 U_{i,j}}{\partial t^2} = s(U_{i+1,j} + U_{i-1,j} - 2U_{i,j}) + \alpha(u_{i,j}^l + u_{i,j}^r + u_{i,j+1}^l + u_{i,j+1}^r - 4U_{i,j}), \quad (5.5a)$$

$$m \frac{\partial^2 u_{i,j}^l}{\partial t^2} = \alpha(U_{i,j} + U_{i,j-1} - 2u_{i,j}^l), \quad (5.5b)$$

$$m \frac{\partial^2 u_{i,j}^r}{\partial t^2} = \alpha(U_{i,j} + U_{i,j-1} - 2u_{i,j}^r). \quad (5.5c)$$

For longitudinal motion in the x direction, the displacements can be assumed not to vary along the y direction. In this case, the following conditions are satisfied:

$$U_{i,j+1} = U_{i,j} = U_{i,j-1}, \quad (5.6a)$$

$$u_{i,j}^l = u_{i,j+1}^l, \quad (5.6b)$$

$$u_{i,j}^r = u_{i,j+1}^r. \quad (5.6c)$$

For steady state time-harmonic wave motion at an angular frequency of ω , and conditions (5.6a-c), Eqs. (5.5a) to (5.5c) reduce to

$$-\omega^2 M U_{i,j} = s(\exp(-ik_x d) + \exp(ik_x d) - 2)U_{i,j} + 2\alpha(u_{i,j}^l + u_{i,j}^r - 2U_{i,j}), \quad (5.7a)$$

$$-\omega^2 m u_{i,j}^l = 2\alpha(U_{i,j} - u_{i,j}^l), \quad (5.7b)$$

$$-\omega^2 m u_{i,j}^r = 2\alpha(U_{i,j} - u_{i,j}^r). \quad (5.7c)$$

Eqs. (5.7b) and (5.7c) can be re-written as

$$u_{i,j}^l = u_{i,j}^r = \frac{2\alpha}{2\alpha - \omega^2 m} U_{i,j}. \quad (5.8)$$

Substituting Eq. (5.8) into (5.7a) yields

$$-\omega^2 M U_{i,j} = s(\exp(-iq_x d) + \exp(iq_x d) - 2)U_{i,j} + \frac{4\alpha\omega^2 m}{2\alpha - \omega^2 m} U_{i,j}. \quad (5.9)$$

By re-writing this equation in the form of basic simple mass-spring dispersion relation, the following equation can be obtained

$$-\omega^2 \left(M + \frac{4\alpha m}{2\alpha - \omega^2 m} \right) = s(\exp(-iq_x d) + \exp(iq_x d) - 2). \quad (5.10)$$

Comparing this with Eq. (5.4), the effective parameters can be defined as

$$M_{x,eff}^m = M + \frac{4\alpha m}{2\alpha - \omega^2 m} = M + \frac{2\omega_0^2 m}{\omega_0^2 - \omega^2}, \quad (5.11a)$$

$$K_{x,eff}^m = s, \quad (5.11b)$$

where $\omega_0 = \sqrt{2\alpha / m}$ is the x -directional resonant frequency. Therefore, only the mass term becomes the function of ω whereas the effective stiffness is independent of ω .

5.2.4 y-directional parameters: resonant stiffness

As for the y direction, a similar approach will be made. Here, the only difference is that the x -directional motion of resonators is always coupled with the y -directional motion. Thus, the equations of motion for mass components in the $(i,j)^{\text{th}}$ cell can be written as follows:

$$M \frac{\partial^2 V_{i,j}}{\partial t^2} = \beta(v_{i,j}^l + v_{i,j}^r + v_{i,j+1}^l + v_{i,j+1}^r - 4V_{i,j}) + \gamma(u_{i,j}^l - u_{i,j}^r - u_{i,j+1}^l + u_{i,j+1}^r), \quad (5.12a)$$

$$m \frac{\partial^2 v_{i,j}^l}{\partial t^2} = \beta(V_{i,j} + V_{i,j-1} - 2v_{i,j}^l), \quad (5.12b)$$

$$m \frac{\partial^2 v_{i,j}^r}{\partial t^2} = \beta(V_{i,j} + V_{i,j-1} - 2v_{i,j}^r), \quad (5.12c)$$

$$m \frac{\partial^2 u_{i,j}^l}{\partial t^2} = \gamma V_{i,j} - \gamma V_{i,j-1} - 2\alpha u_{i,j}^l, \quad (5.12d)$$

$$m \frac{\partial^2 u_{i,j}^r}{\partial t^2} = -\gamma V_{i,j} + \gamma V_{i,j-1} - 2\alpha u_{i,j}^r. \quad (5.12e)$$

Assuming time-harmonic wave motion, $V_{i,j} \exp[i(\omega t - q_y d)]$ and

$V_{i,j-1} = \exp(iq_y d) V_{i,j}$, Eqs. (5.12a-e) become

$$-\omega^2 M V_{i,j} = -4\beta V_{i,j} + \beta(1 + \exp(-iq_y l))v_{i,j}^l + \beta(1 + \exp(-iq_y l))v_{i,j}^r + \gamma(1 - \exp(-iq_y l))u_{i,j}^l - \gamma(1 - \exp(-iq_y l))u_{i,j}^r, \quad (5.13a)$$

$$-\omega^2 m v_{i,j}^l = \beta(1 + \exp(iq_y l))V_{i,j} - 2\beta v_{i,j}^l, \quad (5.13b)$$

$$-\omega^2 m v_{i,j}^r = \beta(1 + \exp(iq_y l))V_{i,j} - 2\beta v_{i,j}^r, \quad (5.13c)$$

$$-\omega^2 m u_{i,j}^l = \gamma(1 - \exp(iq_y l))V_{i,j} - 2\alpha u_{i,j}^l, \quad (5.13d)$$

$$-\omega^2 m u_{i,j}^r = -\gamma(1 - \exp(iq_y l))V_{i,j} - 2\alpha u_{i,j}^r. \quad (5.13e)$$

Re-writing Eqs. (5.13a-e) with respect to $V_{i,j}$ yields

$$v_{i,j}^l = v_{i,j}^r = \frac{\beta(1 + \exp(iq_y l))}{2\beta - \omega^2 m} V_{i,j}, \quad (5.14a)$$

$$u_{i,j}^l = -u_{i,j}^r = \frac{\gamma(1 - \exp(iq_y l))}{2\alpha - \omega^2 m} V_{i,j}, \quad (5.14b)$$

By substituting Eqs. (5.14a-b) into Eq. (5.13a), the dispersion relation for the y direction can be obtained as

$$-\omega^2 \left(M + \frac{4\beta m}{2\beta - \omega^2 m} \right) = \left[\frac{2\beta^2}{2\beta - \omega^2 m} - \frac{2\gamma^2}{2\alpha - \omega^2 m} \right] (\exp(-iq_y l) + \exp(iq_y l) - 2). \quad (5.15)$$

Here, it must be noted that in contrast to the former case, not only the effective mass but also stiffness terms are functions of ω . As Eq. (5.15) shows, the y -directional resonance occurs mainly due to the β term. For the selected geometry ($d=14$ mm, $l=22$ mm) as shown in Fig. 5.3(a), the static values of the properties can be calculated with COMSOL Multiphysics as shown in Table. 5.1. As this is the case, $\beta \gg \alpha$ so that the y -directional resonance occurs at a much higher frequency than that for the x -directional resonance. Because α is related to shear modulus and, β to tension, β is usually much larger than α . However, in a special situation when the operating frequency is much lower than the y -directional resonant frequency $\omega'_0 = \sqrt{2\beta/m}$, one can assume that

$$2\beta - \omega^2 m \approx 2\beta. \quad (5.16)$$

If the assumption (5.16) is valid, Eq. (5.15) reduces to

$$-\omega^2 (M + 2m) = \left[\beta - \frac{2\gamma^2}{2\alpha - \omega^2 m} \right] (\exp(-iq_y l) + \exp(iq_y l) - 2). \quad (5.17)$$

Consequently, the effective mass and stiffness for the y direction become

$$M_{y,eff}^m = M + 2m, \quad (5.18a)$$

$$K_{y,eff}^m = \beta - \frac{2\gamma^2}{2\alpha - \omega^2 m} = \beta - \frac{2\gamma^2 / m}{\omega_o^2 - \omega^2}. \quad (5.18b)$$

5.2.5 Explanation for simultaneous monopolar/dipolar resonances

The two eigenmodes (in-phase and out-of-phase x -directional motions are represented with arrows in the red box) of the translational resonance by m and (α, β, γ) depicted in Fig. 5.3(b) play key roles in bringing about the aforementioned desired extreme values. In this particular case, it should be noted that out-of-phase motion is mainly responsible for the extreme stiffness value in the y -direction whereas in-phase motion is responsible for negative effective density in the x -direction. Let us start with verification for out-of-phase motion. Due to orthogonally coupled stiffness terms (by the inclination in the continuum unit cell), out-of-phase motion induces significant deformation in the y -direction, making an extreme stiffness value in the y -direction but merely affecting the effective density parameter as expressed above in Eqs. (5.18a-b). Specifically, the deformation of the unit cell induced by out-of-phase motion exerts a reaction force against the wave propagating motion in the y -direction, thus giving rise to an extreme stiffness value ($K_{y,eff}^m$). This amplified stiffness consequently compensates for the decreased impedance in the elastic metamaterial to realize total transmission, which will be explained concretely in the next section.

On the contrary, as for the case of in-phase motion, the translational motions of two resonators in the unit cell cancel out each other's effect on the deformation in the y -direction. However, mass density negativity occurs in the x -direction owing to the dipolar resonance motion of the system consisting of $2m$ and M . This phenomenon can be explained otherwise as masses exhibiting a negative total momentum.

In the next section, actual retrieval of the unit cell's properties by our transfer matrix method will be discussed.

5.3 Unit Cell Analysis Based on Transfer Matrix Method

To reveal the wave characteristics of the metamaterial, it is very useful to retrieve its effective parameters. The use of effective parameters for the characterization is reasonable because the size of the unit is approximately equal to 0.14λ in the y direction and 0.09λ in the x direction, thus satisfying the long wavelength metamaterial assumption [64]. In addition to the analytic explanation with the mass-spring model in the previous section, we will verify the effective properties by the numerical simulation in this section.

For such derivation, the transfer matrix models drawn in Figs. 5.3(c-d) will be implemented. As for the x -direction, the M_{eff} -substructure model will be applied.

The main reason is that as shown in Fig. 5.3(b), the eigenmode having influence on the x -directional motion is the in-phase oscillations of the two local resonators. Accordingly, dipolar resonance takes place so that the effective mass term

experiences the resonant state. Therefore, it will be assumed as the M_{eff} - substructure model for the effective parameter retrieval calculation in the x -direction.

On the other hand, the main peculiarity of this cell lies in the anisotropy in the principal axes. The shared both-sided local resonators have totally different affects for two orthogonal axes owing to the symmetrically inclined slender beams. Due to the different eigenmode at the same frequency as depicted in Fig. 5.3(b), the out-of-phase motion dominantly modifies wave properties in the y -direction. Specifically, this out-of-phase oscillation contributes to volume change, and thus can be regarded as monopolar resonance. Therefore, to retrieve the distinctive effective properties in the y -direction, the unit cell can be regarded as the K_{eff} - substructure in the y -direction.

5.3.1 Negative mass in the transverse direction: for hyperbolic dispersion

Numerical evaluation of the wave characteristics in the transverse (x -direction) is shown in Fig. 5.4(a). As was demonstrated in Chapter 3, Fig. 3.9(a), the dispersion relation, characteristic impedance, and the transmission curve are calculated. It can be observed that the resonance frequency is at about 33 kHz. Because it's the M_{eff} -substructure, the resonance gap exists including the resonant frequency. Thus, the wave propagation is forbidden in the x -direction at our target frequency, which is

about 35 kHz. The aspect of the relative impedance and the transmission curve additionally implies that the unit cell behaves like the M_{eff} -substructure. The impedance dramatically soars up just below the resonant frequency and goes to zero value within the gap region. Accordingly, unit transmission peak appears at the impedance matching frequency and then suddenly drops to very low value along the gap region.

Therefore, we retrieve the effective parameters by the M_{eff} -substructure model as discussed before and the results are shown in Fig. 5.4(b). As expected, only the $M_{x,eff}^m$ term experiences the resonant state whereas the $K_{x,eff}^m$ term remains almost constant. As discussed above, the dipolar modeshape due to the two resonators are the main underlying mechanism for tuning only the mass term. Consequently, the wave is hindered to propagate in the transverse direction while it is allowed to propagate in the y -direction (will be discussed in the next subsection). Therefore, in two dimensional aspect, hyperbolic EFC can be obtained for super-resolution imaging (will be discussed in the next section).

5.3.2 Extreme stiffness in the propagating direction: for total transmission

As for the wave propagating direction (y -direction), the numerically calculated wave properties are presented in Fig. 5.5(a). In contrast to Fig. 5.4, only the range of 0 kHz~50 kHz is plotted because of unnecessary branches that appear in the

higher frequency for the y -directional dispersion curve. Here, it can be clearly observed that the resonance frequencies are the same for both evaluations (x - and y -directions). This complements the analytic estimation that the two resonators are shared, meaning that two different eigen-modes occur at the same resonant frequency. Also, the impedance and the transmission curve resemble the ones corresponding to the K_{eff} -substructure that were previously discussed in Chapter 3, Fig. 3.10(a). Here, it must be emphasized that the impedance matching condition (total transmission condition) is what we intend to employ for the total transmission superlensing phenomena.

In Fig. 5.5(b), the retrieved effective properties are presented. As estimated before, only the $K_{y,eff}^m$ term is involved in the resonant state while the $M_{y,eff}^m$ term remains relatively constant. Unlike other works regarding metamaterials, the extreme stiffness value just above the resonant frequency is what we facilitate for the total transmission phenomena. All these exotic results originate from our uniquely designed elastic unit cell with local resonators connected by inclined slender beams.

5.4 Physical Explanation on Super-Resolution Imaging by Hyperbolic Dispersion

The band structure of this unit cell is shown in Fig. 5.6(a). In the inset, the rectangular lattice array and the corresponding first Brillouin zone are illustrated.

The solid line dispersion curve is numerically calculated by finite element analysis with commercial software COMSOL Multiphysics. The circles (for the x -direction) and squares (for the y -direction) are obtained by substituting calculated effective material parameters from Figs. 5.4 and 5.5 into the following basic periodic mass-spring dispersion relation in Eq. (3.23). Dispersion curves retrieved from both methods show a very good agreement. Note that the ranges of the resonant bandgaps in the Γ -X and Γ -Y directions differ because they rely on different constitutive parameters. Specifically, only the stiffness term experiences a resonant state whereas the mass density term is almost constant in the Γ -Y (i.e., y) direction. Exactly the opposite phenomenon occurs in the Γ -X (i.e., x) direction. To realize total transmission in the y direction, we elaborately utilize the fact that the effective stiffness based resonant bandgap is formed below the resonant frequency ω_0 ($\omega_0 = 32$ kHz from the analytical method) whereas the effective mass density based bandgap is formed above the resonant frequency. Therefore, the target frequency for total transmission in the Γ -Y direction is chosen to be 35.48 kHz which is slightly higher than the resonant frequency ω_0 . In this case, a pass band exists only for the Γ -Y direction while no wave can propagate in the Γ -X direction because of the resonant bandgap.

In Fig. 5.6(b), we plot the equi-frequency color contours for a range of frequencies around 35.48 kHz. Hyperbolic and nearly flat EFCs whose widths are several times larger than that of background medium can be clearly seen. It is also observable

that such dispersion behavior is valid for a wide range of frequencies. Similar to the canalization mechanism [113-115, 118], we can expect our slab-like elastic metamaterial lens to work as a transmission device that allows transportation of high wavevector components from one side to the other. With its hyperbolic dispersion, it enables an unbounded range of wave numbers to be delivered across the lens, ensuring no loss of any imaging information. Their EFCs that stretch out larger than that of a background medium make evanescent waves converted into propagating modes inside the metamaterial and transferred to the other side of the lens, thus preserving subwavelength information.

In fact, although not shown here, unit cells with similar geometries with different parameters were found to possess the desired characteristics, meaning that the unit cell microstructure in Fig. 5.2(a) is not the only solution. Although a small discrepancy exists in wave characteristics between the continuum body and the discrete mass-spring model, the analysis based on the discrete model provides adequate guidelines to analyze and obtain the desired parameters.

5.5 1-D Total Transmission Condition due to Impedance Matching Condition

In this section, we will show how the total transmission can be realized by using the designed metamaterial lens at the target operating frequency. Fig. 5.5(a), displays how the relative impedance $Z_{y,eff}/Z$ varies as a function of frequency

along the Γ -Y direction. In the negative-stiffness bandgap region below the resonant frequency (ω_c), the relative impedance has non-real values, meaning that no energy propagation is possible in that frequency range. Just above the resonant frequency, the real part of the impedance increases significantly as a result of the stiffness resonant state. The anomalously increased extreme stiffness term can thus counterbalance the reduced effective property ($M_{y,eff}^m$) of the metamaterial lens. Slightly above the resonant frequency, the relative impedance is extremely large but it decreases as the frequency further increases. A perfectly-matched impedance ($Z_{y,eff}/Z = 1$) occurs at 35.48 kHz.

The one-dimensional transmission coefficient T for waves passing through a dissimilar medium can be formulated as

$$T = \frac{2}{2 \cos(Nq_y l) + i \left(\frac{Z}{Z_{y,eff}} + \frac{Z_{y,eff}}{Z} \right) \sin(Nq_y l)}, \quad (5.19)$$

where N is the number of the unit cells embedded in the aluminum medium. Therefore, Nl represents the total thickness of the metamaterial lens inserted in an aluminum medium.

Further verification of the total transmission is conducted with a continuum model and the simulation set-up is shown in Fig. 5.7. A periodic boundary condition is applied to upper and lower sides. Longitudinal plane waves incident along the x direction are excited by harmonic forces along the line source at the left side of the metamaterial layer. The transmitted wave profile is picked up at the right side.

PMLs are added at the left and right end sides to eliminate any reflected waves from boundaries.

The obtained transmission spectra based on Eq. (5.19) are also presented in the figure with a different number of unit cells (i.e., 1 and 10 unit cells). The transmission curve indicates that total transmission occurs at 35.48 kHz in the 10 unit cells case. The peak frequency makes good agreement with the impedance matching frequency for the single unit cell case. Other observations can be made on additional peaks that occur from the Fabry-Perot resonances. As the number of unit cells increases, or when the lens becomes thicker, additional peaks appear owing to more frequency values satisfying the Fabry-Perot resonance conditions $Nq_y l = n\pi$ (n is an integer). Correspondingly, more standing waves can be compressed within the thickness of the lens.

To better understand the total-transmission subwavelength-imaging mechanism, some analysis will be useful. When $Z_{y,eff}/Z=1$, condition (5.19) becomes $T = 1/[\cos(Nq_y l) + i \sin(Nq_y l)] = e^{-iNq_y l}$ and the magnitude of T becomes unity regardless of q_y . This implies that any propagating wave in the y -direction can undergo total transmission. In other words, the above transmission relation is valid over an unlimited range of high transverse wavenumber components, meaning that they all can be converted to propagating waves and be transferred with total transmission.

It should be remarked that as in the zero-mass effect in an acoustic regime, the

realized total transmission in the elastic regime does not involve the Fabry-Perot resonance which is inappropriate for pulse type ultrasonic inspection.

5.6 Numerical Simulations of Super-Resolution Imaging

To confirm the subwavelength resolution imaging capability of our lens, we perform numerical simulations. The set-up with commercial finite element software COMSOL Multiphysics 3.5a is shown in Fig. 5.8. Plane stress, which is appropriate for small thickness, and no damping conditions were considered for all the simulations.

Our elastic hyperbolic lens is composed of 21×10 unit cells so that the whole structure is 294 mm wide and 220 mm tall. PMLs are applied to entire boundaries to eliminate boundary-reflected waves (not depicted in Fig. 5.8 for brevity). As for incident subwavelength wave generation, a 20 mm wide line source (corresponding to 0.13λ) is considered. A time-harmonic force of 100 Pa in the y direction is applied at the source. It would be worthwhile noting that our lens is designed for in-plane longitudinal waves, and in this specific case with thin plate, the lowest symmetric Lamb wave mode (S_0) makes a good correspondence. Consequently, the line source mainly generates the S_0 wave in our simulations because S_0 has dominant displacement in the y direction. The color plot is presented in the absolute value of the y -directional normal stress, $|\sigma_{yy}|$. The phase velocity of the S_0 wave in this condition is 5438 m/s and the corresponding wavelength is 153.6 mm. (For more details on wave characteristics in the media that we consider, refer to

Table 5.2).

With the finite element simulation model, we will verify the subwavelength imaging by the designed metamaterial lens. Figs. 5.8(a) and (b), respectively, consider one-source and two-source cases. For each of the two cases considered, wave simulations with and without the metamaterial lens are carried out. The metamaterial lens is installed 5 mm apart from the source along the y direction. From Fig. 5.8(a), it is apparent that in contrast to the case without the metamaterial, the subwavelength details are preserved in the imaging domain when the metamaterial lens is installed as though the source is directly transferred through the lens. The simulation result shows that there is no loss in details for the distance of 10 unit cells (corresponding to 1.43λ).

In Fig. 5.8(b), two 2 mm-wide line sources with separation of 36 mm (corresponding to 0.23λ) and center-to-center separation of 56 mm (corresponding to 0.365λ), are installed 5mm in front of the lens. The two ultrasonic sources separated by a center-to-center distance of 4 lattice constants are clearly resolved after the source signals pass through the metamaterial; the detailed resolution profiles are shown in Fig. 5.12(b) with experimental results. Although better resolution can be achieved by narrowing the separation between sources, this setting is chosen for presenting fine quality imaging without side lobes. In fact, two sources as close as 1 lattice constant (14 mm or 0.09λ) was resolved under the definition of full-width at half maximum (FWHM) of the peak as shown in Fig. 5.9. In other words, the ultimate resolution is theoretically limited by the period of an

unit cell size and thus it can be enhanced with smaller periods [137].

To visualize wave propagation inside the lens, extended color plotting is provided in the right sides of Figs. 5.8(a) and (b). Only the regions of wave propagation in the metamaterial lens undergo extremely large deformations, resulting in appreciable stress levels in the regions. These results imply that the system is capable of restricting wave propagation in the x direction, which reflects its hyperbolic dispersion characteristics. Additional simulations with different lens thickness, or different unit cell numbers, are presented in Fig. 5.10.

5.7 Experimental Verification

We experimentally validate the subwavelength imaging phenomenon evidenced with simulation work. In particular, wave motion inside the metamaterial lens is measured. The metamaterial lens shown in Fig. 5.11(a) is fabricated in a 1 mm-thick-aluminum plate by a precision laser cutting system. The purpose of small thickness is to comply with the two-dimensional plane stress condition which was implemented for numerical analysis. The dimension of the whole plate is relatively large (2,400 mm \times 1,200 mm \times 1 mm) to disregard any unwanted reflected waves from its boundaries. The experimental set-up for subwavelength elastic wave imaging is shown in Fig. 5.11(b). The plate is vertically fixed and ultrasonic magnetostrictive transducers [106] are installed to generate subwavelength waves. The wave propagation is scanned with a laser scanning head (Polytec PSV-400)

that aims perpendicular to the plate surface.

For proper generation of in-phase S_0 waves, two magnetostrictive transducers [106, 134-136] are installed in front of the lens. The transducer consists of permanent magnets, a solenoid copper coil array, and a nickel patch that is mainly responsible for wave generation by its magnetostriction phenomenon. Owing to a proper structural assembly of coils and magnets of the employed transducers, they mainly generate the S_0 mode; dynamic magnetic field induced by the coils is set to be parallel to the static bias field by permanent magnets, causing longitudinal strain for nickel patch along the direction normal to the coils, thus predominantly generating S_0 waves. Specifically we utilize a figure-of-eight coil to gain good directivity of the magnetic field. (See [106, 134-136] for more details on the working mechanism of the magnetostrictive transducer.)

As shown in Fig. 5.11(b), the nickel patch of the transducer is directly installed on the plate with epoxy bonding, and then the transducer is carefully attached on top of the patch by positioning its coils above the patch. Here, the middle of the figure-of-eight coil is aligned with the nickel patch. For subwavelength sources, the nickel patches are chosen to be 5 mm long (in the y direction) and 20 mm wide (in the x -direction). These patches well mimic two line sources facing normally to the lens that are appropriate for evaluating the capability of subwavelength imaging. Some critical issue exists in that the length (here, 5 mm) of a nickel patch can affect the incident wave properties in some way. When normal strain is induced from magnetostriction, unwanted waves can be simultaneously produced along

transverse direction due to Poisson's ratio effect [135, 136]. Therefore the shorter the patch size, the less generation of the side waves. However, a tradeoff exists in that the shorter the patch is, the lower intensity power it can produce. We chose it to be 5 mm to minimize the side waves but to guarantee adequate power.

The source signal is emitted from a function generator (Agilent 33220A) and amplified by a low-frequency power amplifier (AE TECHRON 7224) and finally sent to the source transducer. As for two-source experiments, the generation of in-phase source signals is critical. To realize it with magnetostrictive transducers, equal electric current is supplied to each transducer by a serially-connected circuit configuration. To ensure good frequency localization for the sensitive resonant state, we utilize a 20-cycle modulated sine wave

$$\left[1 - \cos\left(\frac{2\pi f_i t}{20}\right) \right] \sin(2\pi f_i t), \quad (5.20)$$

where f_i is our target frequency 35.48 kHz. Although better frequency localization can be obtained with longer cycles, 20 cycles is chosen to avoid elongation of reflected waves from the plate boundaries.

The measurement is performed by a laser scanning vibrometer that scans the surface displacement fields. Here, it should be noted that a laser scanning vibrometer is more suitable for measuring out-of-plane displacements whereas the S_0 mode has larger in-plane displacements along its propagation direction. However, in-plane displacements of the S_0 mode can be detected without losing generality thanks to Poisson's ratio. In this case, one may wonder if anti-symmetric

Lamb waves may be dominantly measured instead of the symmetric S_0 Lamb wave by a vibrometer. Because the actuation frequency is so selected to ensure that the anti-symmetric Lamb wave in this frequency range is in the region of a stop band, its propagation through the metamaterial is forbidden.

Scanning at the output boundary has been conducted to elaborate on its subwavelength resolution ability. The measurements are made in the 100 mm-wide image line that corresponds to the red lines in Fig. 5.8(a). This line is 230 mm apart (in the y direction) from the sources, which is 5 mm apart from the output boundary when there is a metamaterial lens. The purpose of measuring close to the metamaterial is to acquire the wave signals before they rapidly decay in the non-metamaterial base aluminum plate. Regarding data processing, filtering only the desired frequency is necessary because the dispersion curve of the metamaterial is very sensitive to the resonant frequency and the input signal contains a certain range of frequency components. Also, the raw data contain unwanted frequency components and noise owing to high sensitivity of the laser scanning vibrometer. Thus, the arrival signals at the output boundary are post-processed by the Fast-Fourier Transform (FFT) method.

The experimental data extracted through FFT are compared with the simulation data in Fig. 5.12(a). Here, the acquired data from simulation are in the unit of z -directional normal strain because laser scanning vibrometer measures the displacements normal to the plate surface. The plotted results in Fig. 5.12(a) are normalized with respect to the input maximum value from FFT (strain for the

simulation plot). The experimentally measured displacement (as well as strain extracted from simulation) is widely distributed with a small magnitude in the case where there is no metamaterial lens, implying that the subwavelength information is lost in the far-field.

In addition, the experimental results are plotted by the Gaussian regression method to characterize the resolution [138]. To characterize the resolution by deriving the FWHM, triple summations (to consider the case of two-source imaging where two beam profiles and a sidelobe exist) of the Gaussian functions were utilized for regression

$$r(x) = a_1 \exp \left[-\left(\frac{x-b_1}{\sqrt{2c_1}} \right)^2 \right] + a_2 \exp \left[-\left(\frac{x-b_2}{\sqrt{2c_2}} \right)^2 \right] + a_3 \exp \left[-\left(\frac{x-b_3}{\sqrt{2c_3}} \right)^2 \right]. \quad (5.21)$$

The coefficients a , b , and c 's for each case ensure the curves to fit the data with the R^2 (coefficient of determination) value, the goodness of fit, to exceed 80%. The results from the simulation and experiment are in a good agreement. The resolution, by the definition of FWHM, for the one-source experiment is as fine as 26.34 mm or 0.17λ . The FWHM's for two-source experiment is 29.79 mm or 0.19λ and 27.42 mm or 0.17λ , respectively. Also, the result from two-source experiment shows that peak intensities with subwavelength distance of 56 mm or 0.365λ apart can be clearly resolved with the metamaterial lens. The unexpected wave measurement in the middle is attributed to side lobes that are inevitable in experimental setting – we noticed the same behavior with far-field measurement in a bare aluminum without metamaterial.

Because the realization of the subwavelength imaging has been confirmed by the discussions above, we will now analyze the obtained experimental results in terms of total transmission. The peak intensity of single-source case with the metamaterial lens is increased almost by 2.77 times compared to that without one (intensity 0.24 to 0.66). As for the two-source case, the peak intensity is enhanced by 2.09 and 1.93 times, respectively (intensity 0.36 to 0.75 and 0.7, respectively). It can be clearly seen that the transmitted waves are enhanced with the metamaterial lens compared to those without one. Actually, the exact transmission coefficient must be managed in a one-dimensional point of view. Because waves from two-dimensional line sources can be focused in some spot, measuring the exact transmission coefficient with line sources would not be possible. In fact, if measured closer to the lens, the normalized peak intensity exceeds the unity value. Thus, instead of comparing transmission in two-dimensional point of view, we analyzed it with plane wave assumption in the one-dimensional domain.

One may also question about the fact that the experimentally measured ones with metamaterial lens reach about 70% of the theoretical predictions. Besides inherent material damping, the use of line sources in the experiments not functioning as the ideal line sources in the simulation hinders the realization of the total transmission phenomena. The error can also be attributed to fabrication inaccuracy that can slightly change the resonance frequency, resulting in different effective properties.

On the other hand, an interesting and important experiment is to measure the actual propagation inside the metamaterial lens, considering that no wave measurement

through elastic metamaterial lens has been reported. So, additional scanning inside structures of the lens has been carried out as shown in Fig. 5.12(b). The boundaries of the unit cell structures are mainly measured and the mesh grid is as shown in Fig. 5.12(b). The outlines of the lens are also presented. Although the transducers cross the lens boundary, it doesn't affect the wave generation because the nickel patch (which is installed below the lens) is mainly responsible for transmitting strain to the plate. Therefore, the mesh grid is just above the transducers and stretches up to the output boundary.

In each measurement, iteratively updated signals were automatically averaged over 600 data acquisitions to remove unwanted noise components. Also, a high-pass filter in the laser vibrometer software was used to eliminate high frequency components. The trigger delay was set to 200 μs for experimental convenience. In other words, the source transducers emitted signals at 200 μs . The snapshots were taken from sequential animated images obtained from the laser vibrometer software. From figures in Fig. 5.12(b), one can clearly see that because the group velocity is very low inside the metamaterial lens, the wave propagates to the other side of the lens much slower than the S_0 wave in an isotropic aluminum plate. In contrast to the group velocity, phase velocity is increased in the metamaterial lens, resulting in elongated wavelength as well. One can observe the positive amplitudes (represented in red) of increased wavelength inside the structure at 518 μs . The details of wave properties for the background aluminum plate and metamaterial lens are presented in Table 5.2. In addition to that, Fig. 5.12(b) clearly shows that

the direct propagation of two distinct subwavelength S_0 waves without spreading.

5.8 Summary

A hyperbolic elastic metamaterial was proposed and experimented for total transmission subwavelength imaging by ultrasonic elastic waves. The unit cell of the metamaterial was elaborately designed to achieve the anomalous essential parameters (negative effective mass density and extreme stiffness). The feasibility of total transmission is confirmed by both numerical simulation and ultrasonic wave experiment. From the practical point of view, the planar geometry may simplify the mounting of lens on a specimen to be inspected. Regarding the broad range of applications including ultrasonic medical screening and non-destructive evaluation, we expect this research will open doors for advanced ultrasonic imaging techniques with higher performance and practicability.

We also expect that our elastic metamaterial lens will offer new insights for better quality high-resolution ultrasonic imaging, broaden the functionality of elastic metamaterial to ultrasonic imaging techniques, and provide new guidelines for various applications including nondestructive testing and biomedical imaging. As for elastic metamaterial regime, which has been broadly researched worldwide recently, our analytic method will pave a way for controlling the elastic constitutive parameters to design a proper elastic metamaterial structure. Furthermore, our method will simplify the fabrication of elastic metamaterial and thus enhance the practicality of anomalous wave phenomena to a wide range of applications

regarding ultrasonic wave based technology.

Table 5.1 The calculated values for mass and stiffness parts of the analytical mass-spring model from the continuum unit cell.

α	β	γ	M	m
1.87 GPa	12.69 GPa	3.41 GPa	2.53e-4 kg	7.89e-5 kg

※ The calculations were performed by the finite element method with COMSOL

Multiphysics 3.5a.

Table 5.2 Wave properties in the wave propagation direction (y direction) of the two media

Wave properties	1 mm-thick aluminum plate	Metamaterial lens
Group velocity (m/s)	5407	792
Phase velocity (m/s)	5438	8669
Wavelength (mm)	153.6	244.3

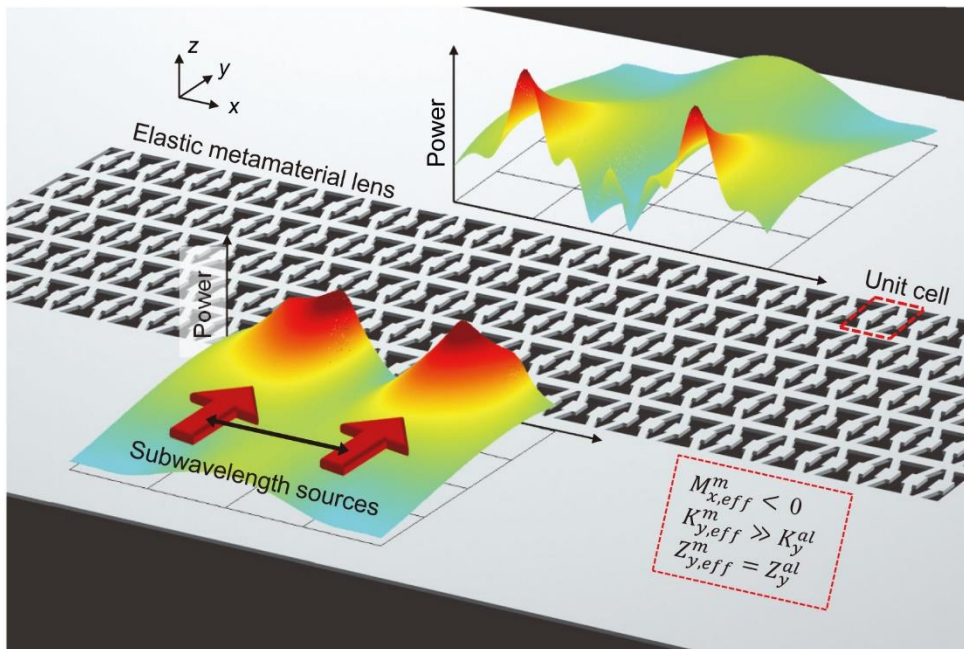


Fig. 5.1 Concept Schematic of total transmission subwavelength imaging with hyperbolic elastic metamaterial. The constitutive properties of its unit cell are presented in the box with red dashed lines.

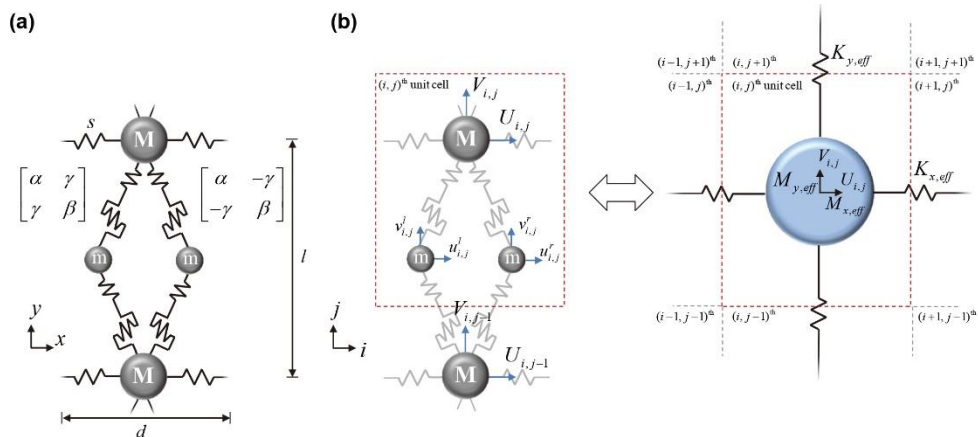


Fig. 5.2 (a) Mass-spring model of unit cell configuration. (b) Displacement notations and a set of masses to be considered as a new unit cell for deriving the parameters. Its effective mass and stiffness terms are equivalently represented in a simple mass-spring system in the right.

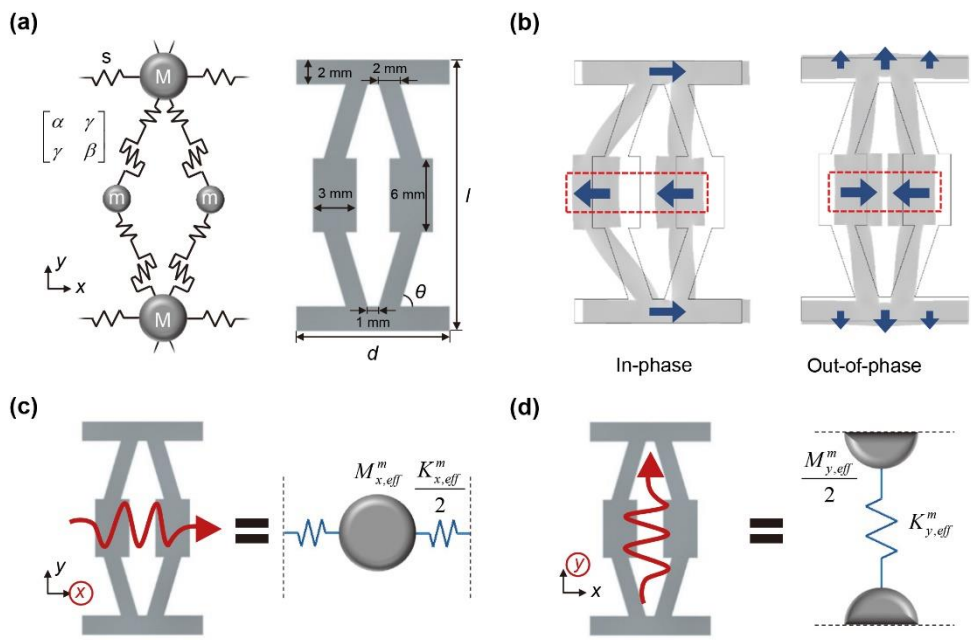


Fig. 5.3 (a) Analytical mass-spring model and its realization in continuum body. (b) The two translational resonance eigenmodes: in-phase (left) and out-of-phase (right). Lumped element transfer matrix model for the (c) x -direction and (d) y -direction

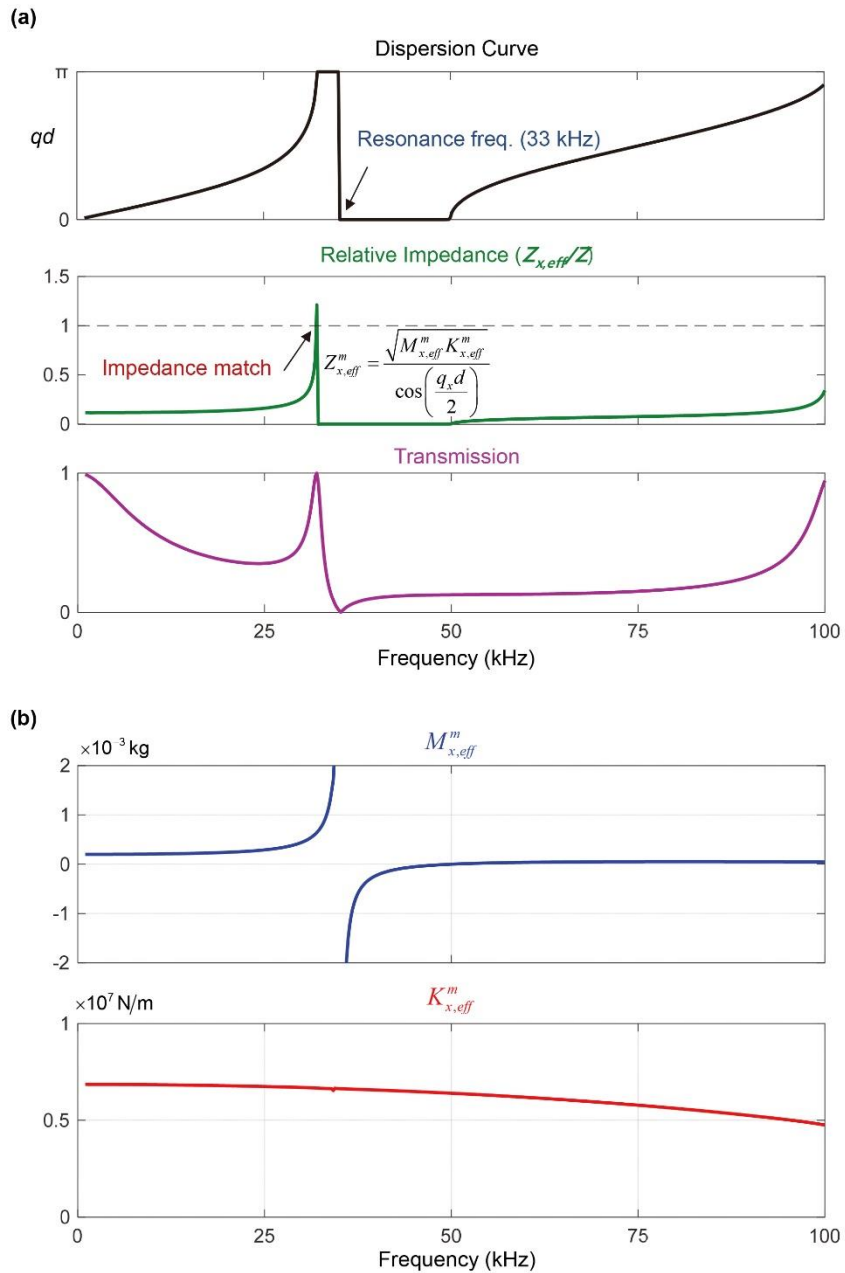


Fig. 5.4 Numerical analysis for the cell in the x -direction. (a) (From top to bottom) Dispersion curve, relative impedance, and transmission spectrum retrieved by the transfer matrix method. (b) Effective parameters retrieved by the transfer matrix method.

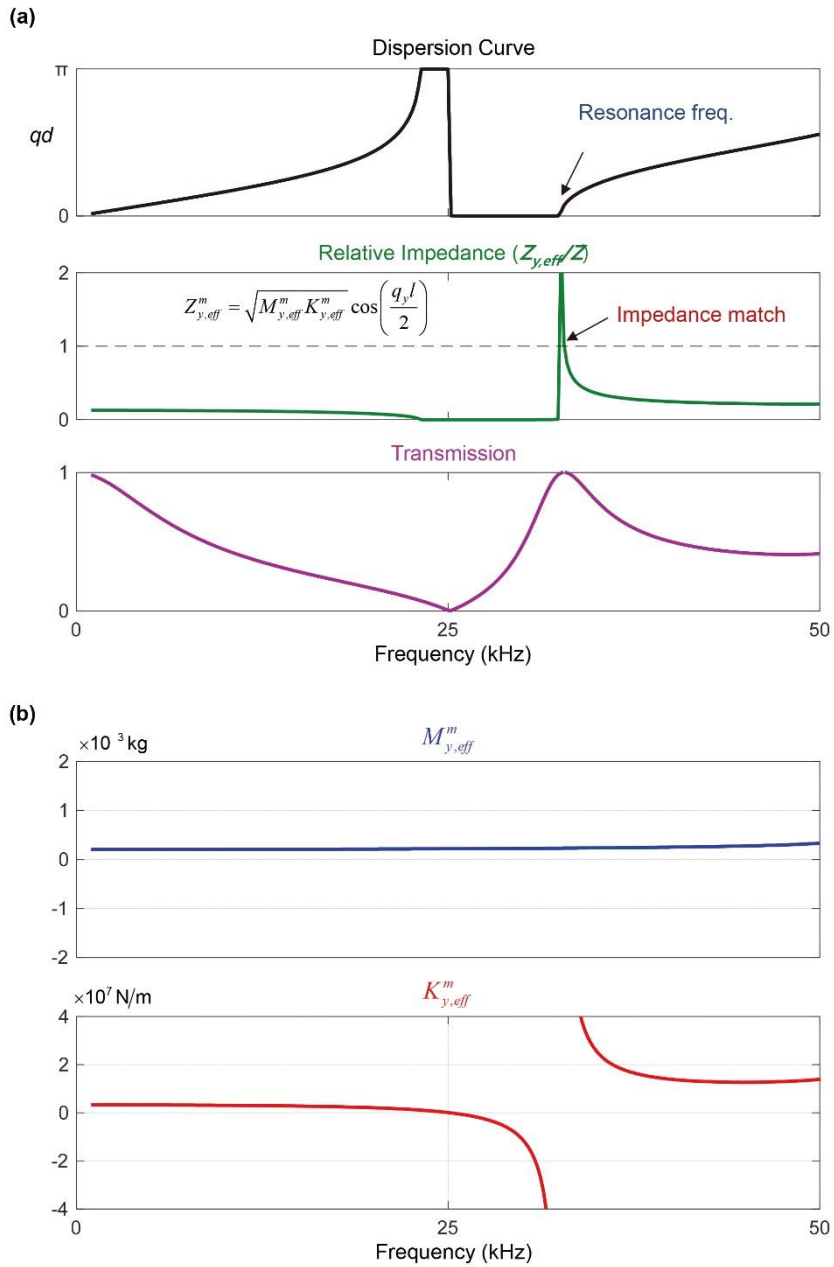


Fig. 5.5 Numerical analysis for the cell in the y -direction. (a) (From top to bottom) Dispersion curve, relative impedance, and transmission spectrum retrieved by the transfer matrix method. (b) Effective parameters retrieved by the transfer matrix method.

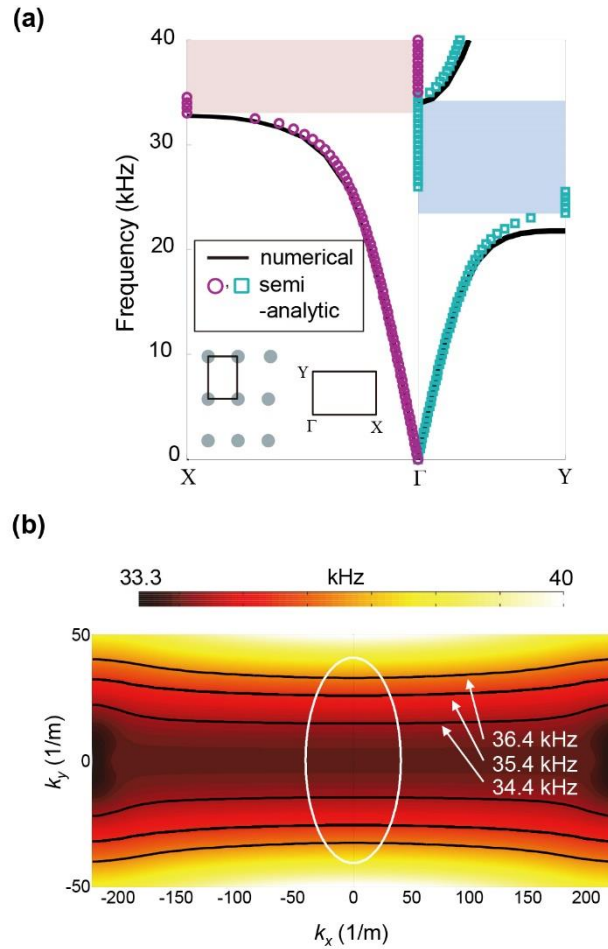


Fig. 5.6 (a) Dispersion curves for the Γ -X and Γ -Y directions. The mismatched resonant bandgap (shaded region) causes highly anisotropic properties. (b) Equi-frequency contours in a range of frequency. The white contour represents equi-frequency contour of the isotropic aluminum plate at 35.48 kHz.

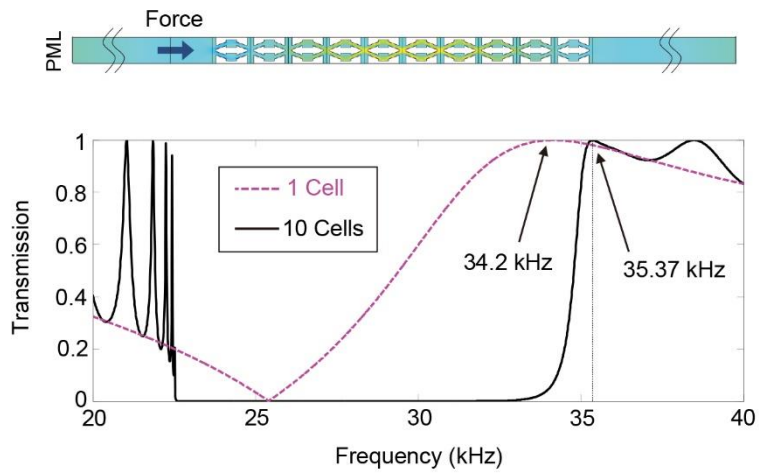


Fig. 5.7 Numerical set-up for transmission computation and transmission curve for different number of unit cells.

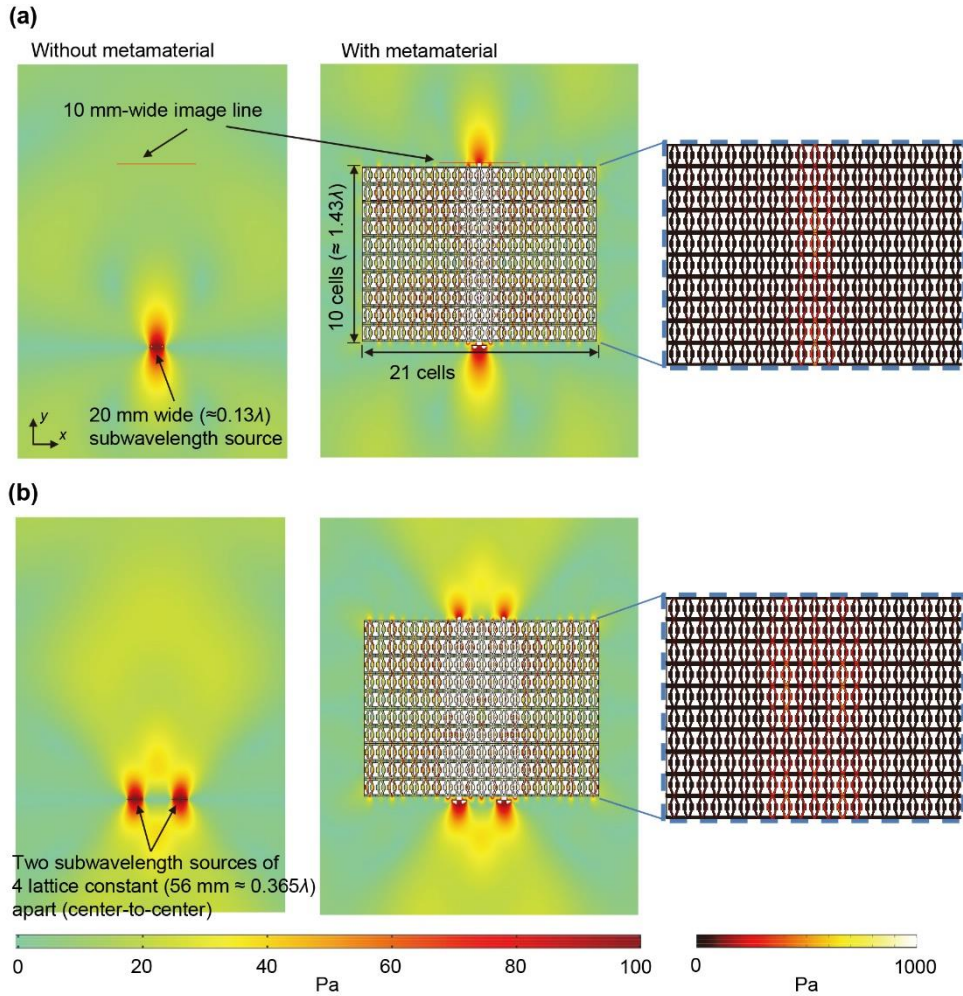


Fig. 5.8 (a) One-source simulation with a 20 mm-wide line source generating the S_0 wave. The zoomed plots inside the metamaterial propagation is also presented in the right side. (b) Two-source simulation with the same sources separated (center-to-center) by 56 mm is shown. The color plot is in unit of the absolute y -directional stress ($|\sigma_{yy}|$) where the input power is 100 Pa in the y direction.

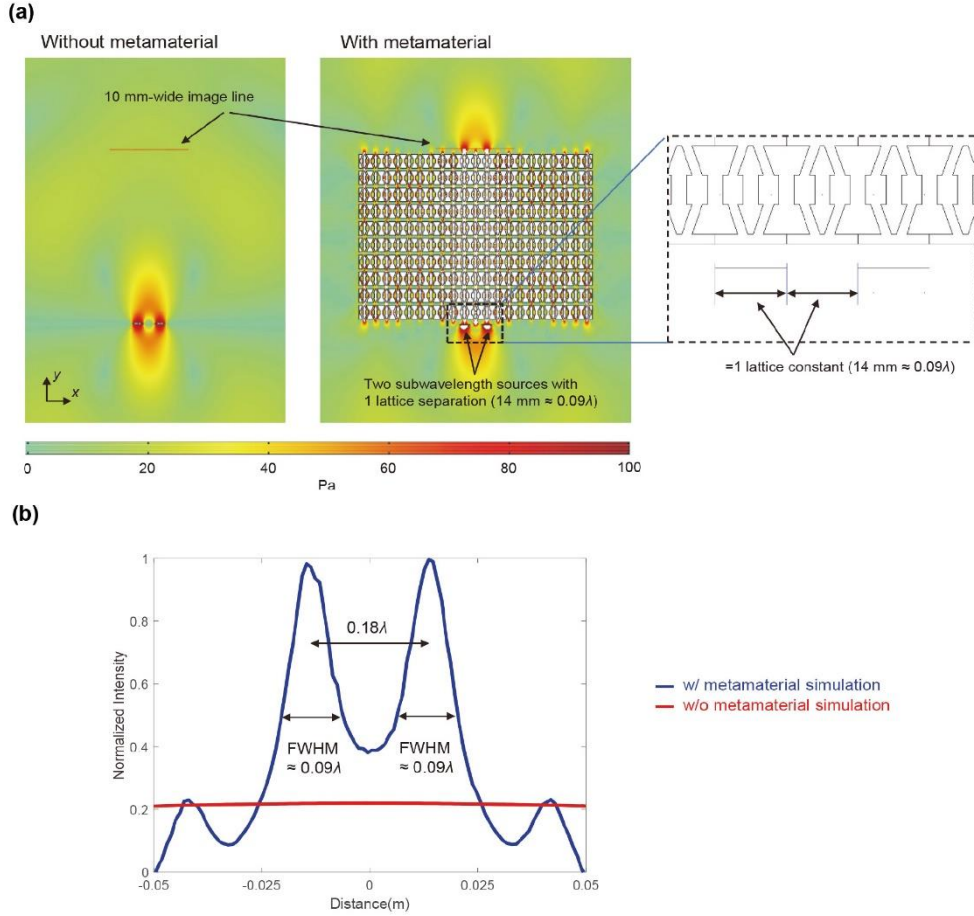


Fig. 5.9 (a) Numerical simulation for two sources as close as 1 lattice constant (14 mm or 0.09λ). The specific parameters are presented in the right side. All the simulation set-up and condition were the same as those stated in the manuscript. (b) Obtained intensity profiles conforming the subwavelength imaging capability.

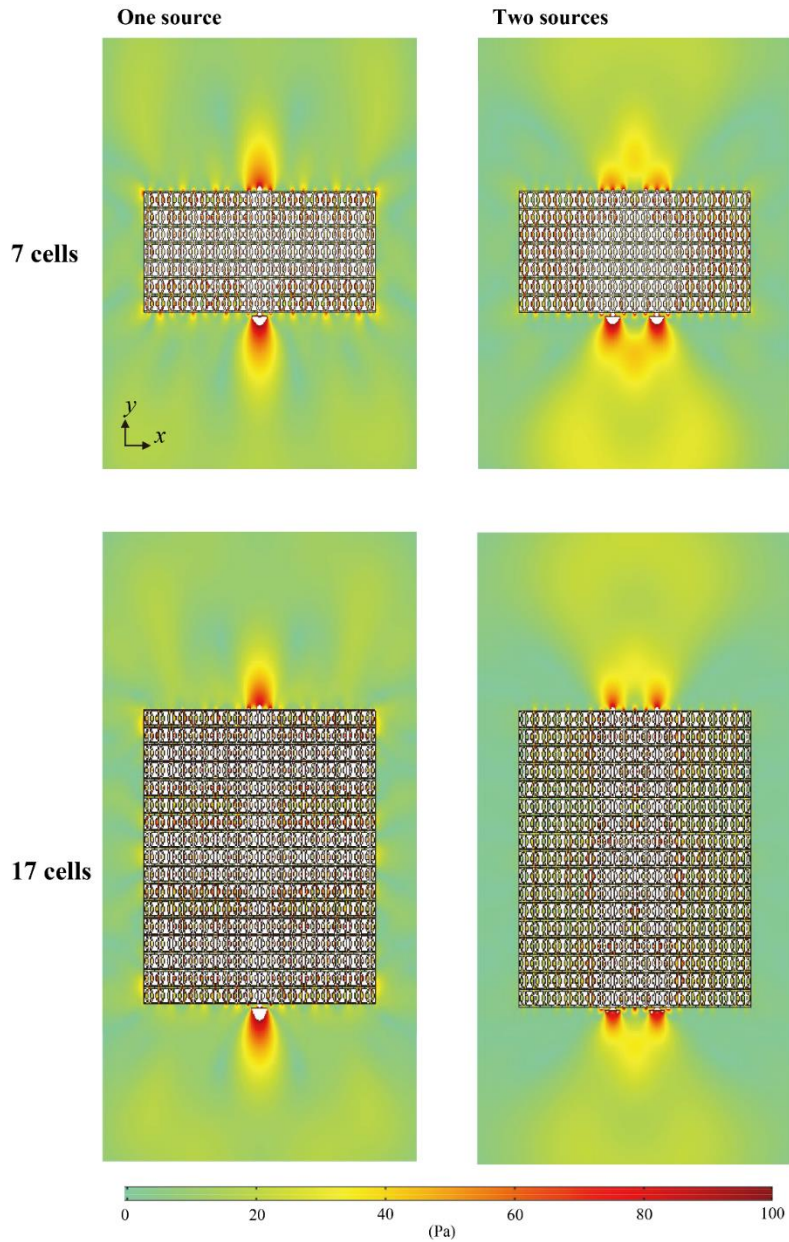


Fig. 5.10 Additional simulations for different thicknesses (not belonging to the Fabry-Perot resonance or finite resonance) of elastic metamaterial lenses. Thicknesses of 7 cells ($\approx 1\lambda$) and 17 cells ($\approx 2.43\lambda$) are considered. The resolved images are clearly observed in all figures.

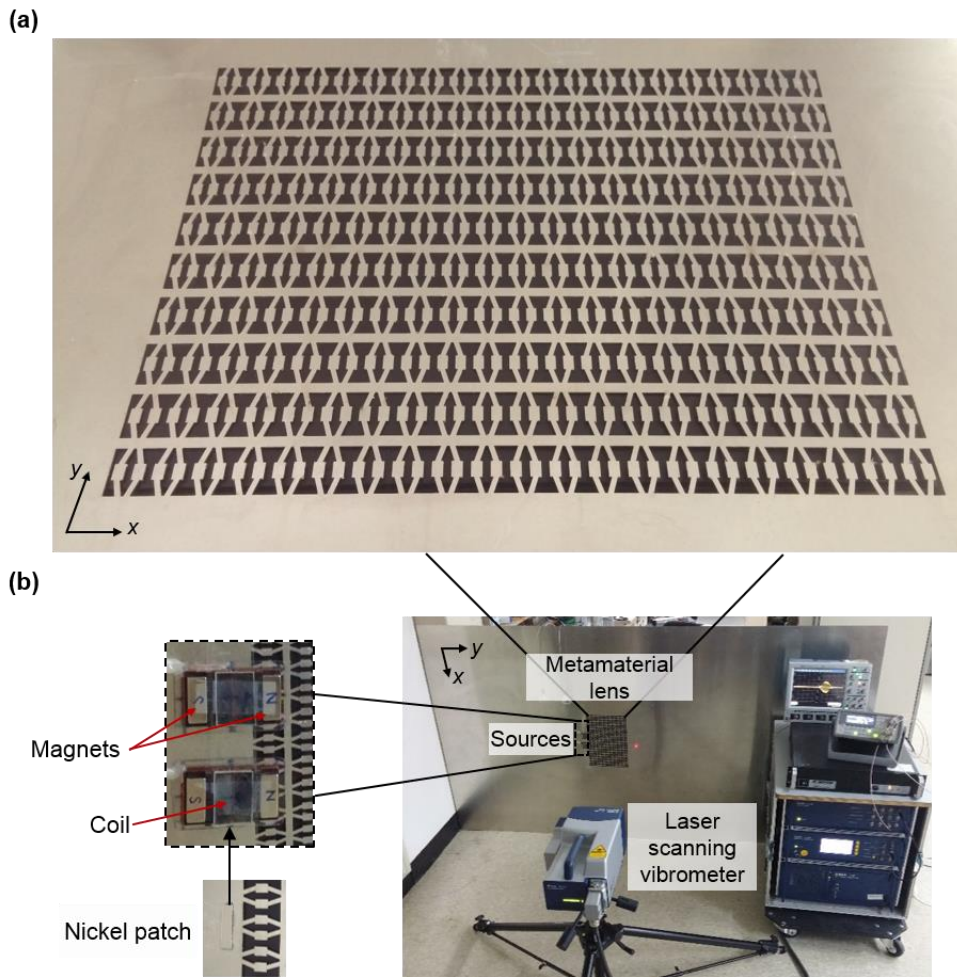


Fig. 5.11 (a) Fabricated hyperbolic elastic metamaterial lens. It consists of 21×10 unit cells. (b) Experimental set-up with magnetostrictive transducers and nickel patches that generate the S_0 wave. The middle of the figure-of-eight coil of the transducer is aligned with the nickel patch. The measurement is carried out by a laser scanning vibrometer.

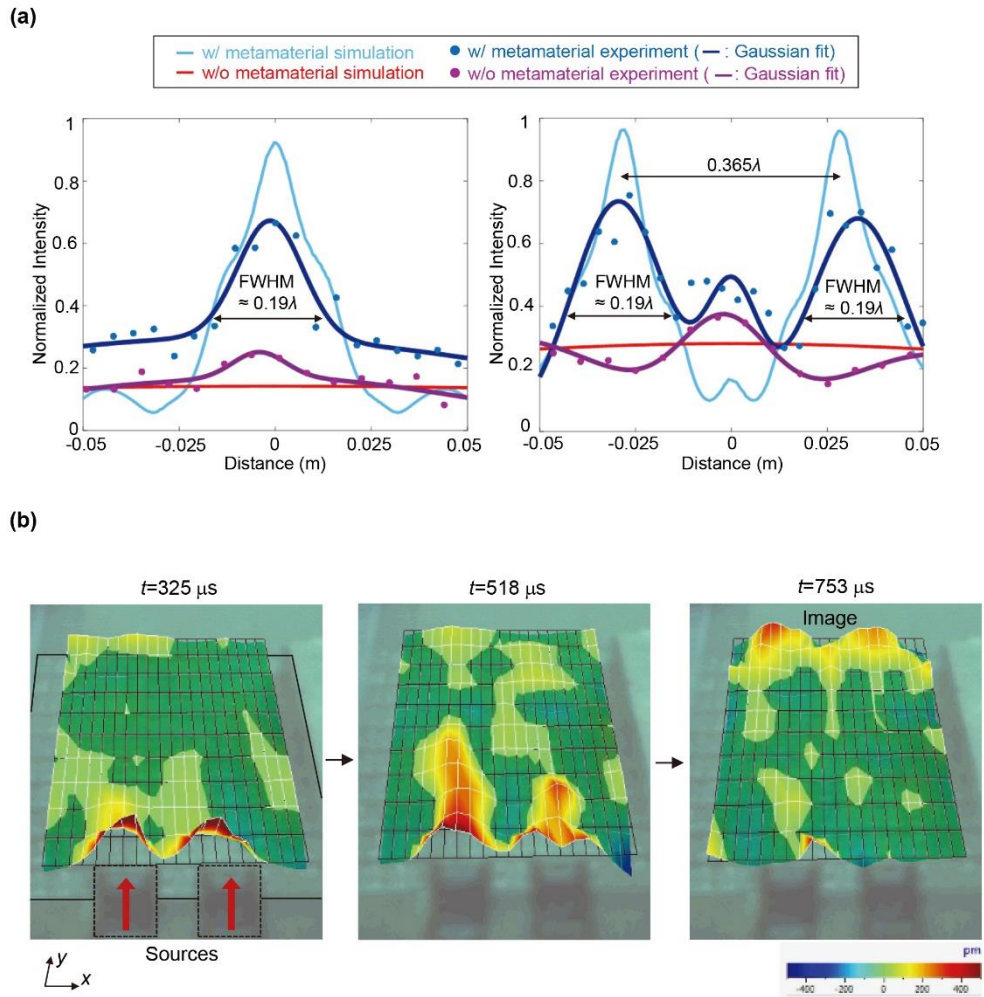


Fig. 5.12 (a) Obtained intensity profiles confirming the subwavelength resolution capability. As for the experimental data, the Gaussian regression method is applied. (b) Snapshots from animated images by laser scanning vibrometer software.

<CHAPTER 6>

CONCLUSIONS

In this dissertation, the design and applications of various elastic metamaterial substructures containing local resonators were presented. Especially, the lumped mass-spring models and their explicit transfer matrixes were developed to precisely facilitate the exact effective properties. By employing the basic underlying methods, novel elastic metamaterial structures were proposed for total transmission fine quality ultrasonic inspection applications. The detailed investigation of this work can be summarized as follows.

First of all, the proposed transfer matrix method for lumped element models can exclusively define the wave characteristics for especially resonance-based elastic metamaterials. In contrast to the conventional methods, the transfer matrix method can exceptionally evaluate the effective properties stemming from the local dynamics that are well expressed by the lumped models. There are two main contributions from the transfer matrix method. One is to estimate the principle wave characteristics including dispersion relation, characteristic impedance, and transmission coefficient by the theoretical analysis. This technique is valid not only for metamaterials but also for any materials. Also, this practice is based on the global boundary responses (displacements and forces) so that even experimental

operation can be feasible. Most of all, the analysis based on the global terms enables one to efficiently characterize the target unit cell's wave properties.

Another specialty of the transfer matrix method is to define the effective properties of the target material in harmonic basis. The dynamic responses of the unit cell expressed by its boundary displacements and forces can easily evaluate how the unit cell actually feels and reacts at every frequency. Therefore, by assuming a proper lumped model for a metamaterial unit cell or vice versa (designing a properly working continuum unit cell based on a lumped model), actual effective dynamic properties can be retrieved. Even more, all the boundary terms are well related with the transfer matrix components so that the effective properties are also well compatible with the dispersion relation, characteristic impedance, and transmission spectra.

Based on the aforementioned method, we designed two main actual continuum elastic metamaterial substructures that well realizes dipolar and monopolar resonances to bring about effective mass and stiffness, respectively. These substructures were also modeled by the basic lumped elements. The substructures are capable of tuning only mass (stiffness) parameter while keeping the stiffness (mass) term relatively constant throughout broad range of frequencies. Therefore, the substructures can be good candidates for the basic building blocks to form an elastic metamaterial with unbounded range of effective properties.

As a result, for novel applications, an elastic metasurface for full transmission beam steering functionality was proposed firstly. For the basic cell, the mass tuning substructure was implemented. To fulfill both the low phase velocity and impedance match conditions, the stiffness of the unit cell was lowered by perforated slits near the boundaries. The peculiarity of the design is that the perforated region corresponds to the spring and the dipolar continuum cell corresponds to the mass in the lumped model. Specifically, the mass substructure is responsible for amplified effective mass while the stiffness substructure is responsible for lowered stiffness. By the combination of these mass and stiffness substructures, realization of both 2π phase shift range and full transmission conditions was possible. To validate the performance of the unit cells, anomalous beam steering and focusing were investigated both by simulations and experiments. The proposed elastic metasurface is expected to minimize the conventional ultrasonic probes in unprecedented ways.

For another application, a hyperbolic elastic metamaterial lens for total transmission super-resolution imaging was designed. Here, the mass-spring model was extended to two dimensional scale to induce anisotropic effective properties. Therefore, the unit cell was designed differently from the metasurface case to satisfy such delicate conditions. The key principle lies in the shared local resonators that are connected by inclined beams. In this way, the whole unit cell

behaves as the mass tuning substructure in one direction as well as the stiffness tuning substructure in the orthogonal direction simultaneously. Thus, at the target frequency, the impedance is matched in the propagation direction by the extreme stiffness above the resonant frequency. At the same time, the hyperbolic dispersion is realized due to the negative mass occurring above the resonant frequency. The validity of the unit cell was confirmed by retrieving the effective properties by the proposed transfer matrix method. The total transmission super-resolution capability was confirmed both by numerical simulations and experiments. Such impedance matched ultrasonic lens is expected to highly enhance the quality of ultrasonic imaging techniques.

In conclusion, this dissertation is devoted to providing explicit analytic models to exactly define the behaviors of resonance-based elastic metamaterials. From the basic mechanisms, continuum novel substructures were delicately designed for multiple functionalities. By the proper combination and modification of the substructures, innovative elastic metamaterial systems were proposed for total transmission ultrasonic wave engineering applications. The overall results are expected to open doors for efficient ultrasonic controls in broad range of applications including non-destructive evaluations and medical devices. Especially, by fabricating such models into bulky metamaterials, the practicability should be maximized for actual applications.

APPENDIX A.

Derivation of the N^{th} power of the unimodular matrix

We start by solving an eigenvalue problem for the transfer matrix \mathbf{T} as

$$\begin{bmatrix} T_{11} & T_{12} \\ T_{21} & T_{22} \end{bmatrix} \mathbf{v} = \lambda \mathbf{v}, \quad (\text{A1})$$

where \mathbf{v} is the eigenvector and λ is the eigenvalue. The eigenvalues can be derived by solving the equation

$$\lambda^2 - \lambda(\text{trace}\mathbf{T}) + \det \mathbf{T} = 0. \quad (\text{A2})$$

Since the transfer matrix is unimodular (viz., $\det \mathbf{T} = 1$), eigenvalues can be given as

$$\lambda_1 = \frac{(T_{11} + T_{22}) + \sqrt{(T_{11} + T_{22})^2 - 4}}{2}, \quad (\text{A3a})$$

$$\lambda_2 = \frac{(T_{11} + T_{22}) - \sqrt{(T_{11} + T_{22})^2 - 4}}{2}. \quad (\text{A3b})$$

Here, it is worthwhile noting that the two eigenvalues are in fact reciprocal ($\lambda_1\lambda_2=1$) to each other owing to the unimodular condition. The corresponding unit eigenvectors will be defined as

$$\mathbf{v}_i = \begin{bmatrix} x_i \\ y_i \end{bmatrix}, \quad (i=1,2) \quad (\text{A4})$$

where

$$x_i = \frac{T_{12}}{\left[(T_{12})^2 + (\lambda_i - T_{11})^2 \right]^{1/2}}, \quad (\text{A5a})$$

$$y_i = \frac{\lambda_i - T_{11}}{\left[(T_{12})^2 + (\lambda_i - T_{11})^2 \right]^{1/2}}. \quad (\text{A5b})$$

We then decompose the transfer matrix in a special form as (matrix diagonalization)

$$\mathbf{T} = \mathbf{PDP}^{-1} \quad (\text{A6})$$

where \mathbf{P} is a matrix composed of eigenvectors of \mathbf{T} (\mathbf{P}^{-1} is the matrix inverse of \mathbf{P})

such that

$$\mathbf{P} = \begin{bmatrix} x_1 & x_2 \\ y_1 & y_2 \end{bmatrix}, \quad (\text{A7a})$$

$$\mathbf{P}^{-1} = \frac{1}{(x_1 y_2 - x_2 y_1)} \begin{bmatrix} y_2 & -x_2 \\ -y_2 & x_1 \end{bmatrix}, \quad (\text{A7b})$$

and \mathbf{D} is the diagonal matrix consisting of the eigenvalues so that

$$\mathbf{D} = \begin{bmatrix} \lambda_1 & 0 \\ 0 & \lambda_2 \end{bmatrix}. \quad (\text{A8})$$

In this way, the N^{th} power transfer matrix can be immediately derived as

$$\mathbf{T}^N = \mathbf{PD}^N \mathbf{P}^{-1} = \mathbf{P} \begin{bmatrix} (\lambda_1)^N & 0 \\ 0 & (\lambda_2)^N \end{bmatrix} \mathbf{P}^{-1}. \quad (\text{A9})$$

In this work, the periodic system follows the Bloch-Floquet theorem [46] so that

Eq. (A1) can be also written as

$$\begin{bmatrix} T_{11} & T_{12} \\ T_{21} & T_{22} \end{bmatrix} \mathbf{v} = e^{iqd} \mathbf{v}. \quad (\text{A10})$$

Then, Eq. (A9) can be modified to (also by using the reciprocity of the two eigenvalues)

$$\mathbf{T}^N = \mathbf{P} \mathbf{D}^N \mathbf{P}^{-1} = \mathbf{P} \begin{bmatrix} e^{iNqd} & 0 \\ 0 & e^{-iNqd} \end{bmatrix} \mathbf{P}^{-1}. \quad (\text{A11})$$

We finally solve for Eq. (A11), which yields

$$\begin{aligned} \begin{bmatrix} T_{11} & T_{12} \\ T_{21} & T_{22} \end{bmatrix}^N &= \frac{1}{(x_1 y_2 - x_2 y_1)} \begin{bmatrix} x_1 & x_2 \\ y_1 & y_2 \end{bmatrix} \begin{bmatrix} e^{iNqd} & 0 \\ 0 & e^{-iNqd} \end{bmatrix} \begin{bmatrix} y_2 & -x_2 \\ -y_2 & x_1 \end{bmatrix} \\ &= \begin{bmatrix} \frac{T_{11} \sin(Nqd) - \sin[(N-1)qd]}{\sin(qd)} & \frac{T_{12} \sin(Nqd)}{\sin(qd)} \\ \frac{T_{21} \sin(Nqd)}{\sin(qd)} & \frac{T_{22} \sin(Nqd) - \sin[(N-1)qd]}{\sin(qd)} \end{bmatrix} \end{aligned} \quad (\text{A12})$$

REFERENCES

- [1] J.B. Pendry, "Negative refraction makes a perfect lens", *Phys Rev Lett*, 85 (2000) 3966-3969.
- [2] R.A. Shelby, D.R. Smith, S. Schultz, "Experimental verification of a negative index of refraction", *Science*, 292 (2001) 77-79.
- [3] C. Luo, S.G. Johnson, J.D. Joannopoulos, J.B. Pendry, "All-angle negative refraction without negative effective index", *Physical Review B*, 65 (2002) 201104.
- [4] P.M. Valanju, R.M. Walser, A.P. Valanju, "Wave refraction in negative-index media: Always positive and very inhomogeneous", *Physical review letters*, 88 (2002) 187401.
- [5] Z.W. Liu, N. Fang, T.J. Yen, X. Zhang, "Rapid growth of evanescent wave by a silver superlens", *Applied Physics Letters*, 83 (2003) 5184-5186.
- [6] J. Pendry, "A chiral route to negative refraction", *Science*, 306 (2004) 1353-1355.
- [7] J. Shen, P. Platzman, "Near field imaging with negative dielectric constant lenses", *Applied Physics Letters*, 80 (2002) 3286-3288.
- [8] J. Pacheco Jr, T. Grzegorzczuk, B.-I. Wu, Y. Zhang, J.A. Kong, "Power propagation in homogeneous isotropic frequency-dispersive left-handed media", *Physical review letters*, 89 (2002) 257401.
- [9] D.R. Smith, D. Schurig, J.J. Mock, P. Kolinko, P. Rye, "Partial focusing of radiation by a slab of indefinite media", *Applied Physics Letters*, 84 (2004) 2244-2246.
- [10] J.B. Pendry, D. Schurig, D.R. Smith, "Controlling electromagnetic fields", *Science*, 312 (2006) 1780-1782.
- [11] A. Grbic, G.V. Eleftheriades, "Experimental verification of backward-wave radiation from a negative refractive index metamaterial", *Journal of Applied Physics*, 92 (2002) 5930-5935.
- [12] F. Martín, J. Bonache, F.a. Falcone, M. Sorolla, R. Marqués, "Split ring resonator-based left-handed coplanar waveguide", *Applied Physics Letters*, 83 (2003) 4652-4654.
- [13] J.D. Baena, L. Jelinek, R. Marques, F. Medina, "Near-perfect tunneling and amplification of evanescent electromagnetic waves in a waveguide filled by a metamaterial: Theory and experiments", *Physical Review B*, 72 (2005) 075116.
- [14] L. Zhou, W.J. Wen, C.T. Chan, P. Sheng, "Electromagnetic-wave tunneling through negative-permittivity media with high magnetic fields", *Physical review letters*, 94 (2005) 243905.
- [15] M.A. Antoniades, G.V. Eleftheriades, "Compact Linear Lead/Lag Metamaterial Phase Shifters for Broadband Applications", *IEEE Antennas and wireless propagation letters*, 2 (2003) 103-106.
- [16] I.S. Nefedov, S.A. Tretyakov, "On potential applications of metamaterials for the design of broadband phase shifters", *Microwave and Optical Technology Letters*, 45 (2005) 98-102.

- [17] A. Andryieuski, A.V. Lavrinenko, D.N. Chigrin, "Graphene hyperlens for terahertz radiation", *Physical Review B*, 86 (2012) 121108.
- [18] X.Y. Ao, C.T. Chan, "Far-field image magnification for acoustic waves using anisotropic acoustic metamaterials", *Physical Review E*, 77 (2008) 025601.
- [19] V.P. Drachev, V.A. Podolskiy, A.V. Kildishev, "Hyperbolic metamaterials: new physics behind a classical problem", *Opt Express*, 21 (2013) 15048-15064.
- [20] L. Ferrari, C.H. Wu, D. Lepage, X. Zhang, Z.W. Liu, "Hyperbolic metamaterials and their applications", *Progress in Quantum Electronics*, 40 (2015) 1-40.
- [21] Z. Jacob, L.V. Alekseyev, E. Narimanov, "Optical Hyperlens: Far-field imaging beyond the diffraction limit", *Opt Express*, 14 (2006) 8247-8256.
- [22] A.V. Kildishev, E.E. Narimanov, "Impedance-matched hyperlens", *Opt Lett*, 32 (2007) 3432-3434.
- [23] H. Chen, C.T. Chan, P. Sheng, "Transformation optics and metamaterials", *Nat Mater*, 9 (2010) 387-396.
- [24] B. Zhang, Y. Luo, X. Liu, G. Barbastathis, "Macroscopic invisibility cloak for visible light", *Phys Rev Lett*, 106 (2011) 033901.
- [25] F. Gomory, M. Solovyov, J. Souc, C. Navau, J. Prat-Camps, A. Sanchez, "Experimental Realization of a Magnetic Cloak", *Science*, 335 (2012) 1466-1468.
- [26] P.Y. Chen, J. Soric, A. Alu, "Invisibility and cloaking based on scattering cancellation", *Adv Mater*, 24 (2012) OP281-304.
- [27] V.C. Nguyen, L. Chen, K. Halterman, "Total transmission and total reflection by zero index metamaterials with defects", *Phys Rev Lett*, 105 (2010) 233908.
- [28] Y. Li, S. Kita, P. Munoz, O. Reshef, D.I. Vulis, M. Yin, M. Loncar, E. Mazur, "On-chip zero-index metamaterials", *Nature Photonics*, 9 (2015) 738-+.
- [29] M. Silveirinha, N. Engheta, "Design of matched zero-index metamaterials using nonmagnetic inclusions in epsilon-near-zero media", *Physical Review B*, 75 (2007) 075119.
- [30] R.W. Ziolkowski, "Propagation in and scattering from a matched metamaterial having a zero index of refraction", *Physical Review E*, 70 (2004) 046608.
- [31] N. Yu, F. Capasso, "Flat optics with designer metasurfaces", *Nat Mater*, 13 (2014) 139-150.
- [32] N. Yu, P. Genevet, M.A. Kats, F. Aieta, J.P. Tetienne, F. Capasso, Z. Gaburro, "Light propagation with phase discontinuities: generalized laws of reflection and refraction", *Science*, 334 (2011) 333-337.
- [33] C. Pfeiffer, A. Grbic, "Metamaterial Huygens' surfaces: tailoring wave fronts with reflectionless sheets", *Physical review letters*, 110 (2013) 197401.
- [34] F. Monticone, N.M. Estakhri, A. Alu, "Full control of nanoscale optical transmission with a composite metascreen", *Phys Rev Lett*, 110 (2013) 203903.
- [35] D. Bigoni, S. Guenneau, A.B. Movchan, M. Brun, "Elastic metamaterials with inertial locally resonant structures: Application to lensing and localization", *Physical Review B*, 87 (2013) 174303.
- [36] H. Lee, J.H. Oh, H.M. Seung, S.H. Cho, Y.Y. Kim, "Extreme stiffness

- hyperbolic elastic metamaterial for total transmission subwavelength imaging", *Sci Rep*, 6 (2016) 24026.
- [37] Y.Q. Liu, Z.X. Liang, F. Liu, O. Diba, A. Lamb, J.S. Li, "Source Illusion Devices for Flexural Lamb Waves Using Elastic Metasurfaces", *Physical review letters*, 119 (2017) 034301.
- [38] J.H. Oh, Y.E. Kwon, H.J. Lee, Y.Y. Kim, "Elastic metamaterials for independent realization of negativity in density and stiffness", *Sci Rep*, 6 (2016) 23630.
- [39] R. Zhu, X.N. Liu, G.K. Hu, C.T. Sun, G.L. Huang, "Negative refraction of elastic waves at the deep-subwavelength scale in a single-phase metamaterial", *Nature communications*, 5 (2014) 5510.
- [40] X. Yan, R. Zhu, G.L. Huang, F.G. Yuan, "Focusing guided waves using surface bonded elastic metamaterials", *Applied Physics Letters*, 103 (2013) 121901.
- [41] Y. Lai, Y. Wu, P. Sheng, Z.Q. Zhang, "Hybrid elastic solids", *Nat Mater*, 10 (2011) 620-624.
- [42] X.N. Liu, G.K. Hu, G.L. Huang, C.T. Sun, "An elastic metamaterial with simultaneously negative mass density and bulk modulus", *Applied Physics Letters*, 98 (2011) 251907.
- [43] G. Ma, C. Fu, G. Wang, P. Del Hougne, J. Christensen, Y. Lai, P. Sheng, "Polarization bandgaps and fluid-like elasticity in fully solid elastic metamaterials", *Nat Commun*, 7 (2016) 13536.
- [44] M.I. Hussein, M.J. Leamy, M. Ruzzene, "Dynamics of phononic materials and structures: Historical origins, recent progress, and future outlook", *Applied Mechanics Reviews*, 66 (2014) 040802.
- [45] P.A. Deymier, *Acoustic metamaterials and phononic crystals*, Springer Science & Business Media, 2013.
- [46] L. Brillouin, *Wave propagation in periodic structures: electric filters and crystal lattices*, Courier Corporation, 2003.
- [47] C. Croenne, E.D. Manga, B. Morvan, A. Tinel, B. Dubus, J. Vasseur, A.C. Hladky-Hennion, "Negative refraction of longitudinal waves in a two-dimensional solid-solid phononic crystal", *Physical Review B*, 83 (2011) 054301.
- [48] C. Croenne, B. Morvan, J. Vasseur, B. Dubus, A.C. Hladky-Hennion, "Analysis of Elastic Waves Transmitted Through a 2-D Phononic Crystal Exhibiting Negative Refraction", *Ieee Transactions on Ultrasonics Ferroelectrics and Frequency Control*, 58 (2011) 178-186.
- [49] A.C. Hladky-Hennion, J. Vasseur, B. Dubus, B. Djafari-Rouhani, D. Ekeom, B. Morvan, "Numerical analysis of negative refraction of transverse waves in an elastic material", *Journal of Applied Physics*, 104 (2008) 064906.
- [50] B. Morvan, A. Tinel, A.C. Hladky-Hennion, J. Vasseur, B. Dubus, "Experimental demonstration of the negative refraction of a transverse elastic wave in a two-dimensional solid phononic crystal", *Applied Physics Letters*, 96 (2010) 101905.
- [51] J. Pierre, O. Boyko, L. Belliard, J.O. Vasseur, B. Bonello, "Negative refraction

of zero order flexural Lamb waves through a two-dimensional phononic crystal", *Applied Physics Letters*, 97 (2010) 121919.

[52] J.O. Vasseur, P.A. Deymier, A. Khelif, P. Lambin, B. Djafari-Rouhani, A. Akjouj, L. Dobrzynski, N. Fettouhi, J. Zemmouri, "Phononic crystal with low filling fraction and absolute acoustic band gap in the audible frequency range: a theoretical and experimental study", *Phys Rev E Stat Nonlin Soft Matter Phys*, 65 (2002) 056608.

[53] A. Khelif, A. Choujaa, S. Benchabane, B. Djafari-Rouhani, V. Laude, "Guiding and bending of acoustic waves in highly confined phononic crystal waveguides", *Applied Physics Letters*, 84 (2004) 4400-4402.

[54] S.X. Yang, J.H. Page, Z.Y. Liu, M.L. Cowan, C.T. Chan, P. Sheng, "Ultrasound Tunneling through 3D phononic crystals", *Physical review letters*, 88 (2002) 104301.

[55] M.Z. Ke, Z.Y. Liu, Z.G. Cheng, J. Li, P. Peng, J. Shi, "Flat superlens by using negative refraction in two-dimensional phononic crystals", *Solid State Communications*, 142 (2007) 177-180.

[56] J. Li, Z.Y. Liu, C.Y. Qiu, "Negative refraction imaging of acoustic waves by a two-dimensional three-component phononic crystal", *Physical Review B*, 73 (2006) 054302.

[57] J.J. Shi, S.C.S. Lin, T.J. Huang, "Wide-band acoustic collimating by phononic crystal composites", *Applied Physics Letters*, 92 (2008) 111901.

[58] H.H. Huang, C.T. Sun, "Theoretical investigation of the behavior of an acoustic metamaterial with extreme Young's modulus", *Journal of the Mechanics and Physics of Solids*, 59 (2011) 2070-2081.

[59] H.-H. Huang, C.-T. Sun, "Anomalous wave propagation in a one-dimensional acoustic metamaterial having simultaneously negative mass density and Young's modulus", *The Journal of the Acoustical Society of America*, 132 (2012) 2887-2895.

[60] J.H. Oh, H.M. Seung, Y.Y. Kim, "Adjoining of negative stiffness and negative density bands in an elastic metamaterial", *Applied Physics Letters*, 108 (2016) 093501.

[61] J.H. Oh, H.M. Seung, Y.Y. Kim, "Doubly negative isotropic elastic metamaterial for sub-wavelength focusing: Design and realization", *Journal of Sound and Vibration*, 410 (2017) 169-186.

[62] R. Zhu, Y.Y. Chen, Y.S. Wang, G.K. Hu, G.L. Huang, "A single-phase elastic hyperbolic metamaterial with anisotropic mass density", *J Acoust Soc Am*, 139 (2016) 3303.

[63] K.T. Tan, H.H. Huang, C.T. Sun, "Blast-wave impact mitigation using negative effective mass density concept of elastic metamaterials", *International Journal of Impact Engineering*, 64 (2014) 20-29.

[64] C. Caloz, T. Itoh, *Electromagnetic metamaterials: transmission line theory and microwave applications*, John Wiley & Sons, 2005.

[65] H.H. Huang, C.T. Sun, G.L. Huang, "On the negative effective mass density in acoustic metamaterials", *International Journal of Engineering Science*, 47 (2009)

610-617.

- [66] H.J. Lee, J.R. Lee, S.H. Moon, T.J. Je, E.C. Jeon, K. Kim, Y.Y. Kim, "Off-centered Double-slit Metamaterial for Elastic Wave Polarization Anomaly", *Sci Rep*, 7 (2017) 15378.
- [67] V. Fokin, M. Ambati, C. Sun, X. Zhang, "Method for retrieving effective properties of locally resonant acoustic metamaterials", *Physical Review B*, 76 (2007) 144302.
- [68] Z. Li, K. Aydin, E. Ozbay, "Determination of the effective constitutive parameters of bianisotropic metamaterials from reflection and transmission coefficients", *Phys Rev E Stat Nonlin Soft Matter Phys*, 79 (2009) 026610.
- [69] B.H. Song, J.S. Bolton, "A transfer-matrix approach for estimating the characteristic impedance and wave numbers of limp and rigid porous materials", *J Acoust Soc Am*, 107 (2000) 1131-1152.
- [70] M. Brun, S. Guenneau, A.B. Movchan, D. Bigoni, "Dynamics of structural interfaces: Filtering and focussing effects for elastic waves", *Journal of the Mechanics and Physics of Solids*, 58 (2010) 1212-1224.
- [71] P. Yeh, A. Yariv, C.-S. Hong, "Electromagnetic propagation in periodic stratified media. I. General theory", *JOSA*, 67 (1977) 423-438.
- [72] A.V. Kildishev, A. Boltasseva, V.M. Shalaev, "Planar photonics with metasurfaces", *Science*, 339 (2013) 1232009.
- [73] X. Ni, N.K. Emani, A.V. Kildishev, A. Boltasseva, V.M. Shalaev, "Broadband light bending with plasmonic nanoantennas", *Science*, 335 (2012) 427.
- [74] A. Arbabi, Y. Horie, M. Bagheri, A. Faraon, "Dielectric metasurfaces for complete control of phase and polarization with subwavelength spatial resolution and high transmission", *Nat Nanotechnol*, 10 (2015) 937-943.
- [75] S. Colburn, A. Zhan, A. Majumdar, "Tunable metasurfaces via subwavelength phase shifters with uniform amplitude", *Sci Rep*, 7 (2017) 40174.
- [76] Y. Li, S. Qi, M.B. Assouar, "Theory of metascreen-based acoustic passive phased array", *New Journal of Physics*, 18 (2016) 043024.
- [77] J. Mei, Y. Wu, "Controllable transmission and total reflection through an impedance-matched acoustic metasurface", *New Journal of Physics*, 16 (2014) 123007.
- [78] Y. Tian, Q. Wei, Y. Cheng, Z. Xu, X.J. Liu, "Broadband manipulation of acoustic wavefronts by pentamode metasurface", *Applied Physics Letters*, 107 (2015) 221906.
- [79] Y. Xie, W. Wang, H. Chen, A. Konneker, B.I. Popa, S.A. Cummer, "Wavefront modulation and subwavelength diffractive acoustics with an acoustic metasurface", *Nat Commun*, 5 (2014) 5553.
- [80] K. Tang, C.Y. Qiu, M.Z. Ke, J.Y. Lu, Y.T. Ye, Z.Y. Liu, "Anomalous refraction of airborne sound through ultrathin metasurfaces", *Scientific Reports*, 4 (2014) 6517.
- [81] F. Aieta, P. Genevet, N. Yu, M.A. Kats, Z. Gaburro, F. Capasso, "Out-of-plane reflection and refraction of light by anisotropic optical antenna metasurfaces with

- phase discontinuities", *Nano Lett*, 12 (2012) 1702-1706.
- [82] F. Aieta, M.A. Kats, P. Genevet, F. Capasso, "Applied optics. Multiwavelength achromatic metasurfaces by dispersive phase compensation", *Science*, 347 (2015) 1342-1345.
- [83] Y. Li, B. Liang, Z.M. Gu, X.Y. Zou, J.C. Cheng, "Reflected wavefront manipulation based on ultrathin planar acoustic metasurfaces", *Sci Rep*, 3 (2013) 2546.
- [84] W.Q. Wang, Y.B. Xie, B.I. Popa, S.A. Cummer, "Subwavelength diffractive acoustics and wavefront manipulation with a reflective acoustic metasurface", *Journal of Applied Physics*, 120 (2016) 195103.
- [85] J. Zhao, B. Li, Z. Chen, C.W. Qiu, "Manipulating acoustic wavefront by inhomogeneous impedance and steerable extraordinary reflection", *Sci Rep*, 3 (2013) 2537.
- [86] Y.F. Zhu, X.Y. Zou, R.Q. Li, X. Jiang, J. Tu, B. Liang, J.C. Cheng, "Dispersionless Manipulation of Reflected Acoustic Wavefront by Subwavelength Corrugated Surface", *Sci Rep*, 5 (2015) 10966.
- [87] L. Huang, X. Chen, H. Muhlenbernd, G. Li, B. Bai, Q. Tan, G. Jin, T. Zentgraf, S. Zhang, "Dispersionless phase discontinuities for controlling light propagation", *Nano Lett*, 12 (2012) 5750-5755.
- [88] Y. Zhao, A. Alu, "Manipulating light polarization with ultrathin plasmonic metasurfaces", *Physical Review B*, 84 (2011) 205428.
- [89] X.J. Ni, A.V. Kildishev, V.M. Shalaev, "Metasurface holograms for visible light", *Nature communications*, 4 (2013) 2807.
- [90] Y. Tian, Q. Wei, Y. Cheng, X.J. Liu, "Acoustic holography based on composite metasurface with decoupled modulation of phase and amplitude", *Applied Physics Letters*, 110 (2017) 191901.
- [91] Y. Li, M.B. Assouar, "Three-dimensional collimated self-accelerating beam through acoustic metascreen", *Scientific Reports*, 5 (2015) 17612.
- [92] Y. Li, X. Jiang, B. Liang, J.C. Cheng, L.K. Zhang, "Metascreen-Based Acoustic Passive Phased Array", *Physical Review Applied*, 4 (2015) 024003.
- [93] P. Zhang, T. Li, J. Zhu, X. Zhu, S. Yang, Y. Wang, X. Yin, X. Zhang, "Generation of acoustic self-bending and bottle beams by phase engineering", *Nat Commun*, 5 (2014) 4316.
- [94] C. Faure, O. Richoux, S. Felix, V. Pagneux, "Experiments on metasurface carpet cloaking for audible acoustics", *Applied Physics Letters*, 108 (2016) 064103.
- [95] Y. Yang, H. Wang, F. Yu, Z. Xu, H. Chen, "A metasurface carpet cloak for electromagnetic, acoustic and water waves", *Sci Rep*, 6 (2016) 20219.
- [96] S.L. Zhai, H.J. Chen, C.L. Ding, L.L. Li, F.L. Shen, C.R. Luo, X.P. Zhao, "Ultrathin skin cloaks with metasurfaces for audible sound", *Journal of Physics D-Applied Physics*, 49 (2016) 225302.
- [97] M.F. Ashby, D. Cebon, "Materials Selection in Mechanical Design", *Journal De Physique Iv*, 3 (1993) 1-9.
- [98] L.J. Gibson, M.F. Ashby, *Cellular solids: structure and properties*, Cambridge

university press, 1999.

- [99] J.B. Berger, H.N.G. Wadley, R.M. Mcmeeking, "Mechanical metamaterials at the theoretical limit of isotropic elastic stiffness", *Nature*, 543 (2017) 533-+.
- [100] K. Davami, L. Zhao, E. Lu, J. Cortes, C. Lin, D.E. Lilley, P.K. Purohit, I. Bargatin, "Ultralight shape-recovering plate mechanical metamaterials", *Nat Commun*, 6 (2015) 10019.
- [101] X. Zheng, H. Lee, T.H. Weisgraber, M. Shusteff, J. DeOtte, E.B. Duoss, J.D. Kuntz, M.M. Biener, Q. Ge, J.A. Jackson, S.O. Kucheyev, N.X. Fang, C.M. Spadaccini, "Ultralight, ultrastiff mechanical metamaterials", *Science*, 344 (2014) 1373-1377.
- [102] H.J. Lee, H.W. Kim, Y.Y. Kim, "Far-field subwavelength imaging for ultrasonic elastic waves in a plate using an elastic hyperlens", *Applied Physics Letters*, 98 (2011) 241912.
- [103] J.M. Kweun, H.J. Lee, J.H. Oh, H.M. Seung, Y.Y. Kim, "Transmodal Fabry-Perot Resonance: Theory and Realization with Elastic Metamaterials", *Phys Rev Lett*, 118 (2017) 205901.
- [104] H. Zhu, F. Semperlotti, "Anomalous Refraction of Acoustic Guided Waves in Solids with Geometrically Tapered Metasurfaces", *Phys Rev Lett*, 117 (2016) 034302.
- [105] Z. Gürdal, R.T. Haftka, P. Hajela, Design and optimization of laminated composite materials, John Wiley & Sons, 1999.
- [106] Y.Y. Kim, Y.E. Kwon, "Review of magnetostrictive patch transducers and applications in ultrasonic nondestructive testing of waveguides", *Ultrasonics*, 62 (2015) 3-19.
- [107] M. Ambati, N. Fang, C. Sun, X. Zhang, "Surface resonant states and superlensing in acoustic metamaterials", *Physical Review B*, 75 (2007) 195447.
- [108] N. Fang, H. Lee, C. Sun, X. Zhang, "Sub-diffraction-limited optical imaging with a silver superlens", *Science*, 308 (2005) 534-537.
- [109] D. Maystre, S. Enoch, "Perfect lenses made with left-handed materials: Alice's mirror?", *JOSA A*, 21 (2004) 122-131.
- [110] D.R. Smith, D. Schurig, M. Rosenbluth, S. Schultz, S.A. Ramakrishna, J.B. Pendry, "Limitations on subdiffraction imaging with a negative refractive index slab", *Applied Physics Letters*, 82 (2003) 1506-1508.
- [111] D. Lu, Z. Liu, "Hyperlenses and metalenses for far-field super-resolution imaging", *Nat Commun*, 3 (2012) 1205.
- [112] A. Poddubny, I. Iorsh, P. Belov, Y. Kivshar, "Hyperbolic metamaterials", *Nature Photonics*, 7 (2013) 948.
- [113] P.A. Belov, Y. Hao, "Subwavelength imaging at optical frequencies using a transmission device formed by a periodic layered metal-dielectric structure operating in the canalization regime", *Physical Review B*, 73 (2006) 113110.
- [114] P.A. Belov, G.K. Palikaras, Y. Zhao, A. Rahman, C.R. Simovski, Y. Hao, C. Parini, "Experimental demonstration of multiwire endoscopes capable of manipulating near-fields with subwavelength resolution", *Applied Physics Letters*,

97 (2010) 191905.

[115] P.A. Belov, Y. Zhao, S. Tse, P. Ikonen, M.G. Silveirinha, C.R. Simovski, S. Tretyakov, Y. Hao, C. Parini, "Transmission of images with subwavelength resolution to distances of several wavelengths in the microwave range", *Physical Review B*, 77 (2008) 193108.

[116] B.D.F. Casse, W.T. Lu, Y.J. Huang, E. Gultepe, L. Menon, S. Sridhar, "Super-resolution imaging using a three-dimensional metamaterials nanolens", *Applied Physics Letters*, 96 (2010) 023114.

[117] B.H. Cheng, K.J. Chang, Y.C. Lan, D.P. Tsai, "Achieving planar plasmonic subwavelength resolution using alternately arranged insulator-metal and insulator-insulator-metal composite structures", *Scientific Reports*, 5 (2015) 7996.

[118] P. Ikonen, C. Simovski, S. Tretyakov, P. Belov, Y. Hao, "Magnification of subwavelength field distributions at microwave frequencies using a wire medium slab operating in the canalization regime", *Applied Physics Letters*, 91 (2007) 104102.

[119] Z. Liu, H. Lee, Y. Xiong, C. Sun, X. Zhang, "Far-field optical hyperlens magnifying sub-diffraction-limited objects", *Science*, 315 (2007) 1686.

[120] J. Rho, Z.L. Ye, Y. Xiong, X.B. Yin, Z.W. Liu, H. Choi, G. Bartal, X.A. Zhang, "Spherical hyperlens for two-dimensional sub-diffractive imaging at visible frequencies", *Nature communications*, 1 (2010) 143.

[121] A. Tuniz, K.J. Kaltenecker, B.M. Fischer, M. Walther, S.C. Fleming, A. Argyros, B.T. Kuhlmey, "Metamaterial fibres for subdiffraction imaging and focusing at terahertz frequencies over optically long distances", *Nature communications*, 4 (2013) 2706.

[122] J. Li, L. Fok, X. Yin, G. Bartal, X. Zhang, "Experimental demonstration of an acoustic magnifying hyperlens", *Nat Mater*, 8 (2009) 931-934.

[123] J.H. Oh, H.M. Seung, Y.Y. Kim, "A truly hyperbolic elastic metamaterial lens", *Applied Physics Letters*, 104 (2014) 073503.

[124] J. Kerbst, S. Schwaiger, A. Rottler, A. Koitmae, M. Broll, J. Ehlermann, A. Stemmann, C. Heyn, D. Heitmann, S. Mendach, "Enhanced transmission in rolled-up hyperlenses utilizing Fabry-Perot resonances", *Applied Physics Letters*, 99 (2011) 191905.

[125] G. Li, H. Tam, F. Wang, K. Cheah, Half-cylindrical far field superlens with coupled Fabry-Perot cavities, in, AIP, 2008.

[126] A. Liu, X. Zhou, G. Huang, G. Hu, "Super-resolution imaging by resonant tunneling in anisotropic acoustic metamaterials", *J Acoust Soc Am*, 132 (2012) 2800-2806.

[127] X.C. Xu, P. Li, X.M. Zhou, G.K. Hu, "Experimental study on acoustic subwavelength imaging based on zero-mass metamaterials", *Epl*, 109 (2015) 28001.

[128] X.M. Zhou, G.K. Hu, "Superlensing effect of an anisotropic metamaterial slab with near-zero dynamic mass", *Applied Physics Letters*, 98 (2011) 263510.

[129] H. Su, X. Zhou, X. Xu, G. Hu, "Experimental study on acoustic subwavelength imaging of holey-structured metamaterials by resonant tunneling",

- J Acoust Soc Am*, 135 (2014) 1686-1691.
- [130] J. Zhu, J. Christensen, J. Jung, L. Martin-Moreno, X. Yin, L. Fok, X. Zhang, F.J. Garcia-Vidal, "A holey-structured metamaterial for acoustic deep-subwavelength imaging", *Nature physics*, 7 (2011) 52-55.
- [131] S.S. Yao, X.M. Zhou, G.K. Hu, "Investigation of the negative-mass behaviors occurring below a cut-off frequency", *New Journal of Physics*, 12 (2010) 103025.
- [132] Y. Wu, Y. Lai, Z.Q. Zhang, "Elastic metamaterials with simultaneously negative effective shear modulus and mass density", *Phys Rev Lett*, 107 (2011) 105506.
- [133] X.M. Zhou, G.K. Hu, "Analytic model of elastic metamaterials with local resonances", *Physical Review B*, 79 (2009) 195109.
- [134] S.H. Cho, J.S. Lee, Y.Y. Kim, "Guided wave transduction experiment using a circular magnetostrictive patch and a figure-of-eight coil in nonferromagnetic plates", *Applied Physics Letters*, 88 (2006) 224101.
- [135] J.S. Lee, S.H. Cho, Y.Y. Kim, "Radiation pattern of Lamb waves generated by a circular magnetostrictive patch transducer", *Applied Physics Letters*, 90 (2007) 054102.
- [136] J.S. Lee, Y.Y. Kim, S.H. Cho, "Beam-focused shear-horizontal wave generation in a plate by a circular magnetostrictive patch transducer employing a planar solenoid array", *Smart Materials and Structures*, 18 (2008) 015009.
- [137] J. Jung, F.J. Garcia-Vidal, L. Martin-Moreno, J.B. Pendry, "Holey metal films make perfect endoscopes", *Physical Review B*, 79 (2009) 153407.
- [138] S.Y. Lee, Y.H. Lai, K.C. Huang, Y.H. Cheng, T.F. Tseng, C.K. Sun, "In vivo sub-femtoliter resolution photoacoustic microscopy with higher frame rates", *Sci Rep*, 5 (2015) 15421.

ABSTRACT (KOREAN)

질량-강성 분절설계 탄성 메타물질을 활용한 완벽투과율 초음파 제어

이 혁

서울대학교 대학원

기계항공공학부

본 연구에서는 완벽투과율과 동시에 여러 파동 특이 현상을 제공하는 질량-강성 분절구조 탄성 메타 물질에 대한 새로운 설계 방법론을 구현 및 정립하는 것을 목표로 한다. 최근, 비파괴 검사 및 의료계 이미징 등의 광범위한 응용 분야에서 초음파를 혁신적으로 제어 할 수 있는 인공구조물인 탄성 메타물질들이 크게 대두되었다. 그러나, 기존의 시스템들은 인위적으로 제조 된 (천공 된 혹은 합성 된) 메타물질과 그 바탕의 매질 사이에 필연적으로 존재하는 임피던스 불일치 때문에 여전히 매우 낮은 투과성의 한계를 겪고 있으며, 이는 결과적으로 검사 품질을 심각하게 저해한다.

이러한 고질적인 딜레마를 해결하기 위해 본 연구에서는 탄성 메타 물질

단위 구조의 질량 및 강성 특성을 독립적으로 제어하여 자체의 임피던스가 외부 탄성 매체에 대해 편리하게 조정될 수 있는 방법론을 제안하였다. 구체적으로는, 독창적으로 설계된 국부 공진기를 포함하는 기본 분절 구조가 오로지 질량 또는 강성만을 각각 조절하도록 설계 하는 것이다. 이러한 분절 구조들을 적절히 배합함으로써, 임피던스 매칭 조건 (완벽 투과) 과 동시에 특이 등가물성치 (음의 유효 질량/강성 뿐만 아니라 극대화된 물성치도 포함) 를 활용한 파동 특이 현상을 구현할 수 있다. 더 나아가 이렇게 개발 된 하부 구조 방법을 이용하여 두 가지 새로운 탄성 메타 물질 구조를 제안하였다. 먼저, 세파장 스케일 내에서 혁신적인 빔 패턴 조종을 위한 탄성 메타 서피스를 설계하기 위해 임피던스 매칭 조건과 동시에 낮은 위상 속도를 달성하였다; 증폭된 질량 및 감소된 강성 구현. 또한, 초고해상도 완벽투과율 하이퍼볼릭 렌즈의 경우, 쌍곡선 분산특성 및 임피던스 매칭 조건을 달성하기 위하여 극한 강성과 음의 유효 질량을 동시에 적용하였다. 이러한 독창적인 분절구조 메커니즘과 그에 대한 응용은 우수한 품질의 완벽투과율 초음파 검사를 구현하는 탄성 메타 물질의 설계에 대한 유연성을 크게 향상시킬 것으로 기대된다.

주요어: 탄성 메타물질, 분절 구조, 유도 초음파, 주기 구조, 등가 물성치.

학 번 : 2012-22564

ACKNOWLEDGEMENTS

This research was supported by the National Research Foundation of Korea (NRF) Grant [No. 2014M3A6B3063711 and 2016R1A2B3010231] funded by the Korean Ministry of Science, ICT and Future Planning (MSIP) contracted through IAMD at Seoul National University.